

UNDERSTANDING RADIO OUTFLOWS IN SEYFERT GALAXIES

A Thesis

Submitted to the

Tata Institute of Fundamental Research
(A Deemed University)

for the degree of Doctor of Philosophy
in Physics

by

Biny Sebastian



National Centre for Radio Astrophysics
Tata Institute of Fundamental Research
September 2020

Abstract

The origin of the kiloparsec scale radio structures (KSR) in the radio-quiet subclass of active galactic nuclei (AGN), viz., Seyfert galaxies, is still not well understood. Several mechanisms including starburst winds, AGN driven winds and AGN jets have been proposed in the literature. To distinguish between the contribution from various mechanisms, we have carried out VLA observations at 5.5 GHz and 1.5 GHz in full-polarization mode in the B-array configurations (some observations carried out using hybrid configurations, BnA and BnA→A) of a sample of Seyfert galaxies with KSRs, along with a comparison sample of starburst galaxies. The radio morphologies of the Seyfert galaxies show lobe/bubble-like features or prominent cores in radio emission whereas the starburst galaxies show radio emission spatially coincident with the star-forming regions seen in optical images. There is tentative evidence that Seyferts tend to show more polarized structures (with higher degrees of polarization) than starburst galaxies at the resolution of our observations. In the Seyferts that show polarized emission, the inferred magnetic fields are typically aligned with the lobe edges but appear to be longitudinal inside the lobes w.r.t. the outflow directions. Several sources however, reveal the presence of rotation measure (RM) gradients; RM gradients have been suggested to be the signatures of helical magnetic fields. A multi-epoch, multi-frequency study of the starburst-Seyfert composite galaxy NGC 3079, reveals that the jet together with the starburst superwind and the galactic magnetic fields are likely to be responsible for the well-known highly-polarized 8-shaped radio lobes observed in this galaxy. We find that unlike Seyfert galaxies with KSRs, starburst galaxies with

superwinds do not show a “radio excess” compared to the radio-FIR correlation. This suggests that shock acceleration is not adequate to explain the excess radio emission seen in Seyferts and hence it most likely has a jet-related origin. We also find that the [O III] luminosity of the Seyferts is correlated with the off-nuclear radio emission from the lobes, whereas it is not well correlated with the total emission which also includes the radio core. This suggests strong jet-medium interaction, which in turn limits the jet/lobe extents in Seyferts. This is consistent with the “frustrated jet scenario” often invoked in the literature to explain the small sizes of Seyfert outflows. We find that the power contribution of AGN jet, AGN accretion, and star formation is more or less comparable in our sample of Seyfert galaxies. The Seyfert galaxy NGC 2639, shows highly polarized secondary radio lobes, not observed before, which are aligned perpendicular to the known pair of radio lobes. The additional pair of lobes represent an older epoch of emission. We find indications of episodic AGN activity in the majority of our Seyfert galaxies.

List of Refereed Publications Related to Thesis

1. **Sebastian, B.**, Kharb, P., O' Dea, C.P., Gallimore, J. F., & Baum, S. A., *A Radio Polarimetric Study to Disentangle AGN Activity and Star-Formation in Seyfert Galaxies* (accepted for publication in MNRAS), 2020, arXiv e-prints, p. arXiv:2008.06039
2. **Sebastian, B.**, Kharb, P., O' Dea, C.P., Gallimore, J. F., Colbert, E. J. M., & Baum, S. A., *Understanding the Origin of Radio Outflows in Seyfert Galaxies using Radio Polarimetry* (accepted for publication in IAU proceedings), 2019, arXiv e-prints, p. arXiv:1912.09511
3. **Sebastian, B.**, Kharb, P., O' Dea, C.P., Gallimore, J. F., & Baum, S. A., *The Discovery of Secondary Lobes in the Seyfert Galaxy NGC 2639*, 2019, Monthly Notices of the Royal Astronomical Society Letters, 490, L26
4. **Sebastian, B.**, Kharb, P., O'Dea, C. P., Colbert, E. J. M., & Baum, S. A., *The filamentary radio lobes of the Seyfert-Starburst composite galaxy NGC3079*, 2019, The Astrophysical Journal, 883, 189

Other Refereed Publications

5. **Sebastian, B.**, & Bait, O., *Radio continuum emission from local analogs of high- z faint LAEs: Blueberry galaxies*, 2019, The Astrophysical Journal Letters, 882(2):L19
6. **Sebastian, B.**, Ishwara-Chandra, C. H., Joshi, R., & Wadadekar, Y., *Discovery of a new, 2.2-Mpc giant radio galaxy at a redshift of 0.56*, 2018, Monthly Notices of the Royal Astronomical Society, 473:4926–4931
7. **Sebastian, B.**, Lal, D. V., & Rao, A. P., *Giant metrewave radio telescope observations of head-tail radio galaxies*, 2017, Astronomical Journal, 154, 169
8. Gendron-Marsolais, M., Hlavacek-Larrondo, J., van Weeren, R. J., Rudnick, L., Clarke, T. E., **Sebastian, B.** et al., *High-resolution VLA low radio*

frequency observations of the Perseus cluster: radio lobes, mini-halo, and bent-jet radio galaxies., 2020, Monthly Notices of the Royal Astronomical Society, 499(4):5791–5805

9. Lal, D. V., **Sebastian, B.**, Cheung, C. C., & Pramesh Rao, A., *GMRT Low-frequency Imaging of an Extended Sample of X-shaped Radio Galaxies*, 2019, Astronomical Journal, 157(5):195
10. Veena, V. S., Vig, S., **Sebastian, B.**, Lal, D. V., Tej, A., & Ghosh, S. K., *Non-thermal emission from massive star-forming regions: a possible SNR candidate G351.7-1.2?* 2019, Monthly Notices of the Royal Astronomical Society, 482, 4630V
11. Kharb, P., Vaddi, S., **Sebastian, B.**, Subramanian, S., Das, M.,& Paragi, Z. *A Curved 150 pc Long Jet in the Double-peaked Emission-line AGN KISSR 434*, 2019, Astrophysical Journal, 871(2):249

Contents

List of Figures	xv
List of Tables	xxiii
List of Symbols & Abbreviations	xxv
1 Introduction	1
1.1 AGN	2
1.1.1 Historical overview	2
1.1.2 Types of AGN	3
1.1.2.1 Seyfert galaxies	3
1.1.2.2 Quasars	4
1.1.2.3 Radio galaxies	5
1.1.2.4 LINERs	6
1.1.2.5 Blazars	6
1.1.3 Unification Scheme	8
1.1.3.1 Supermassive Black Hole	9
1.1.3.2 Accretion Disk	9
1.1.3.3 Dusty Obscuring Torus	10
1.1.3.4 Broad Line Region	11
1.1.3.5 Narrow Line Region	11
1.1.3.6 Jet	12
1.2 Formation of Relativistic Jets in AGN	13
1.2.1 Accretion Rate and Black Hole Mass	14
1.2.2 Black Hole Spin	14

CONTENTS

1.2.3	Accretion State	15
1.2.4	Magnetic Flux	15
1.3	Radio Emission from Seyfert Galaxies	15
1.4	Possible mechanisms for the origin of radio emission	17
1.4.1	Starburst driven winds	17
1.4.2	AGN accretion driven winds	18
1.4.2.1	Radiation pressure driven winds	19
1.4.2.2	Thermally driven winds	20
1.4.2.3	Magnetically driven winds	20
1.4.3	AGN Jets	21
1.4.4	Coronal emission	21
1.5	Diffusive shock acceleration and magnetic fields	22
1.6	Polarization properties of radio outflows	23
1.6.1	Galactic Dynamo	23
1.6.2	Magnetic fields in jets	24
1.7	Jet-NLR interaction	24
1.8	AGN Jet Duty Cycle in Seyfert Galaxies	25
1.9	Objectives of this thesis	26
1.10	Outline of the thesis	27
2	Radio Interferometry and Polarimetry Techniques	29
2.1	Radio Interferometry	29
2.1.1	Basic calibration	30
2.1.2	Deconvolution	31
2.2	Radio Polarimetry	32
2.2.1	Formulation of the radio interferometric polarimetry	33
2.2.2	Polarization Calibration	34
2.2.2.1	Leakage Calibration	36
2.2.2.2	Polarization angle calibration	36
2.3	Depolarization	37
2.4	Rotation Measure Synthesis	39
39section.2.5		

CONTENTS

3 The Filamentary Radio Lobes of the Seyfert-Starburst Composite Galaxy NGC 3079	41
3.1 Introduction	41
3.2 Observations and Data Analysis	43
3.2.1 VLA Data from 1995	43
3.2.2 VLA Data from 2018	44
3.3 Radio Morphology: Lobes, Ring, Galaxy	46
3.3.1 Host Galaxy Emission	50
3.3.2 Spectral and Polarization properties	50
3.4 Energetics of Radio lobes	53
3.5 The origin of the ring and filamentary morphology	60
3.5.1 Shock compression at the boundaries of an expanding superbubble	62
3.5.2 Magnetic Draping	64
3.5.3 Filaments as magnetic flux tubes	65
3.6 Role of the jet in inflating the radio bubble	67
3.7 Summary and Conclusions	69
4 The Seyfert and the Starburst galaxy sample	71
4.1 Introduction	71
4.2 The Sample	74
4.3 Observations and Data analysis	77
4.4 Results	83
4.4.1 Radio Morphology	83
4.4.1.1 NGC 2639	84
4.4.1.2 NGC 2992	84
4.4.1.3 NGC 3079	84
4.4.1.4 NGC 3516	85
4.4.1.5 NGC 4051	85
4.4.1.6 NGC 4235	85
4.4.1.7 NGC 4593	86
4.4.1.8 NGC 4388	86
4.4.1.9 NGC 5506	87

CONTENTS

4.4.1.10 NGC 1134	87
4.4.1.11 NGC 253	87
4.4.1.12 NGC 3044	88
4.4.1.13 NGC 3628	88
4.4.1.14 NGC 4631	88
4.4.1.15 NGC 7541	89
4.4.1.16 UGC 903	89
4.4.2 Polarization Properties	89
4.5 Discussion	98
4.5.1 Correlation between star-formation and radio emission . .	103
4.5.2 Investigating the correlation of radio emission with NLR properties	106
4.5.3 Relative energy input from various mechanisms	109
4.5.3.1 Jet power	109
4.5.3.2 Kinetic energy from AGN bolometric radiation .	113
4.5.3.3 Energy injection rate due to star formation	113
4.6 Conclusions and Summary	115
5 Episodic Activity in Seyfert Galaxies	117
5.1 Introduction	117
5.2 Observations and Data Analysis	118
5.3 Results	120
5.4 Discussion	122
5.4.1 Episodic Jet Activity in the sample	129
5.5 Summary	131
6 Conclusions and Future Work	133
6.1 Summary of the thesis	133
Bibliography	137

List of Figures

1.1	Baldwin, Phillips and Terlevich (BPT) diagram to distinguish between various types of sources. The triangles, open circles and filled circles represent, LINERs, HII regions and Seyfert galaxies respectively. Figure taken from Peterson (1997). Credits: R.W. Pogge using data from Veilleux & Osterbrock (1987)	7
1.2	Schematic illustrating the anatomy of the standard unified model of AGN (Urry & Padovani, 1995).	8
2.1	Polarization State of linear, circular and elliptical polarization . .	32
2.2	Illustration of various effects encountered along the path of the astrophysical signal. Taken from Hamaker et al. (1996)	35
3.1	Grey scale images of total intensity showing the filamentary radio structures observed in NGC 3079 with the (left) historical VLA A-array at 1.4 GHz with a beam size $1.45'' \times 1.19''$ and P.A., -80.2° and (right) historical VLA B-array at 5 GHz with a beam size, $0.58'' \times 0.43''$ and P.A., 85.8°	45
3.2	(Left) 1.4 GHz historical VLA A-array image with contour levels $0.850 \times (-0.170, 0.170, 0.350, 0.700, 1.400, 2.800, 5.600, 11.25, 22.50, 45, 90)$ mJy beam $^{-1}$ and (right) 5 GHz historical VLA B-array image with contour levels $0.800 \times (-0.085, 0.085, 0.170, 0.350, 0.700, 1.400, 2.800, 5.600, 11.25, 22.50, 45, 90)$ mJy beam $^{-1}$ of NGC 3079 with electric vectors whose length is proportional to the fractional polarization superimposed in red.	47

LIST OF FIGURES

3.3	New VLA 5 GHz image of NGC 3079 with total intensity in contours and polarized intensity in colour. The polarization electric vectors are shown in magenta. Contour levels represent $25.5 \times (2, 4, 6, 8, 16, 64, 256, 512, 1024) \mu\text{Jy beam}^{-1}$. The beam shown in the bottom left corner as a filled ellipse is of size $1.10'' \times 0.47''$ and P.A. is -87° .	49
3.4	(Left) 1.4 GHz historical VLA C-array image of NGC 3079 with contour levels = $3.0 \times (-0.085, 0.085, 0.170, 0.350, 0.700, 1.400, 2.800, 5.600, 11.25, 22.50, 45, 90) \text{mJy beam}^{-1}$ and (right) 5 GHz historical VLA A-array image with contour levels = $0.61 \times (-0.085, 0.085, 0.170, 0.350, 0.700, 1.400, 2.800, 5.600, 11.25, 22.50, 45, 90) \text{mJy beam}^{-1}$. The electric vectors with length proportional to fractional polarization are superimposed in red.	51
3.5	The 1.4 - 5 GHz historical VLA spectral index image of NGC 3079 in color superimposed by the 1.4 GHz radio contours. The circular beam shown in the left corner is of size $1.45'' \times 1.45''$.	52
3.6	(Top) The three frequency historical VLA rotation measure image in color superimposed by the 1.4 GHz radio contours and (bottom) the color in-band VLA rotation measure image of the north-eastern lobe. The circular beam shown in the left corner of the left panel is of size $1.45'' \times 1.45''$.	54
3.7	The historical VLA depolarization image of NGC 3079 in color made using the 1.4 and 5 GHz image, superimposed by the 1.4 GHz radio contours. The circular beam shown in the left corner is of size $1.45'' \times 1.45''$.	55
3.8	(Top) The spectral index image and (bottom) equipartition magnetic field image in colour, of the north-eastern lobe made using the 1.4 GHz and 5 GHz historical VLA images. The pink contours denote the VLA polarized intensity at 5 GHz. The left bottom corner shows the 1.4 and 5 GHz historical VLA circular beams enclosing the elliptical VLA beam at 5 GHz.	57

LIST OF FIGURES

3.9 (Left) Overlay of the contours representing the <i>HST</i> WFPC2 $H\alpha + [NII]$ line emission in blue and (right) Chandra ACIS-S X-ray emission in pink, over the total intensity image in colour of NGC 3079 with the historical VLA A-array at 1.4 GHz.	60
4.1 Total intensity images of Seyfert galaxies at 5.5 GHz. The contour levels used are $3\sigma \times (-2, -1, 1, 2, 4, 8, 16, 32, \dots)$, where $\sigma = 8.83, 10.59, 25.57, 13.085 \mu\text{Jy beam}^{-1}$ for NGC 2639 (top left), NGC 2992 (top right), NGC 3079 (bottom left), NGC 3516 (bottom right) respectively.	78
4.1 Continued –Total intensity images of Seyfert galaxies at 5.5 GHz. The contour levels used are $3\sigma \times (-2, -1, 1, 2, 4, 8, 16, 32 \dots)$, where $\sigma = 14.36, 21.35, 33.42, 134.43 \mu\text{Jy beam}^{-1}$ for NGC 4051 (top left), NGC 4235 (top right), NGC 4593 (bottom left), NGC 5506 (bottom right) respectively.	79
4.1 Continued –Total intensity images of Seyfert galaxies at 5.5 GHz. The contour levels used are $3\sigma \times (-2, -1, 1, 2, 4, 8, 16, 32 \dots)$, where $\sigma = 45.08 \mu\text{Jy beam}^{-1}$ for NGC 4388.	80
4.2 Total intensity images of starburst galaxies. The contour levels used are $3\sigma \times (-2, -1, 1, 2, 4, 8, 16, 32, \dots)$, where $\sigma = 24.61, 205.06, 30.076, 9.60 \mu\text{Jy beam}^{-1}$ for NGC 1134 at 1.5 GHz (top left), NGC 253 at 1.5 GHz (top right), NGC 3044 at 5.5 GHz (bottom left), NGC 3628 at 5.5 GHz (bottom right) respectively.	81
4.2 Continued –Total intensity images of starburst galaxies. The contour levels used are $3\sigma \times (-2, -1, 1, 2, 4, 8, 16, 32, \dots)$, where $\sigma = 9.66, 39.68, 22.2 \mu\text{Jy beam}^{-1}$ for NGC 4631 at 5.5 GHz (top), NGC 7541 at 1.5 GHz (bottom left), UGC 903 at 1.5 GHz (bottom right) respectively.	82

LIST OF FIGURES

4.3	Zoomed-in polarization image of NGC 253: Polarization electric vectors in red overlaid on color image of the polarized intensity and total intensity contours for NGC 253 with contour levels = $0.48 \times (1, 2, 4, 8, 16, 32, 64, 128, 256, 512)$ mJy beam $^{-1}$. The polarization intensity and polarization angle images were produced using RM synthesis.	91
4.4	Polarization electric vectors with length proportional to fractional polarization in red overlaid on total intensity contours for (top) NGC 4388 at 5.5 GHz with contour levels = $0.13 \times (-2, -1, 1, 2, 4, 8, 16, 32, 64, 128, 256, 512)$ mJy beam $^{-1}$, with one arcsec length of the polarization vector corresponding to 6.8% fractional polarization and (bottom) NGC 5506 at 5.5 GHz with contour levels = $1.17 \times (-0.350, 0.350, 0.700, 1.400, 2.800, 5.600, 11.30, 22.50, 45, 90)$ mJy beam $^{-1}$ with one arcsec length of the polarization vector corresponding to 6.7% fractional polarization.	92
4.5	The 5 GHz total intensity radio contours superimposed over the in-band rotation measure image of NGC 4388 in color. Contour levels: $213 \times (-2, -1, 1, 2, 4, 8, 16, 32, 64, 128, 256, 512)$ μ Jy beam $^{-1}$. The beam shown in the lower left corner is of size $1.3'' \times 1.30''$. The RM values are in units 1000 rad m $^{-2}$	93
4.6	The in-band spectral index image of NGC 4388 in color with 5 GHz radio contours superimposed. Contour levels: $5 \times 10^{-4} \times (1, 2, 4, 8, 16, 32, 64, 128, 256, 512)$ Jy beam $^{-1}$. The circular beam shown in the lower left corner is of size $\sim 5''$	94
4.7	Radio total intensity emission overlaid in white contours over the optical color composite images. The optical images are taken from various optical surveys namely, DECaLS, MzLS, SDSS and DSS depending on the availability of data in these surveys. We have used only the DSS r-band image to make the overlays of NGC 253, NGC 1134 and NGC 2992 due to the poor quality of the color composite image.	99

LIST OF FIGURES

4.7	Continued–Radio total intensity emission overlaid in white contours over the optical color composite images.	100
4.7	Continued–Radio total intensity emission overlaid in white contours over the optical color composite images.	101
4.8	Plot of FIR luminosity at $60 \mu\text{m}$ vs the 1.4 GHz luminosity in W Hz^{-1} . The black line shows the radio-FIR correlation whereas the region shaded using dark grey and light grey represents the 1σ and 3σ boundary limits of the radio-FIR correlation from Yun et al. (2001).	104
4.9	Top: [O III] line luminosity versus the integrated radio luminosity at 5.5 GHz. Bottom: [O III] line luminosity versus the radio lobe luminosity at 5.5 GHz.	110
4.10	Overlay of radio continuum intensity contours in cyan on [O III] emission line images of NGC 4388 (Left) NGC 3516 (Right) . . .	111
4.11	Top left: jet power versus AGN energy input rate from bolometric luminosities for the Seyfert sample. The identity line is indicated. Top right: The Seyfert sample in the fundamental plane of BH activity, along with its well-known scatter from observations in the literature in grey. Bottom left: AGN energy input rate from bolometric luminosities versus energy input from SFR. Bottom right: Energy injected from SFR versus the difference in AGN and jet power.	112
5.1	The color SDSS image of NGC 2639 superimposed by 5 GHz VLA radio contours in red, clearly showing the presence of the newly discovered north-south radio lobes.	119

LIST OF FIGURES

- 5.2 (Top left) 5.5 GHz total intensity radio contours of NGC 2639 with polarized intensity shown in color. Red ticks denote the polarization electric vectors with lengths proportional to the fractional polarization. Contour levels: $50 \times (-2, -1, 1, 2, 4, 8, 16, 32, 64, 128, 256, 512) \mu\text{Jy beam}^{-1}$. The newly discovered north-south lobes are highly linearly polarised. The beam shown in the bottom left corner is of size $1.15'' \times 1.00''$ at PA = -4.9° . (Top right) 5 GHz total intensity radio contours overlaid on colour image of the total intensity of NGC 2639. Contour levels: $164 \times (-2, -1, 1, 2, 4, 8, 16, 32, 64, 128) \mu\text{Jy beam}^{-1}$. The east-west lobes are embedded within the core of the image in the left panel. The beam shown in the bottom left corner is of size $0.435'' \times 0.302''$ at PA = 85.4° . (Bottom) 8.3 GHz archival VLBA image showing a ~ 1 parsec jet at PA = 130° . Contour levels: $239.2 \times (-2, -1, 1, 2, 4, 8, 16, 32, 64) \mu\text{Jy beam}^{-1}$. The beam shown in the bottom left corner is of size $7.7 \text{ mas} \times 6.2 \text{ mas}$ at PA = -5° 123
- 5.3 Plot of the infrared SED fit and its residual for NGC 2639. Data are in black, with upper limits (inverted triangles) for larger apertures relative to Spitzer Infrared Spectrograph, IRS (in this case, Multiband Imaging Photometer, MIPS, SED mode). The starlight model is in orange, ISM model in blue, the sum is in red. Lines show the best fit, and the shaded region shows the range of realizations for that model component (or sum). The systematic uncertainty is expected to be about 10%, indicated by dotted lines on the residuals plot. The statistical noise can exceed 10% for the short wavelength end of the IRS spectrum. 124
- 5.4 The in-band spectral index image of NGC 2639 in color with 5 GHz radio contours superimposed. Contour levels: $50 \times (1, 2, 4, 8, 16, 32, 64, 128, 256, 512) \mu\text{Jy beam}^{-1}$. The beam shown in the lower left corner is of size $1.15'' \times 1.00''$ at PA = -4.9° 125

LIST OF FIGURES

- 5.5 The in-band rotation measure image of NGC 2639 in color with 5 GHz radio contours superimposed. Contour levels: $50 \times (1, 2, 4, 8, 16, 32, 64, 128, 256, 512) \mu\text{Jy beam}^{-1}$. The beam shown in the lower left corner is of size $1.15'' \times 1.00''$ at PA = -4.9° 126

LIST OF FIGURES

List of Tables

3.1	Observation log and observed parameters of NGC 3079.	48
3.2	Source parameters estimated from the “minimum energy” condition	59
4.1	Observation log and observed parameters.	76
4.2	Upper limit on fractional polarization	90
4.3	Kinetic energy injection rates due to jets, AGN radiation and SFR	111

LIST OF TABLES

List of Symbols & Abbreviations

h	Planck constant	c	Speed of light in vacuum, $\sim 3 \times 10^{10}$ cm s $^{-1}$
α	Spectral index, defined as $S_\nu \propto \nu^\alpha$	CASA	Common Astronomy Software Applications
χ	Polarization angle, EVPA	Chandra	Chandra X-ray Observatory
λ	Emission wavelength	CHANG-ES	Continuum Halos in Nearby Galaxies Survey, with the VLA
ν	Emission frequency	CSS	Compact Steep Spectrum source
z	Redshift	DSA	Diffusive Shock Acceleration
ADAF	Advection Dominated Accretion Flow	e-MERLIN	enhanced Multi-Element Radio-Linked Interferometer Network, UK
AGN	Active Galactic Nuclei	EVPA	Electric Vector Position Angle, χ
AIPS	Astronomical Image Processing System	FIRST	Faint Radio Images of the Sky at Twenty Centimeters, survey with the VLA
ALMA	Atacama Large Millimeter/submillimeter Array, Chile	FP	Fractional Polarization
B	Magnetic field	FR	Fanaroff Riley
BL Lac	BL Lacertae object	FSRQ	Flat Spectrum Radio Quasar
BLR	Broad Line Region	FWHM	Full Width at Half Maximum
BPT	Baldwin, Phillips & Terlevich, diagnostic diagram for distinguishing between Seyfert, LINER and star forming galaxies	H₀	Hubble constant, we adopt $H_0 = 73$ km s $^{-1}$ Mpc $^{-1}$
		HBL	High energy peaked BL Lac object
		Herschel	Herschel Space Observatory
		HST	Hubble Space Telescope
		IFU	Integral Field Unit
		ISM	Inter Stellar Medium
		kpc	Kiloparsec, 10^3 pc
		KSR	Kiloparsec-scale Radio Structure
		L_⊙	Solar luminosity, 4×10^{33} erg sec $^{-1}$

LIST OF SYMBOLS & ABBREVIATIONS

LBL	Low energy peaked BL Lac object	QSO	Quasi Stellar Object
LINER	Low Ionisation Nuclear Emission line Region	RL	Radio Loud
LLAGN	Low Luminosity AGN	RLQ	Radio Loud Quasar
M_{\odot}	Solar mass, $\sim 2 \times 10^{33}$ g	RM	Rotation Measure
mas	Milliarcsecond	RQ	Radio Quiet
MHD	Magneto Hydrodynamic	S_{ν}	Flux density at frequency ν
Mpc	Megaparsec, 10^6 pc	SDSS	Sloan Digital Sky Survey
MS-MFS	Multi-Scale Multi-Frequency Synthesis	SED	Spectral Energy Distribution
NLR	Narrow Line Region	SFR	Star Formation Rate
NLS1	Narrow line Seyfert 1	SMBH	Supermassive Black Hole
NVSS	NRAO VLA Sky Survey, with the D-array VLA at 1.4 GHz	SNR	Signal to Noise Ratio
OVV	Optically Violently Variable quasar	Spitzer	Spitzer Space Telescope
PA	Position Angle, measured from north through east with north being at 0°	uGMRT	upgraded Giant Metrewave Radio Telescope, India
pc	Parsec, $\sim 3 \times 10^{18}$ cm	VLA	Very Large Array, USA
PSF	Point Spread Function	VLBA	Very Long Baseline Array, USA
		VLBI	Very Long Baseline Interferometry

1

Introduction

A small fraction of galaxies in the universe contains an active galactic nucleus (AGN) at their center. It is known that many of these AGN host radio jets, although the fraction of powerful jets often amount to only $\sim 10\%$ which can extend up to several hundreds of kpc or sometimes even up to a few Mpc. However, rarely do Seyfert galaxies host such powerful jets. Understanding the nature of these low powered jets including their power, speeds, extents, environments, and other properties that might be impacting their growth and evolution is an important step towards understanding the mechanisms determining the launching and powering of jets in general. Since the jets in Seyfert galaxies are weak, it is often hard to distinguish the emission from jets and other possible contributors such as starburst superwinds, AGN winds, etc. It therefore becomes important to come up with strategies to disentangle the jet related radio emission from that related to other mechanisms like star formation, AGN accretion, etc. before addressing the more relevant questions related to jet formation. It was demonstrated by Irwin et al. (2017) that polarization can prove to be an effective tool in distinguishing the AGN jet related emission from that of the galactic disk radio continuum emission.

In this thesis, we have tried to use polarization data from the VLA to study a sample of Seyfert galaxies with the aim of disentangling the role played by the different mechanisms in the origin of the radio emission. In this Chapter, I present a general overview of the past and recent studies that were undertaken in this field of research and at the end I provide an outline of the thesis.

1. INTRODUCTION

1.1 AGN

AGN are the energetic centers of a small fraction of galaxies that exhibit a bright star-like nucleus and strong emission lines in their UV/optical spectra. These are now believed to be powered by the release of gravitational energy as matter accretes onto supermassive black holes (SMBH mass 10^5 – 10^{10} M_⊙) through accretion disks. Some of the observational characteristics of an AGN include high nuclear UV luminosity, strong and broad emission lines in the optical/UV/Infrared, variability in flux, presence of X-ray emission, and bipolar jets that are seen mainly in radio wavelengths.

1.1.1 Historical overview

In this section, we discuss a historical overview of the discovery and progress in the field of AGN. In 1908, E.A. Fath noted the presence of strong emission lines in the optical spectrum of the galaxy, NGC 1068. A higher-quality spectrum obtained by V.M. Slipher showed that the emission lines were unusually broad hinting at the presence of high-velocity gas in these systems. Later on, H.D. Curtis observed M 87, and noted the presence of a “curious straight ray” which was later identified as a relativistic jet that is being ejected from the active nucleus.

In 1943, Carl Seyfert recognized that a fraction of galaxies showed distinct properties from the rest of the population like strong broad emission lines. These galaxies were also observed to possess large nuclear luminosities and these galaxies came to be known as Seyfert galaxies. In 1959, Woltjer tried to explain the underlying physics of these Seyfert galaxies. They showed that these sources had sizes smaller than 100 pc and lifetimes larger than 10^8 years and mass in the range of $\approx 10^9$ M_⊙ from virial arguments.

Further down the line, several radio surveys were carried out that led to the identification of a lot of bright radio sources. Many of them were associated with galaxies and sometimes star-like objects. The 3C survey (Edge et al., 1959) had resulted in a catalog of radio sources at 158 MHz with a flux limit of 9 Jy and 3C 273 was one of the bright radio galaxies identified. In 1963, M. Schmidt discovered that 3C 273 had a redshift of 0.158. They named it a “quasi-stellar

radio source” or quasar, hundreds of thousands of which have now been identified (Pâris et al., 2018).

Zel’dovich and Novikov (1964) tried to determine the origin of these distinct properties in AGN and proposed that black holes could be a plausible driver. Lynden-Bell (1969) suggested that the centers of most of the galaxies in the nearby universe might contain “collapsed old quasars” referring to super-massive black holes which are growing with time.

1.1.2 Types of AGN

Based on the difference in the observational properties which led to their discovery, AGN are classified into several categories. All these categories were later on brought under the same umbrella by the unification scheme (Antonucci, 1993; Urry & Padovani, 1995). In this subsection, we discuss the various classes of AGN, their observations, and characteristic properties.

1.1.2.1 Seyfert galaxies

In 1943, Carl Seyfert identified six galaxies, namely, NGC 1068, NGC 1275, NGC 3516, NGC 4051, NGC 4151, and NGC 7469 showed broad and strong emission lines which were not present in typical non-AGN. These galaxies came to be known as ‘Seyfert’ galaxies. The search for ‘UV excess’ galaxies using a low dispersion spectroscopic survey by Markarian led to the discovery of many more Seyfert galaxies.

These were hosted mainly by late type galaxies like spirals and lenticulars. Around 1% of spiral galaxies show Seyfert galaxy like properties. With improvements in spectroscopic techniques, Khachikian & Weedman (1974) introduced a new scheme of classification based solely on their spectroscopic properties and also subdivided the entire class into two, Seyfert 1 and Seyfert 2. Permitted lines in Seyfert 1 galaxies showed broad line widths in the range of $1\text{--}10,000 \text{ km s}^{-1}$, whereas forbidden lines like [O III] did not show broad wings and had widths $\sim 1000 \text{ km s}^{-1}$. However, in Seyfert 2 galaxies both permitted and forbidden lines showed narrow widths ($\sim 1000 \text{ km s}^{-1}$).

1. INTRODUCTION

Osterbrock (1981) extended the classification to Seyfert galaxies which showed permitted lines which could be decomposed into two components, sources which showed broad component in H α but only a narrow component in H β and sources which do not show the broadening in the H β line termed as Seyfert 1.5, 1.8 and 1.9 respectively.

The narrow line emission is believed to be originating from the narrow line region (NLR) at distances of \sim 10 parsec (pc) to \sim 1 kiloparsec (kpc) from the nucleus, whereas the broad component is arising from the broad line region (BLR) which is much closer to the black hole (\sim 1 pc). The large line widths were hence attributed to the large gravitational influence of the black hole on the emitting region due to its proximity. The discovery of the hidden BLR in spectropolarimetric observations of Seyfert 2 galaxies (Antonucci, 1993), led to the unification scheme for AGN.

NLS1 galaxies form a subclass of Seyfert galaxies characterized by their small broad emission line widths (FWHM H β $<$ 2000 km s $^{-1}$) in comparison with typical values seen in type 1 Seyfert galaxies and the weakness of the [O III] λ 5007 emission line ([O III]/H β $<$ 3; Goodrich, 1989; Osterbrock & Pogge, 1985). Most of these sources are radio quiet (RQ) with only \sim 7% being radio loud (RL) (Kommossa et al., 2006).

Radio quiet AGN have radio loudness parameter, $R \leq 10$ as defined by Kellermann et al. (1989) where $R \equiv S_{\text{5 GHz}}/S_{\text{B-band}}$ with $S_{\text{5 GHz}}$ being the radio flux density at 5 GHz and $S_{\text{B-band}}$ being the optical flux density in the B-band at 4400 Å. Radio loud AGN have $R \gg 10$. A multi-wavelength study of these RL NLS1 by Foschini et al. (2015) suggests that the jet properties of these sources are similar to blazars and quasars when scaled with their black hole mass and attribute the low detection rate of RL NLS1s to their low net power and episodic jet activity.

1.1.2.2 Quasars

Quasars form the brightest sources among AGN with nuclear magnitudes, $M_B < -21.5 + 5 \log h_0$ (Schmidt & Green, 1983). These sources appear star-like (a.k.a. quasi-stellar objects, QSOs) and their host galaxies are often invisible due to

contamination from the point spread function (PSF) of the central source. Although first discovered as the optical counterpart of a bright radio source, further discoveries and optical surveys have suggested that only 5 – 10% of these are radio loud. Their properties resemble those of Seyfert galaxies, especially their optical spectra and the presence of broad emission lines with widths up to $\sim 10,000 \text{ km s}^{-1}$. The underlying IR-optical continuum follows a power law and peaks around $100 \mu\text{m}$, similar to Seyfert galaxies. An excess emission in the blue to UV regions is witnessed in some of these quasars and is termed as the ‘big blue bump’. This emission is interpreted to be arising from the hot accretion disk (Shakura & Sunyaev, 1973).

1.1.2.3 Radio galaxies

Powerful radio sources were identified using radio surveys from early on and form one of the first AGN classes to be identified. Most of these radio sources are associated with elliptical galaxies. Several of these radio galaxies extend far beyond the galaxy itself and sometimes reaching up to several Mpc in size. Radio galaxies have been classified into two classes based on their optical spectrum as low-excitation radio galaxies (LERGs) and high excitation radio galaxies (HERGs) (Hine & Longair, 1979). Laing et al. (1994) classified those galaxies which possess $[\text{O III}]/\text{H}\alpha > 0.2$ and equivalent widths of $[\text{O III}] > 0.3$ as high excitation and the rest as low excitation galaxies.

Based on the radio morphology and total radio power, radio galaxies were divided into two classes, FR I and FR II (Fanaroff & Riley, 1974). The lower power FR Is display wide jets that flare into plume-like radio lobes away from the centre, whereas the higher power FR IIs display narrow collimated jets that terminate in regions of high surface brightness called “hotspots”; the trailing or backflowing plasma forms the radio lobes. While the FR dichotomy has been a long standing puzzle in AGN physics, it has been suggested to be a result of either intrinsic differences in the central engines (e.g., Baum et al., 1995; Meier, 1999; Zirbel & Baum, 1995), or differences in environment (e.g., Bicknell, 1995), or both. Environmental influences including entrainment of surrounding material or injection of stellar ejecta (e.g., Bicknell, 1994, 1995; Komissarov, 1994) and development of

1. INTRODUCTION

Kelvin Helmholtz (KH) instabilities in the shear layers (e.g., Kaiser & Alexander, 1997; Perucho et al., 2005) have often been invoked to explain jet deceleration. It has also been suggested that FR II radio galaxies form as a result of mergers whereas FR I radio galaxies form from gradual feeding from the ambient medium like hot IGM (e.g., Emonts et al., 2008; Saripalli, 2012) although mergers have been invoked to explain specific examples of FR I radio galaxies as well (e.g., Das et al., 2005).

1.1.2.4 LINERs

Low ionization nuclear emission-line region galaxies or LINERs (Heckman, 1980) are galaxies which possess emission lines that are not as spectacular in terms of strength or ionization state as the Seyfert galaxies. Their low-ionization lines like [O I] $\lambda 6300$ and [N II] $\lambda\lambda 6548, 6583$ are stronger compared to Seyfert galaxies. The line ratios [OIII]/H β alone can not be used to identify LINER galaxies because HII regions with low metallicity also show similar ratios. Baldwin et al. (1981) showed that AGNs can be separated from the starforming galaxies by using two different line ratios rather than just one. In the BPT diagram, LINERs occupy the region which manifests lower values of [O III] $\lambda 5007$ /H β for similar values of the line ratio, [N II]/ $\lambda 6583$ /H α compared to the Seyfert galaxies. On the other hand, the LINERs have higher values of [N II] $\lambda 6583$ /H α compared to the star-forming galaxies. The LINER type nuclei are found mostly in spiral galaxies and are also known to comprise about half of the population of the spiral galaxies (Ho et al., 1997). While these sources are usually identified using its flat spectrum radio cores and central X-ray emission, their optical emission is relatively weak and is often hard to disentangle from the host galaxy emission.

1.1.2.5 Blazars

Blazars form a category of AGN that are characterized by extreme variability, high levels of optical polarization, radio-loudness, and the presence of a broadband continuum emission ranging from the radio to the γ -rays. Blazars often show optical variability on short time-scales including both intra-night and inter-night variability (Stalin et al., 2006). Blazars comprise optically violent variable (OVV)

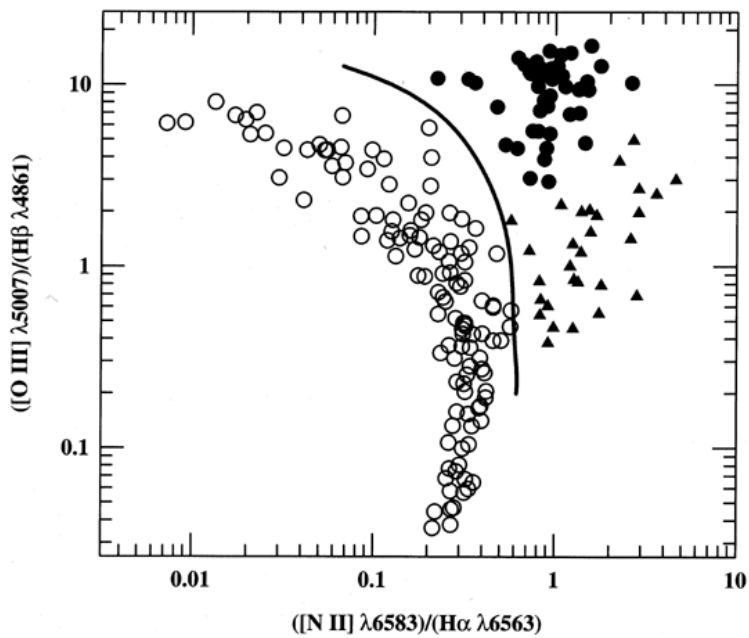


Figure 1.1: Baldwin, Phillips and Terlevich (BPT) diagram to distinguish between various types of sources. The triangles, open circles and filled circles represent, LINERs, HII regions and Seyfert galaxies respectively. Figure taken from Peterson (1997). Credits: R.W. Pogge using data from Veilleux & Osterbrock (1987)

1. INTRODUCTION

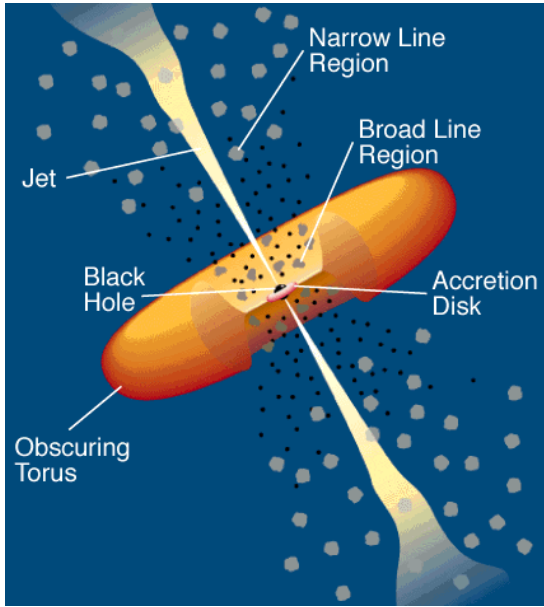


Figure 1.2: Schematic illustrating the anatomy of the standard unified model of AGN (Urry & Padovani, 1995).

quasars and BL Lac objects (Angel & Stockman, 1980). Radio follow-up using VLBI techniques shows that many of them display apparent superluminal motion in their jets (Readhead et al., 1978). All these properties are indicative of a relativistic jet that is inclined close to our line of sight. The BL Lac objects are again subdivided into high energy peaked sources (HBLs) and low energy peaked sources (LBLs) (e.g., Giommi & Padovani, 1994; Padovani & Giommi, 1995). The primary difference between flat spectrum radio quasars (FSRQs) and BL Lacs is that the former show strong emission lines, whereas the latter show either weak or no emission lines in their optical spectrum.

1.1.3 Unification Scheme

The AGN were initially identified due to the immense amount of radiation coming from a compact region. From the earlier studies, it is apparent that there were several sub-classes of AGN, discovered at various wavelengths. The unification scheme posits that these are all the same basic phenomenon, but these sub-classes look different based on other factors like their inclination angle, or environments

(Antonucci, 1993; Urry & Padovani, 1995). In this section, we describe the different components of AGN.

1.1.3.1 Supermassive Black Hole

According to our current understanding, almost all the galaxies harbor a supermassive black hole at its center (e.g., Genzel et al., 2003; Ghez et al., 2008). The masses span several orders of magnitude from $\sim 10^5 - 10^{10} M_\odot$. The gravitational pull of the SMBH is responsible for accreting the matter towards it which results in the accretion disk, which in turn is responsible for the bright emission seen at the center of these objects. Moreover, the jets seen in these AGN are also thought to be launched using the power extracted from the rotation of the SMBH (e.g., Blandford & Znajek, 1977; McKinney & Narayan, 2007; Mor et al., 2009).

In 1916, Karl Schwarzschild found the solution to the general relativistic (GR) equations for a non-rotating but spherically symmetric black hole. In 1963, Kerr generalized these equations to define a rotating black hole. According to the no-hair theorem, any solution describing a black hole in the framework of gravitation and electromagnetism can be completely described using only three observable quantities, which are the mass, charge, and the spin of the black hole.

A major leap in this field was achieved with the imaging of the SMBH shadow at the center of M87 which was made possible using the high angular resolution (~ 20 micro-arcseconds) possible using the Event horizon telescope, EHT (Event Horizon Telescope Collaboration et al., 2019a,b,c,d).

1.1.3.2 Accretion Disk

Accretion is a necessary condition for the powering of AGN, gamma-ray bursts, black hole X-ray binaries, and the launching of jets. The clouds that are under the gravitational influence of the central black hole experience frictional forces acting on them forcing them to go round the SMBH in a disk or the “accretion disk” (Shlosman et al., 1990). One of the best known models of an accretion disk is the “geometrically thin optically thick disk” by Shakura & Sunyaev (1973). The emission from this accretion disk is black-body in nature. The accretion rates are lesser than the Eddington accretion rates and so is the radiative luminosity. As

1. INTRODUCTION

a result, the temperature ranges from 10^{4-7} K for the material in the disk, which is smaller than the virial temperature.

However, when the mass accretion rates are high and close to the Eddington limit, the accretion disk becomes too luminous to be able to radiate away all the energy locally, which is an approximation used in the thin-disk model. The radiation gets trapped inside due to the high optical thickness and is transported along with the accreting matter towards the SMBH. The solution of the accretion disk, in this case, is known as the optically thick advection dominated accretion flows (ADAF) or the slim disk.

Another model of the accretion disk is the hot accretion flow model, where the temperature is near virial and the gas optically thin (Narayan & Yi, 1994, 1995; Shapiro et al., 1976). These are radiatively inefficient and have been applied to sources with low rates of mass accretion like low luminosity AGN, Sgr A*, etc.

1.1.3.3 Dusty Obscuring Torus

The obscuring torus was invoked to unify the different types of AGN (Antonucci, 1993; Urry & Padovani, 1995). The torus was proposed to have a doughnut shape surrounding the central engine and composed of dust that emits mainly in mid-infrared after reprocessing the accretion disk emission (Krolik & Begelman, 1988). It has a size ranging from 0.1 to 10 pc as constrained using MIR interferometric and sub-millimeter observations. Recent IR and X-ray studies have shown that the structure of the torus is clumpy (e.g., Hönig et al., 2010; Markowitz et al., 2014). Due to the high angular resolution provided by Atacama Large Millimeter/submillimeter Array (ALMA), the structure of the torii has been revealed to some extent (e.g., Gallimore et al., 2016; Imanishi et al., 2016; Marinucci et al., 2016; Mor et al., 2009). The sub-mm wavelength gives information about the cooler regions of the torus, which lie towards the outer regions from the accretion disk. It shows that the outer regions of the torii are not stand alone structures and appear more like an extension of the circumnuclear disk.

Moreover, MIR interferometry revealed that it requires a two component model rather than a single component to fit the data (Ramos Almeida et al., 2009). An elongated polar structure is often seen along with the equatorial

component and also appears brighter. The poloidal component is interpreted as outflowing material due to radiation pressure. In a recent study by Perley et al. (2019) the emission from the doughnut shaped torus in Cygnus A has been captured with sensitive observations using the Karl G. Jansky VLA.

1.1.3.4 Broad Line Region

One of the distinguishing characteristics of an AGN is the broad and strong emission lines present at the center of these systems. It has been established that the BLR is confined close and gravitationally bound to the black hole and hence possess high-velocity widths ($\sim 10,000 \text{ km s}^{-1}$). The BLR is dense (electron density, $n_e \sim 10^{11} \text{ cm}^{-3}$; Peterson, 1997) and hence suppresses all the optical forbidden lines.

The size and structure of BLR is still an area of active research. Reverberation mapping is a technique widely employed to understand the size and structure of the BLR (Mejía-Restrepo et al., 2016; Peterson, 1997). Greene & Ho (2005) present an extensive study to determine black hole masses from the broad emission line observations. They show that the broad emission lines are well correlated with the optical continuum luminosities and the size of the BLR.

The BLR has been widely considered to possess a spherical distribution of clouds around the black hole. High ionization lines like He II, He I, O VI, N V, and C IV are thought to be produced from regions near the black hole, whereas the low ionization emission lines like Mg II, Ca II, O I, and Fe II are produced further away. The outer edge of the BLR is also often seen to coincide with the inner edge of the dusty torii (Peterson, 1997).

1.1.3.5 Narrow Line Region

The narrow line region forms the lower density emission line cloud region around the AGN that typically can extent up to kpc scales (Bennert et al., 2006; Peterson et al., 2013). As these lie farther away compared to the BLR, their velocity widths are smaller ($\sim 200 - 500 \text{ km s}^{-1}$). Also, since the densities are lower ($n_e \sim 10^3 \text{ cm}^{-3}$), several magnetic dipole transitions are possible. The forbidden

1. INTRODUCTION

emission lines like $[\text{O III}]\lambda 5007 \text{ \AA}$ and $[\text{N II}]\lambda 6582 \text{ \AA}$ are found to dominate the NLR spectrum.

The unification scheme unified the type 1 and type 2 AGN as a single category and argued that the difference in the emission line spectrum arose as a result of viewing angles (Antonucci, 1993; Urry & Padovani, 1995). When the line of sight coincides with the plane of the disk, the obscuring torus blocks out the emission from the BLR whereas the NLR extends beyond the torus and hence can be viewed from any angle. Hence these sources were classified as type 2 whose emission line spectra only showed the presence of narrow forbidden and permitted emission lines and an absence of broad lines. On the other hand, the sources in which the line of sight coincides with the axis of the accretion disk show both broad permitted emission lines along with the narrow lines and these sources were classified as type 1 AGN.

1.1.3.6 Jet

Although the first jet was identified in the optical waveband by H. Curtis as described in Section 1.1.1, it was the advent of radio astronomy that led to the major observational progress in the field of AGN jets. Jennison & Das Gupta (1953) resolved the bright radio source associated with Cygnus A into two different lobes. Several double sources were identified thereafter, most of them hosted by massive elliptical galaxies. The discovery of the first quasar, 3C 273 was also made possible due to the presence of the bright radio emission from the galaxy. Rees (1966) suggested that these jets possess relativistic motion due to the rapid variability observed in these systems. Rees (1971) concluded that these jets are powered by the AGN rather than other powerful explosions like supernovae.

The composition of the jet is to date an open question. Many suggestions including particle (leptonic as well as for hadronic) and electromagnetic models have been proposed in the literature (see Böttcher (2007) for a review). Jets are also possible candidates for accelerating the high energy cosmic rays (Blandford et al., 2019). In a recent study, a single neutrino (energy $\sim 400 \text{ TeV}$) was associated with a blazar, TXS 0506+056 providing some supporting evidence for this picture (Aartsen et al., 2017). We give a more detailed discussion on jets in Section 1.2

1.2 Formation of Relativistic Jets in AGN

Jets are thought to be composed of relativistic particles that are launched from close to the black hole. The radio emission in AGN spans several orders (~ 6) of magnitude despite similar spectral energy distribution (SED) at all other wavelengths. The disparity is also seen in the extents with a small fraction of AGN producing jets that extend up to sizes of several Mpc known as giant radio galaxies (e.g., Schoenmakers et al., 2000) whereas a larger fraction showing compact cores at the center of the galaxy (e.g., Wrobel & Heeschen, 1988, 1991). Synchrotron mechanism was invoked to explain the radio emission, owing to the high degrees on polarization and the power-law spectrum seen in these sources. There are still several open questions in the field of jet physics, including the launching mechanism, acceleration, content of the plasma, velocities, and the collimation of the jet material.

Three different models of jets are usually considered in the literature although the most favored model is the magnetohydrodynamic model. Blandford & Rees (1974) proposed the jet model, which would make use of a ‘de Laval’ nozzle from the external gas pressure to push the matter into a channel with supersonic velocities. Radiation forces were also considered as a mechanism for jet launching although it was subsequently ruled out due to its inability to provide adequate acceleration.

The magneto hydrodynamic mechanism on the other hand has been widely successful in explaining the relativistic velocities, and the collimation. The ordered magnetic fields can be generated as a result of the dynamo mechanism in the accretion disk. Blandford & Znajek (1977) explains how the rotational energy of the black hole in the vicinity of a magnetic field can be extracted as the electromagnetic power to launch the jets. Collimation is a natural expectation in the case of MHD jets because the footpoint of the field lines anchored to the disk will start to rotate which will lead to the generation of toroidal magnetic fields. These toroidal magnetic field lines will then exert a pressure inward on the jet material which keeps the outflowing material collimated.

General-relativistic magnetohydrodynamic (GRMHD) modeling has been instrumental in developing our current understanding of jets (e.g., Meier, 2012;

1. INTRODUCTION

Nakamura et al., 2018). Several studies like those by Gammie et al. (2003); McKinney (2006) have shown that jets can be produced by rotating and accreting black holes whose jet power increases as a function of the SMBH spin.

From both observational and theoretical studies, several factors are proposed to play a role in the jet formation. Some of these parameters are the mass and spin of the SMBH, accretion rates, the state of accretion, and the strength of the magnetic fields threading the accretion disk. We discuss the current understanding of what constitutes the central engine that determines the launching and properties of the jet in the following subsections.

1.2.1 Accretion Rate and Black Hole Mass

While it is understood that accretion is a necessary condition from observations of the variety of astrophysical sources, it is not yet clear that it is a sufficient condition for the launch of jets. Observational studies of many black hole X-ray binaries reveal a connection between the accretion disc and the jet. The identification of the fundamental plane of black hole activity (Falcke et al., 2004; Merloni et al., 2003) substantiated such a coupling even in AGN. It suggests that the core radio luminosity varies as a function of both black hole mass and X-ray luminosity which probes the accretion disk.

1.2.2 Black Hole Spin

Sikora et al. (2007) studied how the radio loudness was coupled with the Eddington ratio in two different samples of AGN, one optically selected, and the other radio selected. They find that the sources in both these samples separate into two distinct sequences, which they suggest is a result of the SMBH spin. They suggest that the RL population which is often hosted by ellipticals and the RQ AGN which are hosted by disk galaxies have different BH spins and hence the gap. However, this would require that ellipticals that host RQ quasars also have SMBH spins similar to disk galaxies.

Reynolds (2014) compiled the SMBH spin of 22 galaxies which have been measured to date. A significant number of these galaxies are rapidly spinning (SMBH spin, $a>0.8$). They reject the SMBH spin paradigm because all of them

are radio quiet and a majority are hosted by late type galaxies. An alternate explanation is that the mode of accretion causes the gap rather than the SMBH spin.

1.2.3 Accretion State

It was proposed that the difference in jet power is a result of the two modes of accretion, namely from the radiatively efficient thin disks and the radiatively inefficient thick disks which have advection dominated accretion flows (Best & Heckman, 2012).

1.2.4 Magnetic Flux

Sikora & Begelman (2013) propose the magnetic flux paradigm, where they suggest that the magnetic flux threading the black hole plays the deciding role in determining the jet properties rather than both the spin and the accretion rate. The magnetic flux in turn was proposed to depend on the mode of accretion.

1.3 Radio Emission from Seyfert Galaxies

Several radio interferometric imaging surveys at 1.4 and 5 GHz with $\sim 1''$ resolution were carried out on samples of Seyfert galaxies (e.g., Ho & Ulvestad, 2001; Leipski et al., 2006; Morganti et al., 1999; Ulvestad & Wilson, 1984a,b; Ulvestad et al., 1981). Radio structures often extending up to several 100s of parsecs (mostly 500 pc) were commonly identified in these Seyferts. Many of these showed bright cores, while some of them also showed linear features like double and triple structures that straddled the optical core similar to powerful radio sources. Diffuse radio emission around the nuclei was also often identified in many of them, the origin of which was sometimes attributed to star-formation. Investigations of the radio spectra have revealed that most of these Seyfert galaxies possess steep spectrum radio emission ($\sim 90\%$) (e.g., Edelson, 1987; de Bruyn & Wilson, 1978). Giuricin et al. (1990) also find that it is more probable for Seyfert type 1 galaxies to show flat spectrum cores.

1. INTRODUCTION

The radio structures were aligned perpendicular to the optical polarization. The mechanism for the production of optical polarization is dust scattering. Radio polarization on the other hand, is not detected in most cases probably due to the depolarization effects from the dense gas surrounding the radio emission. Another interesting finding was the correlation between the radio emission and the [O III] emission both in terms of luminosity and also the line widths. Further studies explored both higher resolutions and lower resolution imaging of these sources. Very high angular resolution studies (\sim mas) using telescopes like VLBA and e-MERLIN found that many of them hosted significant radio emission on pc scales (e.g., Baldi et al., 2018; Kukula et al., 1999; Mundell et al., 2000; Orienti & Prieto, 2010; Panessa & Giroletti, 2013; Thean et al., 2001; Ulvestad & Wilson, 1989; Unger et al., 1987).

The first imaging surveys of Seyfert galaxies were carried out using the Westerbork telescope which produced low resolution ($\sim 25''$) images of these sources (e.g., de Bruyn & Wilson, 1976, 1978). The sensitivity of these observations was limited and did not reveal the diffuse low surface brightness features. The high angular resolution studies, on the other hand, suffered from the inadequacy of short baselines required for recovering any diffuse emission on the scales of kilo-parsecs.

To be able to recover any diffuse emission that may have been missed in the previous studies, Baum et al. (1993) and Colbert et al. (1996a) carried out low-resolution imaging studies of samples of Seyfert galaxies. These sensitive low-resolution studies revealed that many of these Seyfert galaxies hosted elongated radio structures that extended up to several kpc. The origin of the radio emission was however widely debated in the literature. While Baum et al. (1993) favored a starburst related origin, Colbert et al. (1996a) who contrasted the properties of a sample of starburst galaxies with those of a Seyfert sample, suggested that the radio emission in Seyfert galaxies is jet related.

Gallimore et al. (2006) carried out a more comprehensive study for a sample of 43 Seyfert galaxies and they find that at least 44% of Seyfert galaxies host kiloparsec scale radio structures (KSRs). Seyfert galaxies were classified as KSRs when the central-point source subtracted radio images showed extended residual emission of sizes larger than 1 kpc without an obvious counter part in optical

1.4 Possible mechanisms for the origin of radio emission

emission from the host galaxy. As a result 44% is a lower limit owing to the effects of inclination angle as well as the resolution of the observations.

More recently, the study of KSR emission from a large sample of Seyfert galaxies and LINERs using both FIRST and NVSS images finds that >30% of Seyferts host KSRs (Singh et al., 2015). On the other hand, the fraction of NLS1s hosting KSRs is smaller (e.g., Singh & Chand, 2018). There is still no consensus on the mechanism that plays a major role in the origin of the radio emission seen in these galaxies.

1.4 Possible mechanisms for the origin of radio emission

Several mechanisms have been proposed to explain the radio emission in Seyfert galaxies. It is important to understand the role played by each in the origin of the radio emission from RQ AGN because characterizing low power jets are required to fill our gaps in the understanding jet formation. It is also important to understand the role each of these mechanisms plays in AGN feedback and galaxy evolution (e.g., Harrison, 2017; Harrison et al., 2018; Jarvis et al., 2019). In this section, we discuss the different mechanisms for the origin of kpc-scale radio emission observed in Seyfert galaxies.

1.4.1 Starburst driven winds

It has been suggested in the literature that the radio emission seen in Seyfert galaxies owes its origin to star formation rather than the AGN (Baum et al., 1993). Starburst driven winds have been well studied in the literature (e.g., Bland-Hawthorn et al., 2007; Heckman et al., 1993; Rupke, 2018; Veilleux et al., 2005; Zhang, 2018). In starburst galaxies, star formation is accompanied by a large number of supernovae. The high velocity ejecta from supernovae and stellar winds leads to shocks which in turn leads to the effective conversion of the kinetic energy into thermal energy. Little energy is then lost as radiation. As a result, the interstellar medium (ISM) is filled with hot gas (with temperatures as high

1. INTRODUCTION

as 10^7 K) heated by the supernovae and stellar ejecta, which then expands like a bubble of hot and overpressured gas.

Initially, it cools adiabatically via expansion and sweeps up a layer of shocked ISM at the boundary of the bubble. The swept up layer leads to the deceleration of the boundary and the expansion speed becomes smaller than the wind velocity. After the end of such a free expansion phase, the system is characterized using five regions. These regions, going radially from the center to the edge of bubbles, are (i) source of energy injection or the starburst, (ii) a freely expanding wind, outside the central injection region, (iii) shocked wind region, (iv) the shocked ISM region and (v) the undisturbed ISM. At some point during the expansion, it is also possible that the expanding wind enters a blow-out phase, which occurs as a result of Rayleigh-Taylor instabilities.

1.4.2 AGN accretion driven winds

Broad absorption line (BAL) features seen mainly in the UV spectra of some quasars known as BAL quasars are suggestive of the presence of AGN driven winds in these systems. These lines are usually blue-shifted indicating outflowing gas, although there are also cases of red-shifted absorption lines. Sometimes, even narrow absorption lines are attributed to the outflowing winds. These are found at large velocity offsets as high as $50,000 \text{ km s}^{-1}$ (Hamann et al., 1997). Such broad and narrow absorption lines are also seen in optical as well as the X-ray spectrum.

Ionized outflows seen in X-rays known as “warm absorbers” are observed in a major fraction of Seyfert 1 galaxies. Ultrafast outflows (UFO) seen in X-rays (Pounds, 2014; Tombesi et al., 2010), with velocities as high as $\sim 0.5c$ are also identified using the absorption features seen in the broad Fe $K\alpha$ line feature. These UFOs occur close to the black hole gravitational radii.

More recently, advances in observing capabilities including the advent of high resolution integral field unit (IFU) capabilities in IR. Herschel Space Observatory and ALMA have also shown the presence of galactic scale outflows of molecular neutral and ionized gas (e.g., Feruglio et al., 2010; Fischer et al., 2010; Rupke & Veilleux, 2011). Observational studies using various telescopes including HST

1.4 Possible mechanisms for the origin of radio emission

conclude that these outflows are neither simply spherical nor axially symmetric. Several mechanisms were proposed as the driving mechanism for the outflows in the literature. Some of these are elaborated in this section.

These winds are supersonic compared to the ambient medium leading to the generation of both forward shocks (shocking the ambient medium), the reverse shocks (shocking the wind material) and a contact discontinuity. Radio emission can be generated via diffusive shock acceleration (DSA) at these shock fronts (Blandford & Eichler, 1987) which leads to pushing a thermal population of electrons into relativistic velocities. Magnetic fields are also amplified via shock compression at shock fronts. In both thermally driven and radiatively driven cases, this is the way the radio emission can be generated. On the other hand, in the case of magnetically launched winds, both the relativistic population of electrons and magnetic fields are supplied from the central engine.

Another possible way for the generation of the radio emission from these winds is via the thermal Bremsstrahlung (free-free) emission from an optically thin photoionized gas (e.g., Blundell & Kuncic, 2007; Blustin & Fabian, 2009). In such a case, we would expect a spectral index value of -0.1 . However, many studies of radio emission from radio quiet AGN find the spectrum to be steep.

1.4.2.1 Radiation pressure driven winds

Radiation pressure was proposed as a plausible driver for the outflows seen in BAL QSOs early on, given the impressive amounts of radiation from centers of AGN (e.g., Scargle et al., 1970; Shlosman et al., 1985). The winds have their origin at the accretion disk radii where the UV continuum emission is produced. The mass loss rates and velocities estimated from the blue-shifted broad absorption lines are consistent with such a scenario. ‘Line-locking’ is another observational property that helped in filling the gaps in our understanding of these winds. The line force is a favorable mechanism that can explain these winds, given the gas is moderately ionized (e.g., Proga, 2007; Vaidya et al., 2011). The UV continuum from the disk interacts with this gas through several UV line transitions.

A difficulty in this model is that for a fully ionized gas, the radiation pressure is only via electron scattering. For the ionized gas to overcome gravity and be

1. INTRODUCTION

affected dynamically, the radiative luminosity will need to be above the Eddington limit. Nevertheless, if the gas opacity (proportional to density and inversely proportional to temperature) is higher than that of electron scattering, radiation driven winds can occur.

However, the X-rays produced from close to the black hole can lead to high ionization of the gas, such that the density is low and hence the opacity is negligible to have any effective radiation driven outflow of the gas. If there is shielding of the X-ray flux by some material with a high column density, then this problem can be overcome to some extent. Observationally, it was seen that the systems hosting BAL quasars show weak X-ray powers (Gallagher et al., 2006).

1.4.2.2 Thermally driven winds

When the X-rays from the central engine can heat the gas to high temperatures ($>10^7$ K) and when this hot gas has energies exceeding the escape velocities, they are launched as a thermal wind. While the outflow signatures seen in X-rays are attributed to this mechanism, the radiatively driven model is favored in the case of the low temperature plasma as probed by UV.

A problem of the model is, however, the adiabatic cooling that comes into play which makes it hard to explain large scale thermal winds (Everett & Murray, 2007). Turbulent heating was introduced as a possible mechanism to reverse the effects of cooling (Chelouche & Netzer, 2005).

1.4.2.3 Magnetically driven winds

The accretion disk is believed to be threaded by magnetic fields which upon rotating apply a centrifugal force on the matter (Blandford & Payne, 1982). The poloidal magnetic fields that thread the accretion disk were initially shown to transport the angular momentum via electromagnetic waves. Later on, it was also shown that this centrifugal force helps in accelerating the material outwards via the field lines, along with which it also transports the angular momentum outwards, which is required for the accretion of matter onto the SMBH (Everett, 2007).

1.4 Possible mechanisms for the origin of radio emission

There are two possible scenarios for magnetized winds. When the Alfvén velocities near the disk are much higher than the gas sound speed, the plasma which is frozen-in with the field lines is pushed outwards.

In cases where the Alfvén velocities are lower than the orbital velocities and poloidal magnetic fields are aligned at an angle greater than 30° from the rotation axis, the matter in the disk feels a potential and has an unstable solution. As a result, the matter moves outwards and as it progresses, its velocity also increases due to the reduced effect of gravity. The reaction force of the matter on the field lines also generates helical magnetic fields, which results in the collimation of the outflow itself (see Krolik, 1998, for more details). However, it is not yet clear how these magnetic fields arise in the first place. A plausible explanation is via the shearing of fields in the loops of corona seen above the accretion disk (Everett, 2007).

1.4.3 AGN Jets

Another widely discussed possible mechanism for the origin of radio emission, especially that seen on kpc-scales in Seyfert galaxies is from jets that are launched from the central engine. Colbert et al. (1996a) who studied a sample of star forming galaxies along with a sample of Seyfert galaxies, and found that there are several morphological differences, with the Seyferts showing more narrow or confined structures while the starburst galaxies showed more diffuse and spherically symmetric structures. Also while the starburst radio emission was aligned with the minor axis, the Seyfert KSR is not always aligned with the minor axis.

Gallimore et al. (2006) also showed that the KSR hosting Seyferts showed a “radio excess” suggesting a jet origin of the radio emission. However, the possibility of shock acceleration due to winds leading to an excess radio emission cannot be ruled out.

1.4.4 Coronal emission

X-ray emission seen in AGN is often attributed to having its origin in the hot corona with temperatures of the order of 10^9 K situated close to the black hole

1. INTRODUCTION

($10 - 10,000 r_g$;¹ Haardt & Maraschi, 1991, 1993). The emission itself is produced as a result of the inverse Comptonization of the optical/UV emission that comes from the accretion disk. Several X-ray studies suggest that the corona has a slightly complex structure requiring two components to explain the X-ray spectral features including soft excess and the underlying power-law component (e.g., Crummy et al., 2006; Dewangan et al., 2007).

The proposition that the radio emission seen in RQ AGN is related to coronal emission was a result of the correlation between X-ray and radio emission seen in some AGN (e.g., Brinkmann et al., 2000; Panessa & Giroletti, 2013; Panessa et al., 2007, 2015; Salvato et al., 2004). Moreover, it was shown by Laor & Behar (2008) that the slope of the radio to X-ray luminosity ($\sim 10^{-5}$) turned out to be consistent with the well known relation applicable for cool stars with coronal emission. However, in Seyfert galaxies, we often see a high fraction of them ($\sim 44\%$; Gallimore et al., 2006) showing emission on kpc scales, bringing the coronal origin of the radio emission into question.

1.5 Diffusive shock acceleration and magnetic fields

In this section, we discuss how the thermally and radiation pressure-driven winds lead to radio emission via shocks. Fermi (1949) proposed that the cosmic rays get scattered by waves leading to their isotropization. A turbulent magnetic field was proposed to be able to scatter plasma in a cloud to attain isotropy. Since the head-on collisions are more frequent, and eventual acceleration of particles leading to a power-law energy distribution was expected to occur.

Later, in the seventies, it was identified by several authors (e.g., Blandford & Icke, 1978) that such a mechanism is more favorable to occur at shock fronts. This mechanism was termed as the diffusive shock acceleration (DSA). So when particles are crossing the shock they are first faced with head-on collisions. The predicted spectral index of the power-law matches well with the observations of the cosmic rays reaching the earth.

¹ r_g is the gravitational radius of a rotating black hole, $\sim GM/c^2$;

1.6 Polarization properties of radio outflows

DSA occurs when the cosmic rays are scattered to a different angle by the magnetic field fluctuations on both sides of the shock. When such a scattered particle recrosses the shock it gains some amount of energy namely u_s/c where u_s is the shock velocity. To accelerate a cosmic ray particle to PeV energies, the particle will have to cross and recross the shock $10c/u_s$ times.

Shock compression can lead to magnetic field amplification and Laing (1980) proposed a model to explain the amplification of the ordered magnetic fields leading to a greater degree of polarization along the shock fronts. However, the magnetic field amplification seen in shocks in astrophysical systems like supernova remnants can not be explained merely by shock compression. It was proposed by Bell & Lucek (2001) that the non-resonant streaming instability which leads to the amplification of magnetic fields near the shock front occurs due to a current generated by particles that were accelerated by the forward shock.

1.6 Polarization properties of radio outflows

In this section, we summarize the polarization properties of the radio emission seen in star forming galaxies versus that seen in typical AGN jet features.

1.6.1 Galactic Dynamo

The evolution of magnetic fields in galaxies is a three step process, namely the seeding, the amplification, and the ordering (Beck, 2015). While seed magnetic fields can be explained using various models like the primordial fields (Durrer & Neronov, 2013), the Weibel instability (Lazar et al., 2009), the Biermann batteries (Hanayama et al., 2005) etc., the dynamo mechanism is employed to explain magnetic field amplification. Another possible mechanism was a turbulent dynamo, as proposed by Kulsrud & Anderson (1992). The mean field dynamo or the $\alpha\omega$ dynamo mechanism that plays a role in the generation of the large scale ordered magnetic fields seen in spiral galaxies requires turbulent motions as well as differential rotation.

The Continuum Halos in Nearby Galaxies (CHANG-ES) survey now provides polarization sensitive VLA observations of a sample of edge-on galaxies and has

1. INTRODUCTION

contributed to broadening our understanding the halos in a general population of galaxies (Irwin et al., 2019a,b). It was shown by Krause et al. (2020) that the magnetic fields in galaxies with halos show an X-shaped morphology for the polarization angle structures in the halo. The scales of the emission is comparable to that of the galaxy itself.

1.6.2 Magnetic fields in jets

Pacholczyk (1977) have summarized the polarization properties of regular radio galaxies. It is found that the net linear polarization from emission integrated over the entire source ranges from 0% to 6%, whereas extended structures show degrees of polarization as high as 70%. The position angle of the polarization seemed to show no dependence on the position angle of the jet itself. Magnetic fields were ordered on large scales sometimes, as high as kpc were found. Rotation measures (RM) showed large variations across the source axis and also between different components.

1.7 Jet-NLR interaction

The emission lines seen in NLR was attributed to photo-ionization by the broadband continuum emitted from the accretion disk. However, Binette et al. (1993) has argued that the amount of the continuum emission is not enough to explain the line emission seen through photo-ionization. Several studies have shown that the radio emission in AGN is correlated to the [O III] line emission (e.g., Heckman et al., 1981; Whittle, 1985; Xu et al., 1999; de Bruyn & Wilson, 1978). High resolution studies also show a good correlation between the radio and the emission line features (e.g., Capetti et al., 1996; Goodrich, 1992; Whittle et al., 1988). The radio jet axes of Seyferts were found to coincide with that of the ionization cones of the NLR (Wilson & Tsvetanov, 1994).

A good spatial overlap between the radio features and the optical emission line features was also noted in several Seyfert galaxies in a study by Falcke et al. (1998) using HST WFPC2 [O III] and H α +[N II] in conjunction with radio images using the historical VLA. Similarly, in radio galaxies, line emission extending up

1.8 AGN Jet Duty Cycle in Seyfert Galaxies

to several kpc was seen that appeared linked with the large scale radio emission (e.g., Baum & Heckman, 1989; Fosbury, 1986). Several other studies also showed that, in addition to the luminosities, the line-widths of the [O III] was correlated with the radio luminosities (e.g., Veilleux, 1991a,b). All these pieces of evidence were put together to suggest that the jets impart the momentum and the energy required for the ionization of, at least a part of the NLR via shock ionization (Dopita & Sutherland, 1996).

Three dimensional relativistic hydrodynamic simulations of low power jets show that while they are efficient accelerators of the ISM clouds, they dump a lot of energy into the ISM over a larger volume because these are trapped inside for a longer period compared to the powerful jets which plunge out of the ISM sooner (e.g., Mukherjee et al., 2016, 2018a,b).

1.8 AGN Jet Duty Cycle in Seyfert Galaxies

If indeed the radio emission on kpc scales is jet related and are the relics of past activity, the next step would be to estimate the duty cycle of jets in Seyfert galaxies. Several studies to understand the duty cycles of radio galaxies have been carried out in the recent past. Mahatma et al. (2018) find that the remnant population is smaller than 9%, whereas only $\sim 4\%$ of radio galaxies were double-double (Mahatma et al., 2019). Jurlin et al. (2020) found that a larger fraction ($\sim 13 - 15\%$) of sources showed evidence for restarted activity when they take compact flat spectrum sources in conjunction with relic like emission from the lobes.

It was found that the radio jets in Seyfert galaxies were often randomly aligned to the galaxy axes (e.g., Clarke et al., 1998; Nagar et al., 1999; Schmitt et al., 1997, 2001). Similar results were reproduced for a general sample of radio sources (Battye & Browne, 2009). Several multi-resolution studies also revealed that the pc scale jets were misaligned with the outer larger-scale structures on both 100 pc and kpc scales (e.g., Gallimore et al., 2006; Kharb et al., 2006; Middelberg et al., 2004). Such frequent misalignments are in contrast with the large scale radio galaxies, where we often find excellent agreement between several epochs of jet activity as seen in radio galaxies. Using estimates of lifetimes, Sanders (1984)

1. INTRODUCTION

argue that there might be several minor mergers that might be inducing the formation of a new accretion disk with every minor merger whose axis direction depends on the angular momentum of the infalling galaxy. Such a scenario can explain multiple episodes of short radio jets misaligned with each other.

The recent discovery of the changing look AGN phenomenon is possibly a result of the variable nature of the accretion activity in AGN (Elitzur et al., 2014; Schawinski et al., 2015). The transition between spectral states in X-ray observations along with vanishing broad lines and continuum variations on short time scales are the distinguishing features of these galaxies. Recently the changing-look behaviour was identified at radio wavelengths by Koay et al. (2016). If indeed changing-look AGN phenomenon is a result of varying activity of the nucleus, then it supports the picture of episodic activity on short time-scales.

1.9 Objectives of this thesis

In this thesis, we have attempted to understand the nature of outflows in Seyfert galaxies. The questions we have tried to address in this thesis include: are the radio outflows in Seyfert galaxies primarily AGN jet driven? Or do accretion disk driven winds contribute as well? Is there a significant contribution to the outflows from the starburst winds? We have used polarimetric observations to address these questions. We have also used a matched sample of starburst galaxies to compare and contrast the outflows in Seyferts versus star forming winds.

We have tried to address the question of whether we will find differences in KSRs that are AGN driven versus those that are starburst driven in terms of –

- (i) *The magnetic field structures:* The large scale magnetic fields in starburst galaxies are explained using the $\alpha - \Omega$ dynamo models (see Beck, 2015, and references therein). In many systems, X-shaped fields are observed, which are explained to be resulting due to the coupling of the wind field with the large scale galactic fields. Such fields could also be explained using magnetic dynamo also (see Woodfinden et al., 2019, for example). These large scale fields would, therefore, be oriented along the minor axis, whereas the KSR axis may be randomly oriented. Do the magnetic field structures in Seyfert outflows resemble those observed in RL AGN jets (fields are largely longitudinal and transverse

1.10 Outline of the thesis

to the local jet direction in FSRQs and BL Lacs, respectively) (e.g., Cawthorne et al., 1993; Gabuzda et al., 1992; Kharb et al., 2008)?

(ii) *The degree of polarization:* If the underlying mechanism of the production of these fields are different, one would expect a different fraction of ordered magnetic field component to that of the random fields, which would manifest as differences in the degree of polarization.

(iii) *The spatial scales of polarized emission regions:* For outflows with a jet origin, we would expect collimated structures, whereas, in starburst outflows, we would expect more diffuse and symmetric polarized structures.

(iv) *Large scale RM patterns:* RM inversion was observed from the outflows in NGC 253 which is an archetypal starburst galaxy. Heesen et al. (2011) model the walls of the outflow cones of the galaxy to be threaded by helical magnetic fields. Would we find RM gradients and will there be systematic differences in these RM images in our sample? With the broad bandwidths provided by VLA, it is possible to calculate in-band RM measures with single band observations.

1.10 Outline of the thesis

In the second chapter, we introduce the basic concepts of the interferometric implementation of radio polarimetry, polarization calibration, and the general causes of radio depolarization as well as RM synthesis to deal with it. We also explain the details of an end-to-end pipeline written to automate the analysis of polarization-sensitive data from the upgraded GMRT (uGMRT). In the third chapter, we present an in-depth study of one of the Seyfert galaxies in our sample, which also hosts a starburst nucleus. We then elucidate the details of the entire sample, observations, and results in the fourth chapter. In the fifth chapter, we briefly discuss the evidence for episodic jet activity in Seyfert galaxies. Finally, we summarize the main results of this work and discuss the intended future work in Chapter 6.

1. INTRODUCTION

2

Radio Interferometry and Polarimetry Techniques

In this chapter, I will introduce the basic concepts of radio interferometry and polarimetry, steps involved in the reduction of polarization-sensitive interferometric data, effects that lead to depolarization of astrophysical signals, and a brief discussion about a fully automated pipeline for analyzing uGMRT data.

2.1 Radio Interferometry

The radio interferometric technique makes use of an array of antennas, to obtain an image which has an angular resolution equivalent to that possible with a single antenna with an aperture as big as the largest separation between two antennas in the array. Van-Zittert Zernicke theorem provides the basis of radio interferometry. According to Van-Zittert Zernicke theorem,

$$V_\nu(u, v) = \int_{-\infty}^{\infty} \int_{-\infty}^{\infty} I_\nu(l, m) e^{-i2\pi(ul+vm)} dl dm \quad (2.1)$$

where $V_\nu(u, v)$ is known as the *spatial coherence function* and $I_\nu(l, m)$ represents the intensity distribution of the source, (l, m) represents the direction cosines on the plane of the sky w.r.t the phase center of the observations, (u, v) plane represents the coordinates in the Fourier plane for the given baseline (see Thompson et al., 2017, for a detailed treatment). It is evident from the above equation that

2. RADIO INTERFEROMETRY AND POLARIMETRY TECHNIQUES

the source intensity distribution is the inverse Fourier transform of the *spatial coherence function*. Each two-element interferometer measures a discrete value of the *spatial coherence function* at the corresponding (u, v) coordinates corresponding to the projected baseline length between the two antennas. The rotation of the earth will lead to a change in the projected baseline length. Observations taken over long periods can hence result in an adequately filled uv plane. Also, the dependence of (u, v) on the frequency of observation helps in filling up the plane with wide bandwidth observations.

However, due to the finite sizes of the radio dishes and inter-antenna spacings, one can never obtain a filled (u, v) plane. Hence a simple inverse Fourier transform of the real-life observations will provide the intensity distribution, $I_\nu^D(l, m)$.

$$I_\nu^D(l, m) = \int_{-\infty}^{\infty} \int_{-\infty}^{\infty} S(u, v) V_\nu(u, v) e^{i2\pi(ul+vm)} du dv \quad (2.2)$$

To account for the incomplete sampling, the $V_\nu(u, v)$ in Equation 2.3 is multiplied by a sampling function, $S(u, v)$ such that $S(u, v)=0$ at locations without any data. The dirty image, $I_\nu^D(l, m)$ is related to the real image, $I_\nu(l, m)$ by a two-dimensional convolution with $b_0(l, m)$, also known as the dirty beam.

$$I_\nu^D(l, m) = I_\nu(l, m) * b_0(l, m) \quad (2.3)$$

Here, the dirty beam, $b_0(l, m)$ is the Fourier transform of the sampling function, $S(u, v)$. In the following subsections, I briefly discuss the data reduction steps followed to obtain the total intensity continuum images from the visibility data.

2.1.1 Basic calibration

The electric signals from astrophysical objects that are finally measured at the telescope undergo a variety of effects including those of ionospheric, atmospheric, and instrumental origin. To retrieve the original signal strength we need to carry out time-based and frequency-based gain calibration for every antenna. The following equation gives the relation between the observed visibility, $V_{ij,obs}$ and the true visibility, $V_{ij,true}$.

$$V_{ij,obs} = G_i G_j^* V_{ij,true} + \epsilon_{ij} \quad (2.4)$$

where, G_i , G_j are the complex gains of antennas, i and j respectively and $\epsilon_{i,j}$ is the system noise.

The gain amplitude does not usually change very frequently with time, whereas the phase of the gain changes rapidly. Hence, to carry out the flux calibration, a source with known structure (often a point source), position, and flux density is observed along with the target source once or twice during the observation run. On the other hand, to correct for the phase gain, a suitable phase calibrator which is nearby the target source is observed both before and after the target source scan.

2.1.2 Deconvolution

Once the basic calibration is undertaken, we need to correct for the effect of the dirty beam, to obtain an image closest to the one that could have been obtained using a filled aperture telescope or the one with a Gaussian beam. There are several algorithms to undertake this ‘deconvolution’, e.g., ‘CLEAN’, ‘minimum entropy method’ (MEM), etc. The more widely used ‘CLEAN’ algorithm is available in task ‘IMAGR’ in AIPS and ‘tclean’ in CASA.

Schwarz (1978) shows that the method ‘CLEAN’ is mathematically equivalent to the ‘least square fitting algorithm’. It essentially models the source intensity distribution as a superposition of many point sources at various locations. The brightest point source is identified and is added to the ‘model image’ at the location of the source and the product of the point source peak and the dirty beam is subtracted from the ‘residual image’. Once the brightest source and the sidelobes associated with it are removed from the residual image, the weaker sources start showing up. The same step of identifying the next brightest source from the residual image and adding it to the model image is repeated until the residual image is noise-like. As the final step, the model image, which contains all the ‘CLEAN’ components is convolved with an elliptical Gaussian beam also known as the *synthesized beam* which is estimated by fitting the main lobe of the *dirty beam*.

There are several variants to this algorithm including ‘Hogbom’, ‘Clark’, ‘Cotton-Schwab’ algorithms.

2. RADIO INTERFEROMETRY AND POLARIMETRY TECHNIQUES

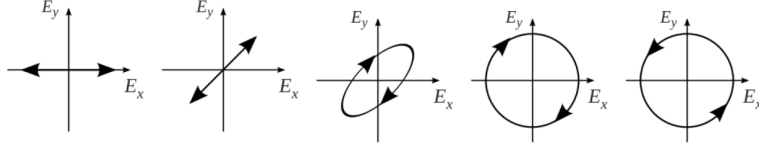


Figure 2.1: Polarization State of linear, circular and elliptical polarization

2.2 Radio Polarimetry

In this section, I will discuss the basic concepts of polarimetry and the interferometric formulation, and the various polarization calibration steps involved.

Maxwell's equations predict that light is comprised of transverse electric and magnetic fields perpendicular to each other and the direction of propagation. At optical frequencies, a polarizer selectively blocks the components of light whose electric field is aligned in the direction of its absorption axis and gives rise to linearly polarized light. Circularly polarized light is produced by passing the linearly polarized light through a quarter-wave plate which introduces a phase difference of $\pi/2$ between the two orthogonal components of the linearly polarized light. The polarization state (the trajectory traced by the tip of the electric field vector) of linear, circular, and elliptical polarization is shown in Figure 2.1.

Two vector conventions viz., Jones and Stokes vectors, were introduced to represent the polarization of light. Jones vector is comprised of two complex elements, namely the phase and amplitude of the orthogonal components. Stokes vectors, on the other hand, comprise of four real elements. As opposed to the Jones vector, the Stokes vector deals with the intensities, rather than the complex values of electric fields. The time-averaging that is intrinsic to the estimation of intensities, gives us the extra information about the amount of random electric fields or in other words the fraction of unpolarized light. The Stokes vectors are essentially defined as

$$I = \langle E_x^2 \rangle + \langle E_y^2 \rangle \quad (2.5)$$

$$Q = \langle E_x^2 \rangle - \langle E_y^2 \rangle \quad (2.6)$$

$$U = \langle E_a^2 \rangle - \langle E_b^2 \rangle \quad (2.7)$$

$$V = \langle E_r^2 \rangle - \langle E_l^2 \rangle \quad (2.8)$$

The Stokes I vector represents the total intensity. The other Stokes vectors namely, Q, U, and V are defined in such a way that the fractional polarized intensity, m is given by

$$m = \frac{\sqrt{Q^2 + U^2 + V^2}}{I} \quad (2.9)$$

The polarization angle, χ , also known as the EVPA, is given by

$$\chi = \frac{1}{2} \tan^{-1} \left(\frac{U}{Q} \right) \quad (2.10)$$

2.2.1 Formulation of the radio interferometric polarimetry

The feeds of radio antennas are usually sensitive to a single polarized component of the astrophysical signal. To deal with the polarization of the interferometric radio data, the coherency vector is used. This vector is used because the output of the correlators of the radio interferometer can be Fourier transformed and deconvolved using conventional tasks like ‘IMAGR’ and ‘tclean’ in AIPS and CASA respectively to directly obtain the components of the coherency vector.

The coherency vector, e is defined as

$$e = \begin{bmatrix} < E_{Ax} E_{Bx}^* > \\ < E_{Ax} E_{By}^* > \\ < E_{Ay} E_{Bx}^* > \\ < E_{Ay} E_{By}^* > \end{bmatrix} \quad (2.11)$$

The coherency vector can be defined differently for the circular feeds, by replacing the basis vectors, E_{Ax} by E_{Ar} and E_{Ay} by E_{Al} .

Usually, the coherency vector is transformed into the Stokes vector after which the equations 2.9 and 2.10 are used to obtain the fractional polarization and the polarization angle. While estimating the polarization intensity images, there is the additional requirement to correct for the Ricean bias. This bias is introduced as a result of adding Stokes ‘Q’ and ‘U’ images in quadrature. Both these images have a Gaussian distribution in noise and the resulting fractional polarization has a Rice distribution. This bias can be especially prominent for sources with weaker polarization signal.

2. RADIO INTERFEROMETRY AND POLARIMETRY TECHNIQUES

The transformation matrix, S which transforms the Stokes vector to the coherency vector for circular feed would be given by

$$S = \begin{bmatrix} 1 & 0 & 0 & 1 \\ 1 & 0 & 0 & -1 \\ 0 & 1 & i & 0 \\ 0 & 1 & -i & 0 \end{bmatrix} \quad (2.12)$$

Figure 2.2 shows the schematic of the pathway of the electric signal from the source and the various effects that are encountered en-route before conversion into voltages.

The electric signals from the source pass through the Earth's ionosphere which introduces some rotation to the polarized signal as a result of the Faraday effect. This Faraday rotation is denoted by F , a rotation matrix. For an alt-az mount, the feed keeps rotating with respect to the source over time. This parallactic angle rotation is accounted for by using the rotation matrix, P .

The feeds are not usually perfect transmitters of linearly or circularly polarized signals. Hence the polarized intensity as detected by a feed may also include some amount of "leakage" from the orthogonal component. The fraction of the leakage is often symbolized as D-terms in the equation relating the complex antenna gains, the input and output voltages.

The signal detected at both the feeds then passes through their respective electronic backends. The gains that are introduced are represented by the G matrix.

Hence all these effects can be mathematically summarized using the following equation.

$$e_{out} = GDCPF e_{in} = J e_{in} \quad (2.13)$$

where e_{out} is the output Jones vector, e_{in} is the input Jones vector, and J is the Jones matrix.

2.2.2 Polarization Calibration

In addition to basic gain calibration steps, several effects like the ellipticity of the feeds, non-orthogonality of feeds, and the offset of the polarization angles

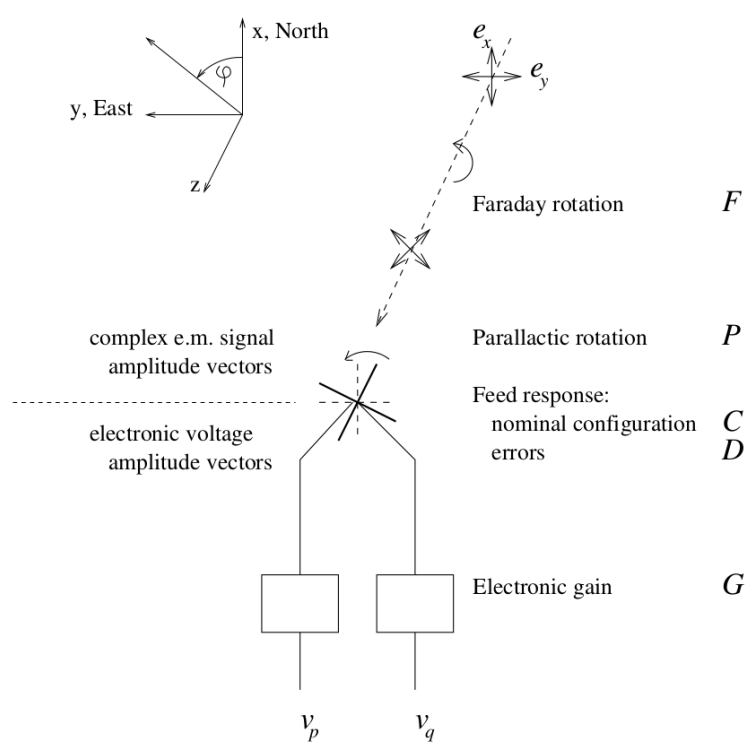


Figure 2.2: Illustration of various effects encountered along the path of the astrophysical signal. Taken from Hamaker et al. (1996)

2. RADIO INTERFEROMETRY AND POLARIMETRY TECHNIQUES

necessitate further calibration to correct for these errors.

2.2.2.1 Leakage Calibration

The polarized feeds that are mounted on radio telescopes are not perfect. They need not be perfectly aligned at orthogonal angles to each other nor do they transmit perfectly linear/circular polarized signals. The ellipticity of the feeds imply that some amount of the polarized signal from each of the feed leaks into the other feed. This will result in measuring polarization from an unpolarized source and is known as the instrumental polarization. In the simplest case, the measured voltages can be represented using the following equation.

$$\begin{bmatrix} v_L \\ v_R \end{bmatrix} = \begin{bmatrix} G_L & 0 \\ 0 & G_R \end{bmatrix} \begin{bmatrix} D_L & 1 \\ 1 & D_R \end{bmatrix} \begin{bmatrix} E_R \\ E_L \end{bmatrix} \quad (2.14)$$

where D-terms represent the leakage from one feed into the other, and the G-terms represent the complex amplitude terms estimated during the initial amplitude calibration. The leakage terms are typically very small in amplitude and are about the order of a few percent. As a result, the second and the higher-order terms in the cross-correlation terms are neglected while estimating the leakage terms.

There are two possible strategies to calibrate the D-terms either using an unpolarized calibrator or using multiple scans of a polarized calibrator. While using an unpolarized calibrator, the source polarization is set to zero and the residual polarization represents the instrumental polarization, which is used to calibrate the D-terms.

When a polarized calibrator is involved, several scans spanning a range of parallactic angles are required. In this case, the D-terms remain a constant over varying parallactic angles and the source polarization appears to rotate with time. A joint solution for the constant D-terms and the varying source polarization is determined in this case.

2.2.2.2 Polarization angle calibration

For the regular phase gain calibration, the gain phases of the reference antenna are set to zero and the gain phases of all the other antennas are estimated under

2.3 Depolarization

this assumption. The gain phases assigned to each antenna (denoted by n) for a given Stokes (S) is not the absolute phase gain, $\phi_{S,n}$, but the difference of phase gains between the given antenna and the reference antenna. Let the assigned phase gain of the antenna, n with Stokes, S be $\phi'_{S,n}$. Then the relation between the absolute and assigned phase gain is $\phi'_{S,n} = \phi_{S,n} - \phi_{S,ref}$, where $\phi_{S,ref}$ represents the absolute phase gain of the reference antenna. For RR^* and LL^* (R^* and L^* represent the complex conjugate vectors) correlations, the $\phi_{S,ref}$ term cancels out. But for RL^* and LR^* correlation, this does not happen. The phase correction for RL^* , $(\phi'_{R,n} - \phi'_{L,m}) = (\phi_{R,n} - \phi_{L,m}) - (\phi_{R,ref} - \phi_{L,ref})$, is loaded with an additional term, $\Delta\phi = (\phi_{R,ref} - \phi_{L,ref})$ which needs to be removed. Physically, this manifests as an offset in the polarization angle, $(-\frac{\Delta\phi}{2})$ for the sources.

For a circular basis, the rotation by an angle χ for the vectors is given by the following.

$$R' = e^{i\chi} R \quad (2.15)$$

$$L' = e^{-i\chi} L \quad (2.16)$$

Now, when $\chi = -\frac{\Delta\phi}{2}$,

$$R'L^* = e^{-i\Delta\phi} RL^* \quad (2.17)$$

$$L'R^* = e^{i\Delta\phi} LR^* \quad (2.18)$$

Hence, to correct for this phase offset, a known calibrator is observed to find the offset in PA of polarization, χ . The corresponding phase correction is then applied to RL^* and LR^* , by multiplication of $e^{-i2\chi}$ and $e^{i2\chi}$ respectively.

2.3 Depolarization

Synchrotron emission is intrinsically linearly polarized. For an optically thin plasma, the degree of polarization depends on the electron energy index as $\frac{3\gamma+3}{3\gamma+7}$ (Le Roux, 1961). However, in reality, we observe fractional polarization much lower than 75% which is the expected value for a typical plasma with $\gamma=2.5$. There are mainly two physical effects that play a role in depolarizing the medium and hence resulting in a lower fractional polarization (Burn, 1966).

2. RADIO INTERFEROMETRY AND POLARIMETRY TECHNIQUES

1. **Faraday effect:** When a linearly polarized light passes through a magneto-ionized medium, it undergoes rotation by a certain angle as a result of circular birefringence. It occurs because the left circularly polarized light and the right circularly polarized light travels at a different velocity through the medium. The final effect will be a rotation of the angle of the linearly polarized light.
2. **Random magnetic fields within the beam:** When the ordering scales of the magnetic fields are much smaller than the beam size, the vector averaging leads to detection of lower degree of polarization.

The depolarization that is seen in the radio emission is modeled as the combination of both the effects either introduced by the emitting medium itself or an external Faraday rotating medium (Sokoloff et al., 1998).

We now discuss various models of depolarization below.

1. **Depolarization due to random magnetic fields:** If the ordered magnetic field component is B_o and the random magnetic field component be represented by B_r , then the polarization fraction reduces by a factor, $\frac{B_o^2}{B_o^2 + B_r^2}$.
2. **Differential Faraday dispersion:** When we consider a uniform slab of an emitting region which is also the Faraday rotating medium, then the polarized emission from different lengths of the emitting region undergoes rotation by different amounts. As a result, the net emission received at the observer would in effect have undergone depolarization. The complex polarization emitted by a uniform slab of Faraday rotating synchrotron emitting material is given by, $\mathcal{P} = p_i \frac{\sin \mathcal{R}\lambda^2}{\mathcal{R}\lambda^2} \exp 2i(\psi_0 + \frac{1}{2}\mathcal{R}\lambda^2)$.
3. **External depolarization:** An external screen of magneto-ionized medium threaded by uniform magnetic fields only introduces a rotation of the linearly polarized angle. However, when the external magnetic field is not ordered and has a random component, there will be depolarization. This is because the RM is a function of magnetic field strength. In this case, the mean degree of polarization decreases as a function of the wavelength as $\mathcal{P} \propto \exp(-2\sigma_{RM}^2 \lambda^4)$.

4. **Internal depolarization:** Internal depolarization occurs when we combine the effects of random magnetic fields along with the differential Faraday dispersion. The mean polarization is given by $\langle \mathcal{P} \rangle = \langle \mathcal{P}_0 \rangle \frac{1 - \exp(-S)}{S}$, where $S = 2\sigma_{RM}^2 \lambda^4 - 2i\lambda^2 \mathcal{R}$.

2.4 Rotation Measure Synthesis

Since the angle of rotation is a function of the square of the wavelength, the polarized emission from different parts of the spectrum undergoes rotation by different amounts. Averaging the polarization signal from the entire band will result in bandwidth depolarization. The idea of rotation measure synthesis was introduced in Burn (1966) and was discussed in detail in Brentjens & de Bruyn (2005). The observed complex polarization can be expressed as a Fourier transform of the Faraday dispersion function $F(\phi)$ as follows.

$$P(\lambda^2) = \int_{-\infty}^{\infty} F(\phi) e^{2i\lambda^2\phi} d\phi \quad (2.19)$$

where ϕ is the Faraday depth. This equation can be inverse Fourier transformed to obtain the intrinsic polarization as a function of varying Faraday depths. However, the sampling in the frequency is limited by the bandwidth and frequency of observation as a result of which deconvolution is carried out.

2.5 uGMRT data reduction pipeline for polarization-sensitive data¹

The upgrading of the GMRT has resulted in a near-continuous frequency coverage from 150 MHz to 1400 MHz. The earlier maximum bandwidth of 32 MHz at any particular center frequency has now been upgraded to a maximum bandwidth of 400 MHz. In this section, we present an end to end pipeline for uGMRT continuum data analysis mostly AIPS

The pipeline is essentially a set of python codes that have to be run in CASA.

¹The codes can be found on GitHub. see here.

2. RADIO INTERFEROMETRY AND POLARIMETRY TECHNIQUES

The inputs to the codes are the name of the directory containing the lta or fits data files and the starting userid in **AIPS** in which the data is to be analyzed. If the data files are in lta format, they are first converted to fits files. The pipeline extracts the information about each data set like the observing frequency, flux, and phase calibrators, the number of channels to be averaged while imaging, etc. The code then writes run files that have all the commands that are to be executed in **AIPS**. Once these runfiles are created for all the data files in the input folder, the actual analysis of the data in **AIPS** is initiated by using the subprocess module of python.

The data analysis steps are the regularly followed procedures for GMRT continuum data reduction. After the initial editing and calibration of the data, the legacy GMRT Software Backend (GSB) data sets undergo several rounds of imaging and phase-only self-calibration before a final round of A&P self-calibration and imaging. The data analysis of legacy GMRT data is completely done in **AIPS**. However, for wideband data sets, after several rounds of phase-only self-calibration, the final imaging is carried out in **CASA** using the Multi-Scale Multi-Frequency Synthesis (MS-MFS) algorithm available in **CASA**.

The outputs can be found in the output folder, which is created with a name that has ‘out’ appended to the input folder name. The details about the observation, userid, channels averaged etc can be found here. The final image and uv files can be found in folders named ‘im’ and ‘uv’ respectively. The file ‘output.txt’ also records all output logs from the **AIPS** message window.

3

The Filamentary Radio Lobes of the Seyfert-Starburst Composite Galaxy NGC 3079¹

3.1 Introduction

Radio observations reveal that most Seyfert galaxies have sub-parsec-scale radio emission in spite of their “radio-quiet” AGN status (Kharb et al., 2010b, 2014b; Lal et al., 2004; Roy et al., 1994; Thean et al., 2000; Ulvestad & Wilson, 1984a,b; de Bruyn & Wilson, 1976). Many of these galaxies with small-scale radio emission show elongated KSRs, similar to the radio jets seen in powerful radio galaxies. The kpc-scale radio structures, however, are not always found to be aligned with the small scale jets (Baum et al., 1993; Colbert et al., 1996b; Gallimore et al., 2006). Furthermore, Seyfert radio jets were found to be randomly aligned with respect to the host galaxy major axes (Kinney et al., 2000; Schmitt & Kinney, 2002; Schmitt et al., 2001). Abrupt changes of jet axes were also inferred in several Seyfert galaxies, e.g., NGC 4151 (Ulvestad et al., 1998), NGC 1068 (Gallimore et al., 1996), and Mrk 6 (Kharb et al., 2006). It appears that the radio structures in Seyfert galaxies are more complex than in radio galaxies. In particular, it is unclear if KSRs are purely AGN-driven (either via a jet or an accretion-disk wind)

¹The contents of this chapter have been published in [Sebastian et al., ApJ, 2019, 883, 189](#), see here.

3. THE FILAMENTARY RADIO LOBES OF THE SEYFERT-STARBURST COMPOSITE GALAXY NGC 3079

or starburst superwind-driven. It is essential to disentangle these contributions before the truly relevant questions of how radio outflows are produced in low luminosity AGN (LLAGN), in general, and Seyfert galaxies in particular can be answered. Also, the role played by LLAGN outflows in AGN feedback needs to be examined (Croton et al., 2006; Müller-Sánchez et al., 2011; Riffel et al., 2013).

NGC 3079 is a well known nearby ($z = 0.003723$) Seyfert 2 / LINER galaxy with a nuclear starburst, that is a member of an interacting galaxy pair. It is an edge-on spiral galaxy with several regions of star-formation along the disk. Its 8-shaped radio structure with a ring-like feature (“ring” hereafter) inside its north-east lobe (Duric & Seaquist, 1988; Irwin & Saikia, 2003), its slow-moving ($v \sim 0.1c$) parsec-scale radio jet (Baan & Irwin, 1995; Irwin & Seaquist, 1988; Middelberg et al., 2005a), copious amount of hot X-ray gas and emission-line filaments (Cecil et al., 2001, 2002), have been well documented. NGC 3079 is a Compton-thick AGN (Iyomoto et al., 2001) having a disk-like pseudo-bulge. The origin of the double-lobed morphology observed in the NGC 3079 is not yet completely understood. Duric & Seaquist (1988) argue that the lobe material is moving at supersonic velocities, though they dismiss the possibility that these are jets which may be precessing based on the difficulty in reproducing the closed loop morphology using these models. They suggest that these are probably winds originating from a nuclear starburst or accretion activity. X-ray emission and emission line imaging shows that NGC 3079 hosts a superwind (Cecil et al., 2001, 2002; Veilleux et al., 1994). Superwinds are believed to be generated when the kinetic energy from supernovae and massive star winds are transformed into thermal energy. The heated gas then expands into the lower pressure ambient medium. The direction of the steepest pressure gradient is along the minor axis. The hot gas is easily traced by the X-ray emission, which is a more direct tracer compared to the emission line gas, which is generated at shock fronts as a result of the interaction with the ambient medium. The emission line ratios seen in superwinds are typical of shock-ionized gas as also seen in the case of NGC 3079 (Veilleux et al., 1994). Although these authors favored a starburst-wind origin for the radio lobes, they were not able to rule out AGN-driven winds. Several authors favored the jet origin of the lobes (Irwin & Saikia, 2003; Irwin & Seaquist, 1988) partly because of the known VLBI structure.

3.2 Observations and Data Analysis

Lin et al. (2016); Miyamoto et al. (2015); Sofue et al. (2001) have studied the molecular constitution and kinematics of NGC 3079 using various molecular lines in both emission and absorption. Many of these studies present evidence for blue-shifted features or blue-wings which was readily associated with outflowing molecular gas. Shafi et al. (2015) present evidence for outflowing HI gas. These authors propose that large amounts of cold gas, both molecular and atomic, is being blown out along with the ionized gas. They find that both the AGN and starburst scenarios are powerful enough to drive such outflows. They also point out that such multi-phase gas outflows are being discovered in several AGN driven outflows. The presence of a nuclear starburst in NGC 3079 was contested by Hawarden et al. (1995). They suggest that the molecular gas outflows are driven by the AGN rather than a starburst.

Despite the abundance of literature on NGC 3079, a consensus has not yet been reached regarding the origin of the kpc sized radio emission. In this chapter, we present a polarization-sensitive radio study of NGC 3079 with the historical and expanded VLA, at multiple radio frequencies and array configurations. We attempt to disentangle the contribution of the starburst, AGN winds and the jet in the formation of double-lobed structure in NGC 3079.

3.2 Observations and Data Analysis

3.2.1 VLA Data from 1995

We observed NGC 3079 with the historical VLA at 1.5 and 4.9 GHz with the A, B and C-array configurations in 1995–1996 (Project ID: AB740). 3C 286 and 3C 48 were used as the primary flux density as well as the polarization calibrators, while 1035+564 was used as the phase calibrator for the whole experiment. The data were processed with AIPS using standard imaging and self-calibration procedures. Table 3.1 lists the observing frequency, the corresponding bandwidth, the VLA configuration, the observation date, the FWHMs of the synthesized beams, the total flux densities of the source at the corresponding resolution and the *rms* noise of the final images. AIPS task PCAL was used to solve for the antenna “leakage” terms (D-terms) as well as polarization of the calibrators 3C 286 and

3. THE FILAMENTARY RADIO LOBES OF THE SEYFERT-STARBURST COMPOSITE GALAXY NGC 3079

3C 48. The leakages were typically a few percent. Polarization calibration of the 4.9 GHz A-array data was unsuccessful. This was a consequence of not having acquired enough scans of the polarization calibrator for adequate parallactic angle coverage; there were only two scans of 3C 286.

The polarization intensity (PPOL) and polarization angle (PANG) images were created by first running the task IMAGR for Stokes ‘Q’ and ‘U’ and then combining these images using the task COMB. Pixels with intensity values below 3σ and angle errors $> 10^\circ$ were blanked before making PPOL and PANG images, respectively. Fractional polarization images were created using the PPOL and total intensity images where pixels with $> 10\%$ errors were blanked. We created two-frequency spectral index images using the AIPS task COMB after first convolving images at both frequencies with the same circular beam ($= 1.45'' \times 1.45''$). Pixels with total intensity value below 3σ were blanked before making the spectral index image. Rotation measure images were created using three frequencies using AIPS tasks MCUBE, TRANS, and RM. For this, we split the two IF data at L-band (IF1 = 1.465 GHz, IF2 = 1.385 GHz) and used the C-band (frequency = 4.860 GHz) data as such. Images were made after first convolving all images with the same circular beam ($= 1.45'' \times 1.45''$). Pixels with errors $> 13^\circ$ were blanked while making the polarization angle images (PANG) shown in Figure 3.3. We created depolarization (DP) images by dividing the fractional polarization images at 1.42 GHz and 4.86 GHz using the task ‘COMB’. We blanked pixels with fractional errors $> 20^\circ$ before making the DP image shown in Figure 3.7.

3.2.2 VLA Data from 2018

New polarization-sensitive VLA data at 5 GHz were acquired in 2018 (project ID: 17B_074; see Table 3.1) using the BnA array configuration. 3C286 and 1035+564 were observed as the primary flux + polarization calibrator and phase calibrator respectively. OQ208, which is a strong unpolarized source was observed to calibrate the polarization leakages. Data were reduced using CASA version 5.1.2-4. Basic calibration and editing of the data were carried out using the CASA pipeline for VLA data reduction. Polarization calibration was performed on the

3.2 Observations and Data Analysis

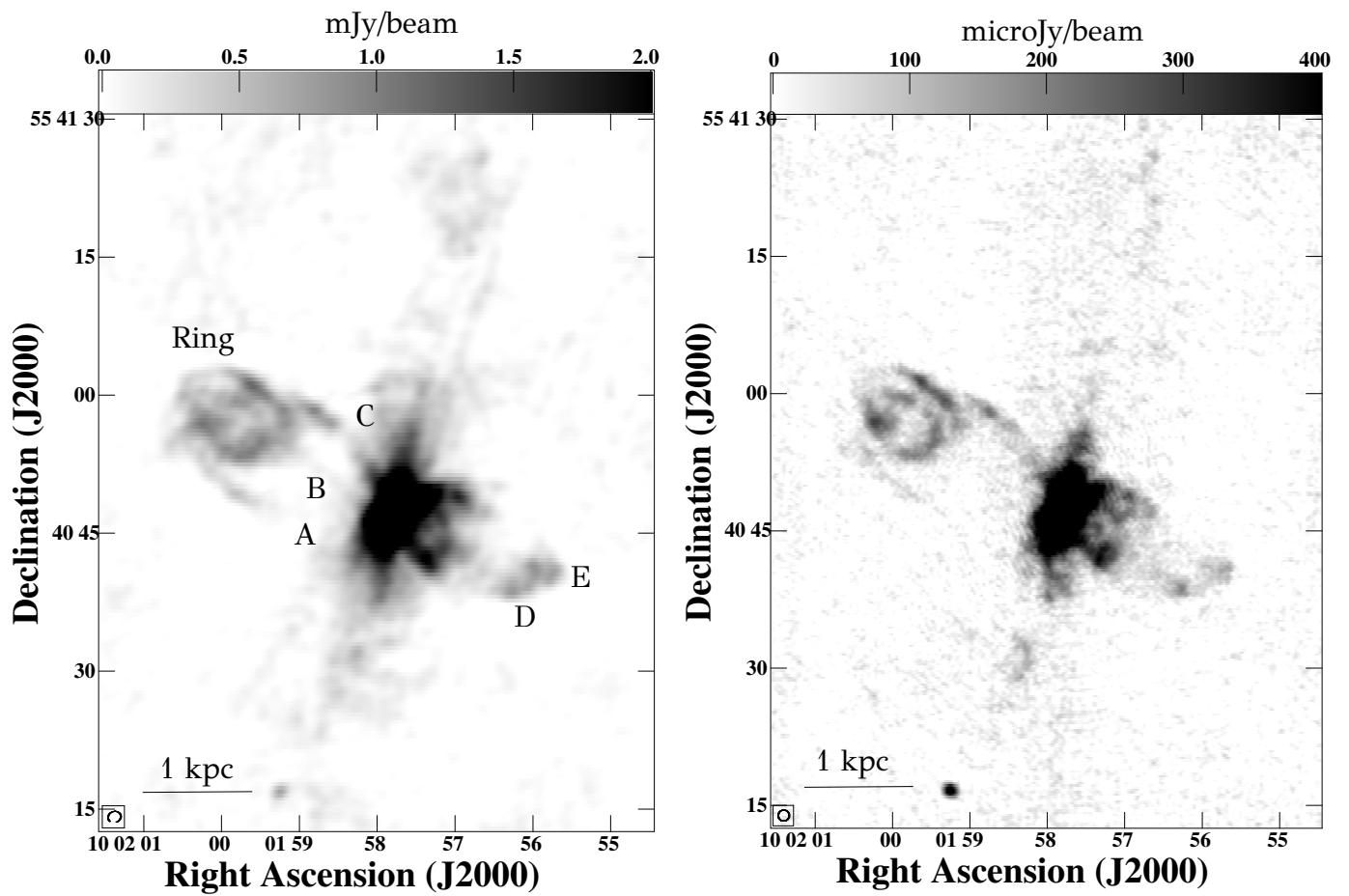


Figure 3.1: Grey scale images of total intensity showing the filamentary radio structures observed in NGC 3079 with the (left) historical VLA A-array at 1.4 GHz with a beam size $1.45'' \times 1.19''$ and P.A., -80.2° and (right) historical VLA B-array at 5 GHz with a beam size, $0.58'' \times 0.43''$ and P.A., 85.8° .

3. THE FILAMENTARY RADIO LOBES OF THE SEYFERT-STARBURST COMPOSITE GALAXY NGC 3079

pre-calibrated data. The model of 3C 286 was defined using the model parameters which were fed manually to the task ‘setjy’. The model parameters required for completely defining the source model included the stokes I flux density at the reference frequency, the spectral index, the coefficients of the Taylor expansion of both the degree of linear polarization as a function of the frequency about the reference frequency and the reference frequency itself. The polarization angle of 3C 286 appears to be a constant across frequencies whereas the degree of polarization varies across frequencies. Therefore we estimated the coefficients by fitting a first-order polynomial using the data from Perley & Butler (2013). The cross-hand delays between both the polarizations were corrected. The leakage terms per channel were solved using the **CASA** task ‘polcal’ with the unpolarized source OQ208. The polarization angle was calibrated using the known polarization angle of 3C286.

The target NGC 3079 was then SPLIT out before imaging. We made use of the MT-MFS algorithm in **CASA** while cleaning to take care of the wideband effects. Imaging and phase-only self-calibration were performed iteratively for three times before a final round of A&P self-calibration and imaging was performed. The stokes ‘Q’ and ‘U’ images were made using the final calibrated uv data file. The VLA data had 16 spectral windows spanning a bandwidth of 2 GHz. The data set was then divided into four chunks each consisting of 4 spectral windows. The ‘QU’ stokes image cubes of these data sets were then created using task ‘tclean’ in **CASA**. Finally, the task ‘rmfit’ was used to make an in-band rotation measure image from these cube images. We have not corrected for Ricean-bias because the polarized emission had sufficiently high enough SNR to be affected by Ricean bias. The RM image obtained is shown in 3.6. The pixels where the errors are greater than 200 rad m^{-2} were blanked. The RM image is shown in the left panel of figure 3.6.

3.3 Radio Morphology: Lobes, Ring, Galaxy

The total intensity and linearly polarized emission images for NGC 3079 are presented in Figures 3.1 to 3.3. The 1.4 GHz image in Figure 3.1 (right panel) shows the north-eastern lobe with an extent of $27'' (=2.3 \text{ kpc})$ and the south-western

3.3 Radio Morphology: Lobes, Ring, Galaxy

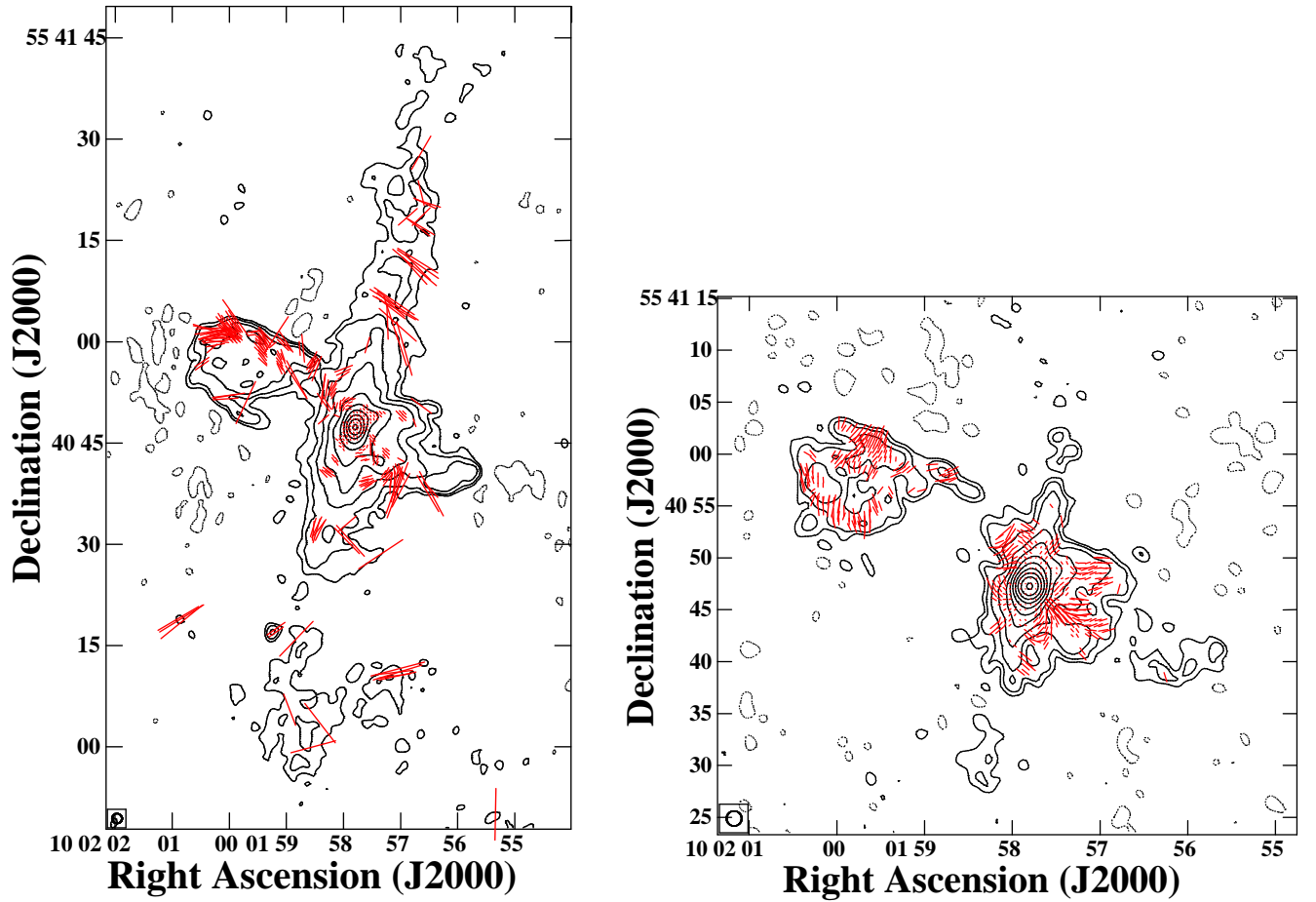


Figure 3.2: (Left) 1.4 GHz historical VLA A-array image with contour levels $0.850 \times (-0.170, 0.170, 0.350, 0.700, 1.400, 2.800, 5.600, 11.25, 22.50, 45, 90)$ mJy beam $^{-1}$ and (right) 5 GHz historical VLA B-array image with contour levels $0.800 \times (-0.085, 0.085, 0.170, 0.350, 0.700, 1.400, 2.800, 5.600, 11.25, 22.50, 45, 90)$ mJy beam $^{-1}$ of NGC 3079 with electric vectors whose length is proportional to the fractional polarization superimposed in red.

3. THE FILAMENTARY RADIO LOBES OF THE SEYFERT-STARBURST COMPOSITE GALAXY NGC 3079

Table 3.1: Observation log and observed parameters of NGC 3079.

Frequency (GHz)	Bandwidth (MHz)	VLA Array Configuration	Observation Date	Beam, PA (arcsec ² , °)	Total Flux Density (mJy)	r.m.s. (μJy beam ⁻¹)
4.86	50	A	07/21/1995	0.45×0.31, 81.1	99.4	27
4.86	50	B	11/02/1995	0.58×0.43, 85.8	161.0	16
1.42	50	A	07/03/1995	1.45×1.19, -80.2	509.0	53
1.42	50	C	02/17/1996	14.82×13.03, 62.2	838.0	80
5.50	2048	BnA	02/16/2018	1.10×0.47, -87.08	260.3	8.6

lobe with an extent of 20'' (=1.7 kpc) in exquisite detail, especially the extremely filamentary nature of the lobes. The north-eastern lobes show three distinct filaments annotated as A, B and C two of them forming the “edges” of the radio bubble/lobe. The filament at the southern edge (A) can extend up to the top edge of the lobe. This filament shows increased brightness towards the top edge of the lobe. The northern filament (C) can also be traced till the lower end of the “ring-like” structure after which the trajectory is not clear. This filament also appears brighter, farther away from the core. It is probable that the “ring” is a 3D-shell-like structure seen in projection. The “ring-like” feature at the top of the north-eastern lobe appears to be comprised of additional radio filaments. They are the brightest filaments and do not appear to be connected to the center of the galaxy.

The south-western lobe, on the contrary, does not comprise of as many filamentary structures. Yet, the edges of the lobe, especially at the base, appear brighter compared to the emission from the inner parts. Further away, towards the southernmost tip, there is an increase in brightness where it appears as though two filaments, namely E and D, have turned in. Unlike the north-eastern lobes, there are no standalone filamentary structures apparently disconnected from the core.

3.3 Radio Morphology: Lobes, Ring, Galaxy

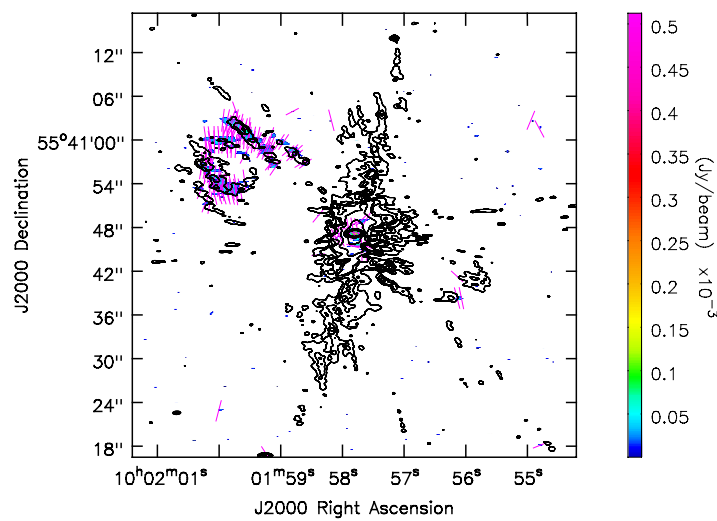


Figure 3.3: New VLA 5 GHz image of NGC3079 with total intensity in contours and polarized intensity in colour. The polarization electric vectors are shown in magenta. Contour levels represent $25.5 \times (2, 4, 6, 8, 16, 64, 256, 512, 1024)$ $\mu\text{Jy beam}^{-1}$. The beam shown in the bottom left corner as a filled ellipse is of size $1.10'' \times 0.47''$ and P.A. is -87° .

3. THE FILAMENTARY RADIO LOBES OF THE SEYFERT-STARBURST COMPOSITE GALAXY NGC 3079

3.3.1 Host Galaxy Emission

Figure 3.4 shows a higher resolution image (VLA A-array 5 GHz) and a lower resolution image (VLA C array 1.4 GHz). The lower resolution image reveals the large extent of host galaxy radio emission. The lobes are seen embedded slightly above the disk in the low-resolution view. Apart from the lobes, there are several features which protrude out of the disk. A prominent spur-like feature is seen rising up to ~ 8 kpc above the disk at nearly 4 kpc in the north-east direction along the disk from the center. It is also interesting to note that most of these protrusions are highly polarized. Such spurs were previously seen in other starbursts systems hosting a radio halo like NGC 253 (Carilli et al., 1992). They suggest that the material from the disk gets convected up and is driven by both cosmic ray pressure as well as thermal pressure. The protrusion can also be explained as galactic fountains (Bregman, 1980; Shapiro et al., 1976). Another possibility is that the spur is merely a part of a large loop seen by Irwin & Saikia (2003) in their lower resolution images (Figure 2). The higher resolution image does not show any lobe emission whereas the emission from the disk which is aligned very well with the outer disk is very prominent.

3.3.2 Spectral and Polarization properties

The 1.4 GHz - 5 GHz spectral index image of NGC 3079 is shown in Figure 3.5. The spectrum is mostly steep (mean $\alpha \sim -1.2 \pm 0.13$) except at the core. The spectral index image shows that the inner parts of the disk have a flatter spectrum compared to the rest of the source. The core possesses a flat spectrum ($\alpha \sim -0.3 \pm 0.002$) pointing towards current AGN activity as is substantiated by the presence of a relativistically moving VLBI jet (Irwin & Seaquist, 1988; Middelberg et al., 2007; Sawada-Satoh et al., 2000; Trotter et al., 1998). The spectral index image also reveals regions of flat spectrum along the edges of the ring. The spectral index becomes as flat as -0.5 in certain locations along the edges.

The fractional polarization ($FP = P/I$) images reveal the “ring” to have $FP = 16 \pm 5\%$ at L-band and $FP = 33 \pm 9\%$ at C-band. For the central part of the galaxy showing polarization, we find $FP = 4 \pm 1\%$ at L-band and $FP = 16 \pm 3\%$ at C-band. For the L-band C-array image with a resolution of

3.3 Radio Morphology: Lobes, Ring, Galaxy

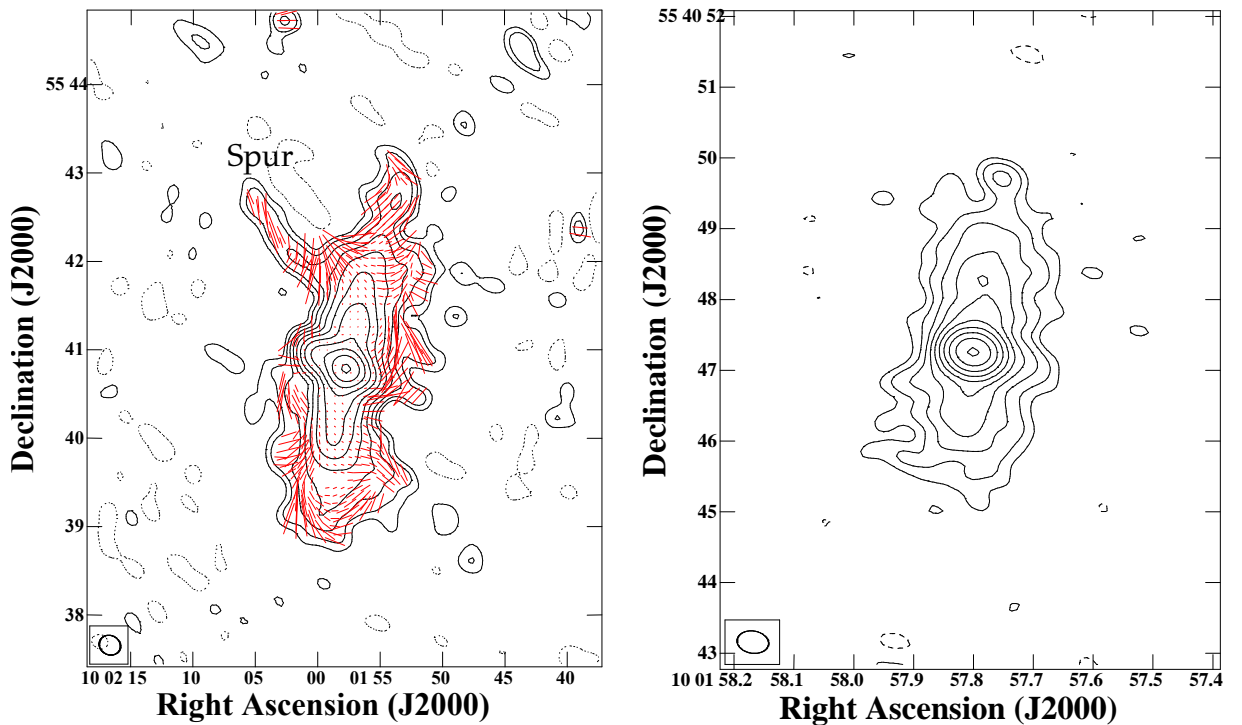


Figure 3.4: (Left) 1.4 GHz historical VLA C-array image of NGC 3079 with contour levels = $3.0 \times (-0.085, 0.085, 0.170, 0.350, 0.700, 1.400, 2.800, 5.600, 11.25, 22.50, 45, 90)$ mJy beam $^{-1}$ and (right) 5 GHz historical VLA A-array image with contour levels = $0.61 \times (-0.085, 0.085, 0.170, 0.350, 0.700, 1.400, 2.800, 5.600, 11.25, 22.50, 45, 90)$ mJy beam $^{-1}$. The electric vectors with length proportional to fractional polarization are superimposed in red.

3. THE FILAMENTARY RADIO LOBES OF THE SEYFERT-STARBURST COMPOSITE GALAXY NGC 3079

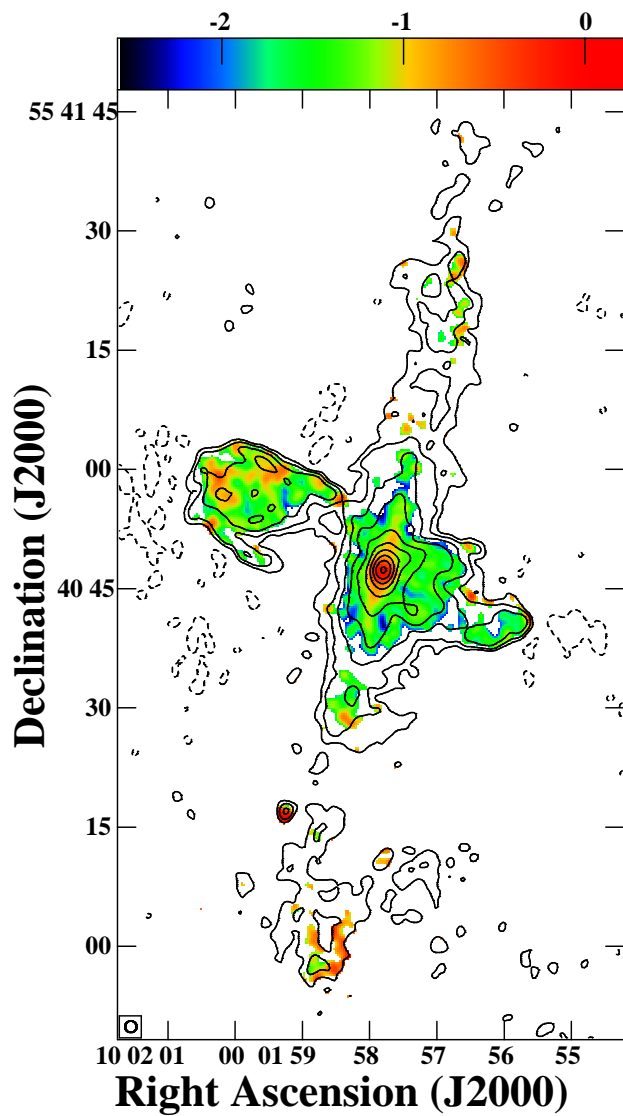


Figure 3.5: The 1.4 - 5 GHz historical VLA spectral index image of NGC 3079 in color superimposed by the 1.4 GHz radio contours. The circular beam shown in the left corner is of size $1.45'' \times 1.45''$.

3.4 Energetics of Radio lobes

$\sim 14''$ where the KSR is not clearly resolved (Figure 3.4), we find that the average fractional polarization is $FP = 19 \pm 3\%$. Interestingly, the “spur” like feature to the north-east of the host galaxy disk is very highly polarized: $FP = 40 \pm 7\%$. Images made with fractional polarization pixels blanked for errors greater than 20% suggest that at L-band, the “ring” and the galaxy have $FP = 14 \pm 4\%$ and $FP = 4 \pm 1\%$, respectively, and at C-band, the “ring” and the galaxy have $FP = 40 \pm 12\%$ and $FP = 24 \pm 7\%$, respectively.

The new VLA image at 5 GHz mostly detects the ring-like feature (Figure 3.3); the fractional polarization is $37 \pm 8\%$ in the “ring” and $6 \pm 2\%$ in the galaxy. It is clear that the new VLA image is not as sensitive as our deeper historical VLA images. However, the filaments comprising the “ring” are more clearly delineated in the new image in polarized light. Our in-band RM image indicates that the average RM values are in the range of $\pm 50 - 100 \text{ rad m}^{-2}$, similar to what was previously observed in the “ring” by (Cecil et al., 2001).

The three-frequency RM image (see figure 3.6 left panel) reveals an $\text{RM} = +150 \text{ rad m}^{-2}$ with an error of 30 rad m^{-2} , for the southern part of the host galaxy emission. For the western jet region, $\text{RM} = -210 \text{ rad m}^{-2}$ with an error of 15 rad m^{-2} . We have also estimated the depolarization parameter, DP, as $\text{DP} = m_l/m_h$, where m_l and m_h are the fractional polarization at low and high frequencies, respectively. The DP image is shown in Figure 3.7. A higher value of DP implies lower depolarization. We find that the average $\text{DP} = 0.3$ in the “ring”, and 0.4 in the galaxy; the average DP approaches 0.8 in the central regions of the galaxy. The higher depolarization around the ring could be suggestive of greater confinement.

3.4 Energetics of Radio lobes

NGC 3079 has a flared and clumpy accretion disk (Hu, 2008) with detections of water maser emission on milliarcsec scales (Kondratko et al., 2000). Kondratko et al. (2000) have estimated a black hole mass of $2 \times 10^6 M_\odot$ in NGC 3079 using a VLBA study of water masers within a radius of 0.4 pc. Iyomoto et al. (2001) find that X-ray emission is heavily obscured and the luminosity after correction for absorption turns out to $10^{42} - 10^{43} \text{ ergs s}^{-1}$. This luminosity would imply that

3. THE FILAMENTARY RADIO LOBES OF THE SEYFERT-STARBURST COMPOSITE GALAXY NGC 3079

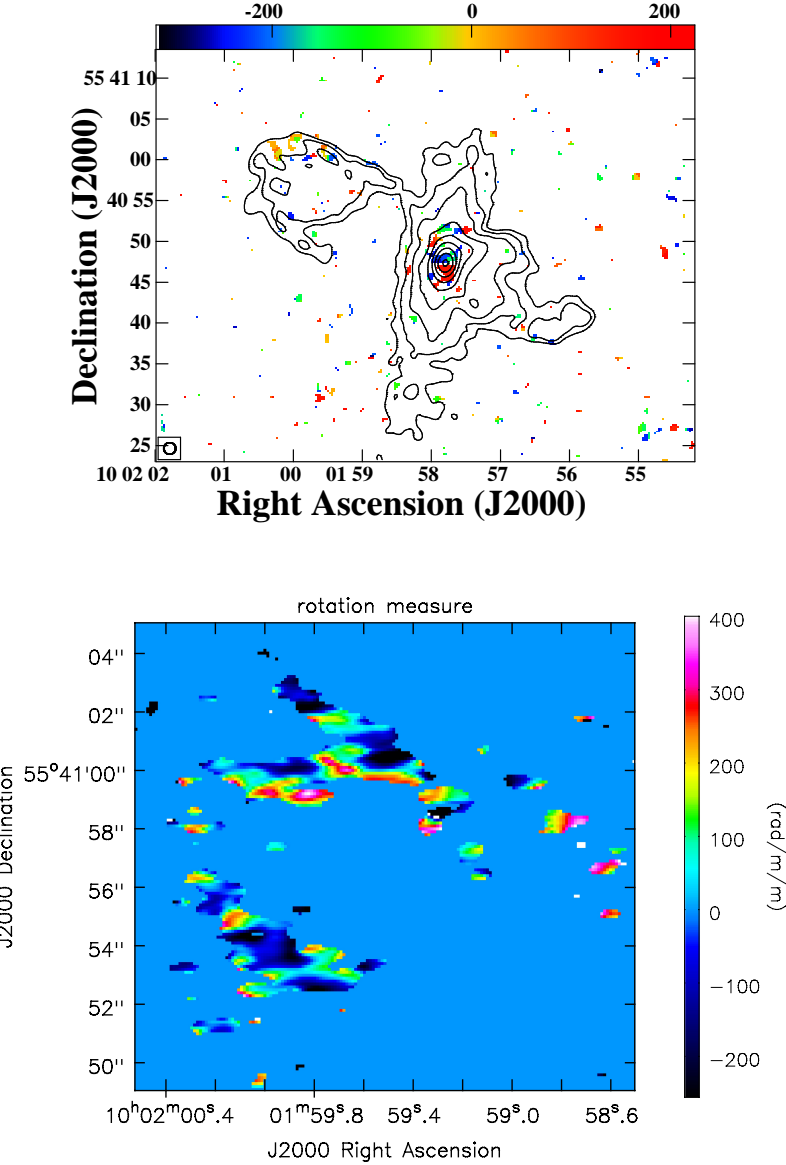


Figure 3.6: (Top) The three frequency historical VLA rotation measure image in color superimposed by the 1.4 GHz radio contours and (bottom) the color in-band VLA rotation measure image of the north-eastern lobe. The circular beam shown in the left corner of the left panel is of size $1.45'' \times 1.45''$.

3.4 Energetics of Radio lobes

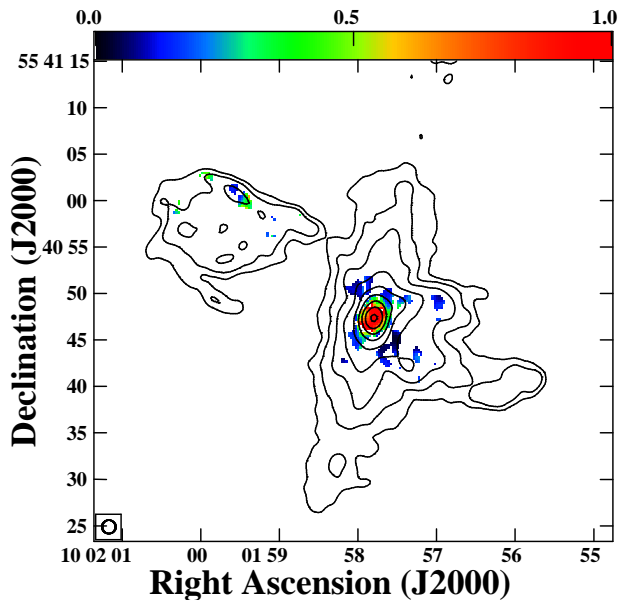


Figure 3.7: The historical VLA depolarization image of NGC 3079 in color made using the 1.4 and 5 GHz image, superimposed by the 1.4 GHz radio contours. The circular beam shown in the left corner is of size $1.45'' \times 1.45''$.

3. THE FILAMENTARY RADIO LOBES OF THE SEYFERT-STARBURST COMPOSITE GALAXY NGC 3079

the source is accreting at a rate of 0.01 to 0.1 times its Eddington luminosity. The accretion rates are consistent with that seen in high excitation radio galaxies (Best & Heckman, 2012).

The parameters derived from our radio observations of NGC 3079 are listed in Table 3.2. The parameters derived were total radio luminosity (L_{rad}), magnetic field at minimum pressure (B_{min}), minimum energy (E_{min}), minimum pressure (P_{min}), total energy (E_{tot}), energy per unit volume for a given filling factor or energy density (E_{den}) and electron lifetime from synchrotron and inverse Compton (over CMB) radiative losses (t_{life}). The minimum pressure parameters were estimated for the north-east lobes, south-west lobes, and the galactic disk separately using equations (1)-(5) from O'Dea & Owen (1987). The lifetimes were estimated using the relation given in Pérez-Torres & Alberdi (2007).

The B-array image at 5 GHz and the A-array image at 1.4 GHz were used while estimating the flux densities as these images had matched baseline coverages. These images were then convolved with the same beam size. Rectangular regions were used for estimating the flux densities. The radio spectrum was assumed to extend from 10 MHz to 10 GHz. The proton to electron ratio was assumed to be unity. Table 3.2 lists the parameters corresponding to a volume filling factor (ϕ) values of 1, 0.5 and 10^{-4} (Blustin & Fabian, 2009).

To further investigate the underlying mechanism we derive the equipartition magnetic fields for every pixel in a similar manner. A spatially resolved image of the spectral index was made instead of assuming an average spectral index value. A volume filling factor equal to unity was used. A cylindrical volume with a height equal to the width of the lobe (0.8 kpc) was assumed. The radius of the cylinder was chosen to be the same as that of the synthesized beam of the image. The pixels with flux density less than 3σ were blanked. The spectral index image and the magnetic field image of the source are shown in Figure 3.8. The VLA polarized intensity image at 5 GHz is shown overlaid in contours. The average magnetic field is $\sim 16 \pm 3\mu G$. The spectral index image shows flatter spectral indices along the ring. The equipartition magnetic field is a function of the spectral index, flux density and the volume of the emitting region. If one assumes a constant spectral index, the magnetic field trend follows the flux density pattern which is brighter along the ring.

3.4 Energetics of Radio lobes

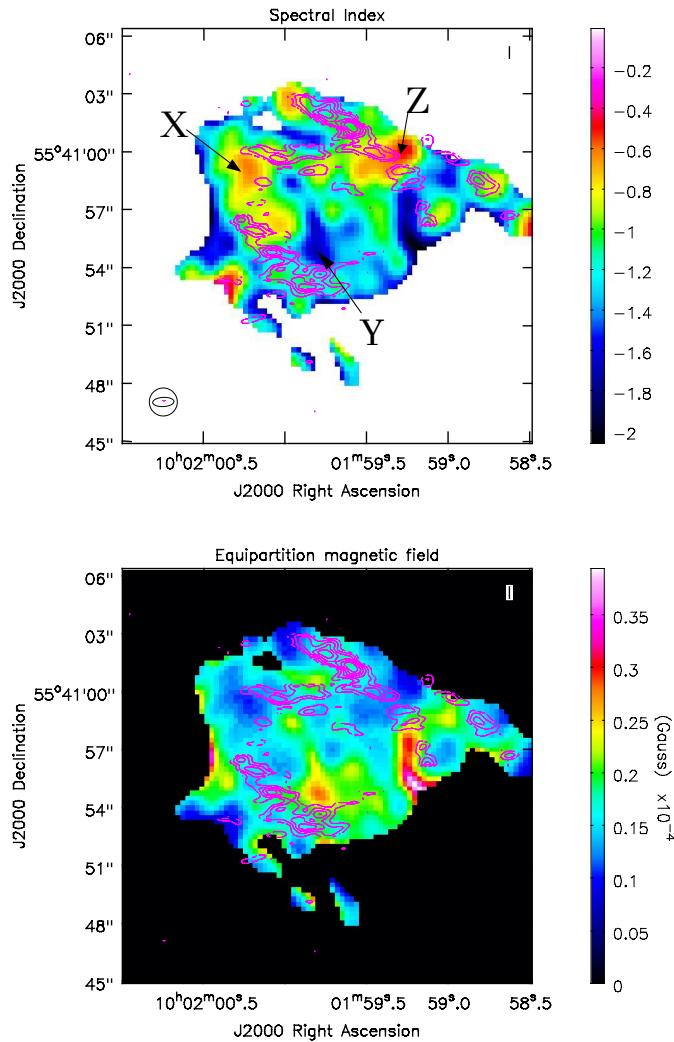


Figure 3.8: (Top) The spectral index image and (bottom) equipartition magnetic field image in colour, of the north-eastern lobe made using the 1.4 GHz and 5 GHz historical VLA images. The pink contours denote the VLA polarized intensity at 5 GHz. The left bottom corner shows the 1.4 and 5 GHz historical VLA circular beams enclosing the elliptical VLA beam at 5 GHz.

3. THE FILAMENTARY RADIO LOBES OF THE SEYFERT-STARBURST COMPOSITE GALAXY NGC 3079

The spectral index and the magnetic field structure is quite complex. Several regions along the ring like those marked X & Z in Figure 3.8, shows flat spectrum, whereas region Y show steep spectrum. Region Y forms the inner part of the ring as seen at 1.4 GHz. The width of the ring is not as large at 5 GHz, where most of the emission is confined to the outer edges where the spectral indices are flatter as well. Region Y also shows high magnetic field values though polarized emission is not detected at 5 GHz probably because of the steep spectrum which reduces the total intensity and thereby polarized flux density or because of the absence of ordered magnetic fields or both. Although the regions X and Z also show flatter spectrum, the magnetic fields values are low which might be a reason for not detecting much-polarized emission. The apparent anti-correlation between magnetic field strength and the radio spectral index can be explained by enhanced synchrotron losses in a high magnetic field region.

Table 3.2: Source parameters estimated from the “minimum energy” condition

Component	L_{rad} (erg/s)	B_{min} (Gauss)	E_{min} (ergs)	P_{min} (dynes/cm ²)	E_{tot} (ergs)	E_{den} (ergs/cm ³)	t_{life} (yrs)
filling factor=1.0							
NE lobes	7.2×10^{39}	3.07×10^{-5}	9.3×10^{54}	8.7×10^{-11}	1.16×10^{55}	1.9×10^{-10}	3.88×10^6
SW lobes	7.9×10^{39}	3.45×10^{-5}	8.6×10^{54}	1.11×10^{-10}	1.07×10^{55}	2.4×10^{-10}	3.26×10^6
Disk	2.2×10^{41}	5.13×10^{-5}	1.3×10^{56}	2.44×10^{-10}	1.63×10^{56}	5.2×10^{-10}	1.81×10^6
filling factor=0.50							
NE lobes	7.2×10^{39}	3.74×10^{-5}	6.9×10^{54}	1.3×10^{-10}	8.6×10^{54}	2.8×10^{-10}	2.90×10^6
SW lobes	7.9×10^{39}	4.21×10^{-5}	6.4×10^{54}	1.6×10^{-10}	8×10^{54}	3.5×10^{-10}	2.43×10^6
Disk	2.2×10^{41}	6.2×10^{-5}	9.6×10^{55}	3.6×10^{-10}	1.2×10^{56}	7.8×10^{-10}	1.35×10^6
filling factor= 1.0×10^{-4}							
NE lobes	7.2×10^{39}	0.00042	2.0×10^{53}	1.68×10^{-8}	2×10^{53}	3.61×10^{-8}	0.08×10^6
SW lobes	7.9×10^{39}	0.00048	2.0×10^{53}	2.14×10^{-8}	2×10^{53}	4.58×10^{-8}	0.06×10^6
Disk	2.2×10^{41}	0.00071	2.5×10^{54}	4.71×10^{-8}	3.1×10^{54}	1.01×10^{-7}	0.04×10^6

Column 1: Radio source components including the north-east (NE), southwest (SW) lobes and the galactic “Disk” minus the AGN. Column 2: Total radio luminosity. Columns 3, 4, 5 : “Minimum energy” magnetic field strength, energy and pressure, respectively. Column 6: Total energy. Column 7: Total energy density. Column 8: Electron radiative lifetimes via synchrotron and inverse Compton (over CMB) losses. See Section 3.4

3. THE FILAMENTARY RADIO LOBES OF THE SEYFERT-STARBURST COMPOSITE GALAXY NGC 3079

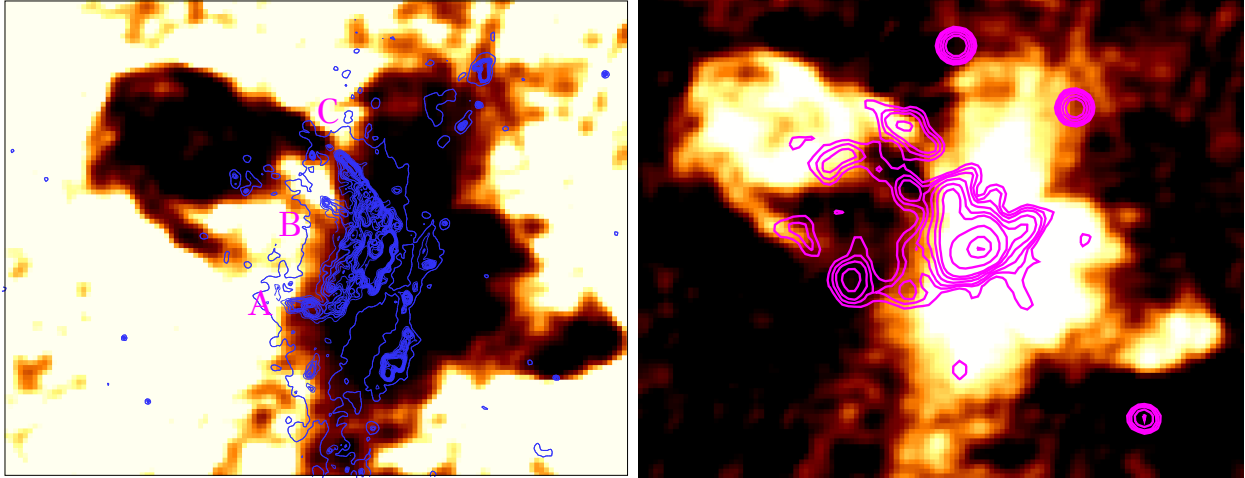


Figure 3.9: (Left) Overlay of the contours representing the *HST* WFPC2 $H\alpha$ + $[NII]$ line emission in blue and (right) Chandra ACIS-S X-ray emission in pink, over the total intensity image in colour of NGC 3079 with the historical VLA A-array at 1.4 GHz.

3.5 The origin of the ring and filamentary morphology

In this section, we try to understand the origin of the peculiar morphology of the radio lobes in NGC 3079 using our radio observations in conjunction with the existing results from the X-ray and emission line data from the literature.

Cecil et al. (2002) find evidence for a large scale diffuse X-ray halo surrounding the radio superbubble which is delineated by $H\alpha$ filaments at wide angles. These $H\alpha$ filaments were explained as the contact discontinuity between the shocked wind and the galaxy halo gas. The inner four filaments of $H\alpha$ emission form the walls of the superbubble (Cecil et al., 2001). Cecil et al. (2001) infer that the radial velocities in these filaments increase with distance from the disk. They also find that the four filaments get disrupted at some height which was explained as a result of Rayleigh-Taylor instabilities that may develop in the case of wind-driven superbubbles.

The three prominent radio filaments, (A, B and C) mentioned in Section 3.3, at first glance, appear to be aligned with the ionized filaments seen in the $[N II]$

3.5 The origin of the ring and filamentary morphology

$\lambda 6583 + H\alpha$ line emission image (Cecil et al., 2001).

Figure 3.9 shows the overlay of the Hubble Space Telescope WFPC2 $H\alpha + [NII]$ emission line contours and Chandra ACIS-S X-ray emission contours over the radio continuum historical VLA A-array image at 1.4 GHz. There is no one-to-one correspondence between the radio and the thermal emission filaments (see Figure 3.9).

The $[N II] \lambda 6583 + H\alpha$ line emission image shows no counterpart for the south-western lobes due to extinction, although there is soft-X-ray emission (Cecil et al., 2002). Among the three radio filaments that seemingly arise from the radio core, the filament marked C is aligned with the $H\alpha$ filaments. Such a correlation was previously seen in M82 by Adebahr et al. (2013). They suggested that this could be a proof for magnetic fields that are frozen into the ionized medium and get transported along with the superwind.

However, there are several other observational signatures in NGC 3079 that cannot be explained using a simple frozen-in magnetic field. Although partially aligned, it has to be noted that the weakest radio filament (A) corresponds to the brightest $H\alpha$ filament, which is also aligned almost along the same direction as that of the parsec-scale VLBA jet. This trend goes against the frozen-in magnetic field picture, where one would expect a correlation in the brightness of the radio and $H\alpha$ filaments. The brightest radio filament being offset from the direction of the VLBI jet also poses a problem for these filaments being powered by jets, unless the jet is changing its direction or undergoing precession. Moreover, the middle radio filament annotated B in Figure 3.9 does not appear to be associated with the central $H\alpha$ filament. Cecil et al. (2002) have shown that X-ray and $H\alpha$ filaments were spatially well correlated using their high-resolution images from Chandra and HST respectively. However, radio emission which is also mostly filamentary in nature does not seem to be well correlated with the thermal filaments. In the northern lobe, the closed loop like structure appears displaced northwards compared to the emission line filaments. The dearth of emission lines and X-ray emission at the topmost loop is intriguing. The radio emission also extends farther beyond the point where the emission line gas reaches a blowout phase as a result of the growth of Rayleigh-Taylor instabilities (Cecil et al., 2001).

3. THE FILAMENTARY RADIO LOBES OF THE SEYFERT-STARBURST COMPOSITE GALAXY NGC 3079

The radio plasma and thermal emission are not completely intermixed, which would imply different sources of origin. Such lack of intermixing despite the disruption of the jet at early stages is also witnessed in X-ray cavities in clusters of galaxies, where the ambient hot gas is simply pushed aside by the expanding radio source (Bîrzan et al., 2004).

Now, we consider plausible physical mechanisms that might be playing a role in the formation of the “ring” in NGC 3079.

3.5.1 Shock compression at the boundaries of an expanding superbubble

Duric & Seaquist (1988) propose that shocks at the interface between ambient medium and the outflow would be a natural consequence of the supersonic velocities derived for the winds present in NGC 3079. Several features seen in the ring of NGC 3079 are suggestive of the presence of a shock. With our better resolution images, it can be seen that the ring-like structure is also comprised of several filaments. The entire structure is reminiscent of a supernova remnant shell. Shocks can produce synchrotron emission via diffusive shock acceleration (DSA) or Fermi first order acceleration (Blandford & Eichler, 1987). The power-law index of the energy distribution of the particles is determined by the strength of the shock, which can be described using the Mach number.

The flattening in the spectral index along the ridges of the ring at various locations might point towards the reacceleration of charged particles (see Section 3.3.2). The spectral index image shows that the spectrum is as flat as -0.5 at several locations which match with the mean spectral index values typically seen in galactic supernova remnants (Klein et al., 2018).

By using the spectral age of 4 Myrs (see Table 3.2) and an outflow length of 2.3 kpc, we obtain a wind velocity of 575 km s^{-1} . Since the velocity of the wind increases with the distance from the disk (Cecil et al., 2001), our wind velocity represents an average value of the projected wind velocities at various distances above the disk. The thermal gas traced by emission lines exhibits radial velocity that increases with distance from the disk to attain velocities as high as 1000 km s^{-1} (Cecil et al., 2001; Veilleux & Osterbrock, 1987). Since most of the

3.5 The origin of the ring and filamentary morphology

radio emission is from above the emission-line complex and assuming that the radio emission is coexisting with the superwind we can assume a radial velocity of 1000 km s^{-1} for the radio outflow as well. Hence, the total velocity of the radio outflow is $v \gtrsim 1000 \text{ km s}^{-1}$.

The sound speed in the hot wind regions present in typical starbursts is about 100 km s^{-1} (Romero et al., 2018). Hence the sonic Mach number turns out to be ~ 10 .

The spectral index, α depends on the Mach number of the shock (Blandford & Eichler, 1987; van Weeren et al., 2016) as the following

$$\alpha = \frac{1}{2} - \frac{M^2 + 1}{M^2 - 1} \quad (3.1)$$

For a sonic Mach number of 10, we obtain $\alpha \sim -0.52$. Hence the shock present in NGC 3079 is strong enough to produce the spectral index values as flat as that seen in NGC 3079 from an underlying thermal distribution of electrons.

However, we cannot rule out the scenario where an already existing relativistic population of electrons gets reaccelerated at the shock front. Detailed DSA simulations would be required to understand the contribution of the reacceleration of an already existing relativistic electron population.

Shock compression often leads to the ordering of the tangled or turbulent magnetic fields that permeate the ambient medium. The magnetic fields parallel to the shock front get amplified leading to high degrees of polarized emission aligned perpendicular to the shock fronts (Ensslin et al., 1998; Laing, 1980). The northern ring shows high fractional polarization compared to the rest of the galaxy. The polarization vectors are also aligned perpendicular to the individual filaments as expected in the case of shock amplification. The “ring” also shows higher depolarization (see Section 3.3.2) which might be due to a higher Faraday depth within or in front of it (Cioffi & Jones, 1980). So either the magnetic field or electron density (or both) is higher here. It might be that the expansion of the shell (that we see projected as a ring) is sweeping up gas, so there is a denser shell of gas along the shell. It could also be that the magnetic fields are being compressed along the edges although compressing magnetic fields can lead to higher absolute polarization (Laing, 1980).

3. THE FILAMENTARY RADIO LOBES OF THE SEYFERT-STARBURST COMPOSITE GALAXY NGC 3079

It can be seen from Figure 3.8 that the regions of flat spectral index does not show a one-to-one correspondence with regions showing high polarized signal. This might be indicative of some other mechanisms that might also have significant roles to play in the formation of the peculiar ring like structure.

3.5.2 Magnetic Draping

Bernikov & Semenov (1979); Lyutikov (2006) have pointed out that as an object moves through a weakly magnetized medium with a velocity greater than its Alfvén speed, it necessarily drags up a layer of magnetic field lines along with it. For magnetic draping to be playing a role it is required that the velocity of the wind is higher than the Alfvén velocity. Adebahr et al. (2019) show that the radio lobes of B2 0258+35 are probably being affected by magnetic draping using their polarization and HI study. We test this idea to explain the polarization structures observed in the lobes of NGC 3079.

We estimate the Alfvén velocity of the wind using the following equation.

$$v_a = 2.18 n_e^{-\frac{1}{2}} B \text{ km s}^{-1} \quad (3.2)$$

where B is the magnetic field in μG and n_e is the electron number density in cm^{-3} . For the northern lobes we have estimated an equipartition magnetic field of $20 \mu G$ (see Table 3.2). Our RM images show an average RM value of 50 rad m^{-2} . If we assume a Faraday screen path length of 100 parsecs, which is equal to the widths of the filaments as seen in our VLA images, the electron number density values turn out to be 0.03 cm^{-3} by using the relation $\text{RM} = 812 n_e B_{\parallel} dl \text{ rad m}^{-2}$. This value is of the same order as that predicted by Duric & Seaquist (1988) for the wind model. We obtain an Alfvén velocity of 250 km s^{-1} . Therefore, the wind is super Alfvénic with an Alfvénic Mach number, M_A of 4. Pfrommer & Jonathan Dursi (2010) suggest that the following criteria have to be met for magnetic draping to occur,

$$\frac{\lambda_B}{R} \gtrsim \frac{1}{M_A} \quad (3.3)$$

where λ_B is the magnetic coherence length. The thickness of the polarized filaments in our image which is about 100 pc can be regarded as a lower limit of the magnetic coherence length. Assuming a radius of curvature, $R \sim 0.4 \text{ kpc}$,

3.5 The origin of the ring and filamentary morphology

we obtain a value for the ratio of $\frac{R}{M_A}$ which is similar to the magnetic coherence length. So magnetic draping is a viable mechanism that could be playing a role in the formation of the ring-like morphology.

Dursi & Pfrommer (2008) argue that if magnetic draping is occurring the polarization structure can be used to identify the alignment of the large scale magnetic field. Though the ring is closed on top in the total intensity image, the polarized emission is not detected at the top, suggesting lower fractional polarization values. This might be because the ambient magnetic field is parallel to the minor axis and hence gets amplified when the radio plasma expands sideways rather than towards the top of the “ring”. As was pointed out in Section 3.4, despite the flattening of the spectrum at regions X (refer Figure 3.8), the equipartition magnetic field as well as the polarized intensity values are less which also supports the idea of a large scale poloidal magnetic field threading the galaxy.

Magnetic draping can also provide stability against the growth of fluid instabilities. Therefore magnetic fields could probably explain why the radio plasma extends beyond the blowout of the thermal gas (Cecil et al., 2001).

3.5.3 Filaments as magnetic flux tubes

Similar to NGC 3079, NGC 253, a starburst galaxy hosting superwinds possesses magnetic fields which are aligned along the filaments. Heesen et al. (2011) model the walls of the outflow cones of the galaxy to be threaded by helical magnetic fields as indicated by RM inversion. They appear as filaments in projection. But unlike NGC 3079, there are only two filaments each at the edge of the outflow cone. If the inner $H\alpha$ or radio filaments actually trace the wall of a superbubble in the case of NGC 3079, the expectations would be to see edge-brightened structures in projection or a completely filled volume rather than discrete filaments at intermediate angles.

The presence of separate filaments in between the edge filaments in NGC 3079 casts doubts over the simple picture of these being the edge of the walls seen in projection. Cecil et al. (2001) have studied the rotation measure of the northern ring of NGC 3079. They have found that the RM changes its sign from the $+50 \text{ rad m}^{-2}$ on the inside of the ring to -50 rad m^{-2} on the outside. We note

3. THE FILAMENTARY RADIO LOBES OF THE SEYFERT-STARBURST COMPOSITE GALAXY NGC 3079

that our VLA in-band RM image exhibits average RM values in the same range and also shows the RM inversion. In our RM image of the northern lobe (see Figure 3.6) we see the RM inversion in individual filaments on the right hand side although the polarized emission with positive RM has not yet been recovered.

Cecil et al. (2001) put forth three explanations for the observed RM inversion. In their first model, they consider that the wind entrains material from the cold disk with a frozen in magnetic field which is transported upstream and gives rise to the positive RM values. Once the disk material cools down the material starts falling back resulting in the reverse fields.

Secondly, they consider a globally ordered magnetic field of the halo, which surrounds the wind. The negative RM results from the compressed halo gas whereas the outflowing wind contributes to the positive RM. In both these models, the outer shells lead to a positive RM while material inside leads to negative RM. However, as they had pointed out in Section 3.5 of their paper, Faraday rotation closely follows a λ^2 dependence which rules out a Faraday rotating medium within the synchrotron source. Therefore it is unlikely that the outflowing wind enclosed within either the host galaxy halo or the wind material that is falling back to the disk is giving rise to the positive RM.

They propose a third scenario which is similar to the solar prominence. Here, we consider the possibility of these being actual standalone filaments, in which case the RM inversion seen in the individual filaments can be easily explained using a helical magnetic field structure. The rotation is probably introduced by a sheath around the filaments with increased particle density and width about 10 % of the filament size itself. The sheath which is threaded by a helical magnetic fields can introduce such an inversion. A helical magnetic field morphology is often invoked to explain the RM inversion seen in VLBI scale jets (Clausen-Brown et al., 2011; Kharb et al., 2009; Pudritz et al., 2012). The morphology of radio filaments that are anchored to the core is especially reminiscent of the non-thermal radio filaments found in the Galactic center (Morris et al., 2014). The Galactic center filaments also possess organized magnetic fields often aligned along the filament similar to that seen in NGC 3079. It is possible that these filaments are magnetic flux tubes through which the relativistic material is transported from the core to the top.

3.6 Role of the jet in inflating the radio bubble

Radio halos were discovered in several starburst galaxies (Allen et al., 1978; Carilli et al., 1992; Duric et al., 1998; Ekers & Sancisi, 1977). These were believed to be composed of the material that was convected up from the central starburst regions, where it was created by supernovae (Lerche & Schlickeiser, 1980). However, these radio halos which are purely powered by starbursts have a very different morphology compared to NGC 3079 (Colbert et al., 1996b). These radio halos are more spherical and diffuse whereas NGC 3079 shows two distinctly directional lobes. Irwin & Seaquist (1988) argue that the large scale radio lobes and the VLBI scale jet are unusual in spiral galaxies and are therefore probably related. In this section, we investigate the role of the jet in actually inflating the radio bubbles. Star formation rates (SFR) from the radio flux density of north-east lobes, south-west lobes and the disk are 2.58, 2.14 and 17.87 M yr^{-1} respectively (using the relations in Condon et al., 2002) for stars more massive than $>0.1 \text{ M}_\odot$. Yamagishi et al. (2010) have estimated SFR using AKARI far-infrared data. They find that the SFR is 5.6 M yr^{-1} in total and 2.6 M yr^{-1} in the central 4 kpc region. The SFR estimated in the east and west lobes together exceed that estimated from IR emission in the central regions by about a factor of 2. Therefore, it is unlikely that the lobes are composed of plasma that is accelerated solely by supernovae and stellar winds. A certain contribution from the jet is inevitable unless the radio emission is generated as a result of in-situ particle acceleration in the lobes due to shocks (see Section 3.5.1).

Energy and pressure requirements of the radio lobe can provide constraints on the origin of the bubble. Duric & Seaquist (1988) invoke accretion along with a nuclear starburst due to the very high rates of star formation required to meet the energy budget. Although the AGN at the core is weak, the radio jet on VLBI scales, as was pointed out by Irwin & Seaquist (1988), is capable of powering the superbubble.

Irwin & Seaquist (1988) compare the momentum flux that is required to feed the kpc-scale radio lobes to the pc-scale jets. They find that the momentum flux of the pc-scale jets is $3 \times 10^{31} h^{-\frac{10}{7}} \text{ g cm s}^{-2}$ while that of the north-eastern radio lobe is $1 \times 10^{32} h^{\frac{-10}{7}} \text{ g cm s}^{-2}$. However, these values are three orders in

3. THE FILAMENTARY RADIO LOBES OF THE SEYFERT-STARBURST COMPOSITE GALAXY NGC 3079

magnitude lower compared to the wind model parameters of Duric & Seaquist (1988). Following Irwin & Seaquist (1988) we assume a slab volume with size 1.1 kpc. We find a momentum flux value of $1 \times 10^{33} h^{-\frac{10}{7}} \text{ g cm s}^{-2}$ for the north-eastern lobe for a filling factor value of 1.0. Irwin & Seaquist (1988) pointed out that the momentum flux of the lobes derived is a lower limit owing to the underlying minimum energy assumption. When we use a filling factor value of 1×10^{-4} (Blustin & Fabian, 2009) we find a momentum flux value of $2 \times 10^{35} h^{-\frac{10}{7}} \text{ g cm s}^{-2}$, which is comparable to the momentum flux derived from wind model parameters (Duric & Seaquist, 1988). Interestingly, for the volume filling factor of 1×10^{-4} , the radio lobes are overpressured with respect to the surrounding hot gas. Thus, momentum flux requirements of both the wind and the radio lobe model can be met by the pc scale jet in NGC 3079.

Shafi et al. (2015) estimate the jet power of NGC 3079 using various relations that connect radio luminosities to jet power. Their estimated value of $10^{41} \text{ ergs s}^{-1}$ is two orders of magnitude lower than that required by the wind model in Duric & Seaquist (1988). However the uncertainties in the relations used for conversion is often high that this difference is consistent with the wind model within error bars.

The radio continuum emission in NGC 3079 is very different from the typical jet lobe morphology seen in powerful radio galaxies. Several VLBI studies had revealed that the jet in NGC 3079 is expanding with mildly relativistic speeds in the range 0.1c to 0.18c (Kondratko et al., 2005; Sawada-Satoh et al., 2000; Trotter et al., 1998). It is also known that Seyfert galaxies often host very low power jets which often get disrupted or show S-shaped or twisted morphology (Booler et al., 1982; Kharb et al., 2006; Ulvestad et al., 1981; Wehrle & Morris, 1988; Wilson & Ulvestad, 1982, 1983). Therefore it is probable that the jet in NGC 3079 got disrupted due to its interaction with the ambient medium or an accretion disk wind. This disrupted jet material probably gets transported out along with the superwind. As discussed in Section 3.5, the lack of correlation of radio plasma with the superwind also suggests that the jet might be playing an important role. We, therefore, conclude that the jet, the active nuclei, and the superwind together give rise to the peculiar lobe morphology in NGC 3079 which is neither similar to a typical AGN jet or a starburst radio halo.

3.7 Summary and Conclusions

Precession jet model can connect the VLBI jet to the large scale lobes with a jet precession period of $\sim 10^5$ yrs using the precession model of Hjellming & Johnston (1981). For instance, fixing the jet speed to be the one observed on VLBI scales ($v \sim 0.2c$) yields a precession period of 9.5×10^4 yrs for a precessing cone half opening angle of 10° and jet inclination of 20° , for the north-eastern lobe. However, one episode of precession is insufficient to explain the entire complex morphology of the jet lobe structure.

3.7 Summary and Conclusions

We have carried out a multi-frequency multi-scale radio study of NGC 3079, a Seyfert 2 galaxy which also hosts a nuclear starburst. The origin of the radio continuum emission in this galaxy is widely debated. With our high resolution and high sensitivity data, we favor a scenario which involves an interplay of various processes and outflows. Our findings can be summarized as follows.

1. There is no one-to-one correlation between the thermal emission (traced by X-ray and emission line) and non-thermal emission (traced by radio), which is inconsistent magnetic fields frozen-in within the superwind hot material and being transported out. A disrupted jet would have both the relativistic particles and the magnetic field and hence could be a possible alternative to explain the radio emission.
2. We propose that the filamentary structures are not merely edges of the superbubble seen in projection, but actual individual filaments (see Section 3.5.3). The RM inversion observed in the individual filaments can also be easily explained using such a scenario. Each filament is like a jet segment threaded by helical magnetic fields.
3. We find that the conditions in NGC 3079 are favorable for both magnetic draping and shock acceleration to happen. The peculiar morphology might be a result of the interplay of both these mechanisms. However, detailed simulations would be required to disentangle the role played by each.

3. THE FILAMENTARY RADIO LOBES OF THE SEYFERT-STARBURST COMPOSITE GALAXY NGC 3079

4. The SFR estimated from the lobes suggest that supernovae and stellar outflows cannot feed the lobe material entirely and a contribution from the AGN jet is required. As discussed in section 3.5.1, shock acceleration of the thermal pool of electrons in the wind has not been ruled out. It is not entirely clear if all the emission can be accounted for by this mechanism. An observational test would be to check whether such a radio excess is seen in other starburst galaxies hosting superwinds in which an AGN core is absent.

We conclude that the AGN jet contributes to the relativistic plasma that is observed in the lobes of NGC 3079. We, therefore, propose that the radio lobes in NGC 3079 are AGN jet-related. However, the presence of starburst superwind is also indicated, and it is hard to discriminate the effects of each mechanism.

4

The Seyfert and the Starburst galaxy sample¹

4.1 Introduction

It is known that only a fraction ($\sim 10\%$) of active galaxies host powerful radio jets which in some cases extend up to several Mpc in size (Begelman et al., 1984). The question of why some active galaxies host powerful jets and others not, is yet to be settled. While the origin of radio emission in radio loud AGN with the radio loudness parameter, $R \gg 10$, is decidedly attributed to jets powered by the central engine, this is not true for radio quiet AGN. Although many studies have contested this RL/RQ bimodality and have argued in favour of a continuous distribution (Bonchi et al., 2013; Lacy et al., 2001; Wals et al., 2005; White et al., 2007), several studies have suggested mechanisms other than jets to explain the radio emission seen in radio-quiet AGN. Several possibilities that can lead to radio emission in radio-quiet AGN that have been discussed in the literature include star formation driven superwinds, winds driven by the AGN, the coronal activity of the accretion disk, or jets which are intrinsically low powered (see Panessa et al. (2019) and references therein).

Radio synchrotron emission seen in starburst galaxies owes its origin to supernovae and stellar winds which give rise to the relativistic electron popula-

¹The contents of this chapter have been published in [Sebastian et al., MNRAS, 2020, arXiv: 2008.06039](#), see here.

4. THE SEYFERT AND THE STARBURST GALAXY SAMPLE

tion. This electron population combined with the large-scale magnetic fields that thread the galaxy gives rise to the observed radio synchrotron emission in these systems. This emission is diffuse and present at the scales of the galaxy and beyond. The polarized emission from these radio halos of starburst galaxies often shows X-shaped morphology (Beck, 2015; Krause et al., 2020).

Ultrafast outflows observed in X-rays (Pounds, 2014; Tombesi et al., 2010) and broad absorption lines in several quasars (Everett, 2007) are thought to be signatures of AGN driven winds. The supersonic velocities of these radiatively/thermally driven winds result in shock acceleration of particles which in turn leads to synchrotron emission (Hwang et al., 2018; Nims et al., 2015; Zakkamska & Greene, 2014). Yet another mechanism proposed for the origin of the radio emission is the free-free emission mechanism from the optically thin plasma in the wind (Blustin & Fabian, 2009). The spectral slope of the radio emission is expected to be $\alpha = -0.1$ (using $S_\nu \propto \nu^\alpha$) in this case. However, in most of the Seyfert galaxies, we find steeper spectral indices in the larger scale emission diminishing the importance of this mechanism. Magnetohydrodynamically launched winds are an alternative to the radiation driven winds and have been proposed to explain outflows observed in the X-ray (Fukumura et al., 2015). It has also been proposed in the literature that the radio emission is coronal in origin as suggested by the correlation between the radio and X-ray luminosity observed in these systems (Laor & Behar, 2008; Panessa et al., 2007). However, such coronal emission might be confined to the core region with the kpc-scale radio emission being unrelated to it. More work needs to be done in this context.

Seyfert galaxies are usually classified as radio-quiet in nature. Yet, when nuclear optical emission is properly accounted for, either by using high-resolution optical imaging from the Hubble Space Telescope (HST) or by removing galactic contribution, $> 50\%$ of Seyfert galaxies wind up as “radio-loud” (RL) sources with $R > 10$ (Ho & Peng, 2001; Kharb et al., 2014b). High angular resolution studies like those by Kukula et al. (1995); Thean et al. (2000, 2001); Ulvestad et al. (1981) show compact nuclear structures and sometimes evidence for multiple components, suggesting the presence of low-power jets. Moreover, kiloparsec-scale radio structures (KSR) of extents $\sim 1 - 10$ kpc, have been detected in a large

4.1 Introduction

fraction of them in complete samples (Baum et al., 1993; Colbert et al., 1996b; Gallimore et al., 2006).

However, the debate on the origin of KSRs is yet to be settled. While studies like Baum et al. (1993) suggested KSRs are starburst wind driven, later studies have favored an AGN jet driven origin (e.g., Colbert et al., 1996b). The observed misalignment between the KSRs and their host galaxy minor axes (e.g., Gallimore et al., 2006); the presence of relic lobe emission around KSRs (e.g., Kharb et al., 2016); and the presence of parsec-scale radio jets leading into lobes (e.g., Kharb et al., 2014a), favor an AGN jet driven scenario.

Gallimore et al. (2006) suggest that a low-power jet that starts from the central engine gets disrupted as soon as it interacts with the dense ISM of these Seyfert galaxies and loses its stability after which the radio plasma simply follows the steepest path in pressure gradient, which is along the minor axis of the host galaxy. This model can also explain the misalignment of the jet with the large scale lobe alignment, typically seen in these galaxies (Schmitt et al., 2001).

In this chapter, we try to obtain more insights into the origin, nature, and evolution of the radio emission from Seyfert galaxies using a comparative study between a sample of Seyfert galaxies versus that of starburst galaxies. In the previous chapter and the upcoming chapter, we present detailed multi-frequency studies of two of the Seyfert galaxies from our sample, viz., NGC 2639 (Sebastian et al., 2019a) and NGC 3079 (Sebastian et al., 2019b). Our primary aim is to try and understand how the linear polarization properties vary between the population of Seyfert galaxies and starburst galaxies. Previous studies of starburst galaxies reveal magnetic fields that follow the spiral arms of the galaxy or the minor axis and is generated as a result of the dynamo process at play in the galaxy (Beck, 2015). Hence, in the case for a purely starburst origin of radio emission, the magnetic field alignment should be along the galaxy minor axes and the ordering scales similar to sizes comparable to that of the galaxy itself. On the other hand, if the radio emission has a jet origin, the magnetic field orientation need not be along the disk or the galaxy minor axes, and the magnetic field ordering scales can be either in collimated or diffuse outflows. One would also expect to see systematic differences between a Seyfert galaxy sample versus a

4. THE SEYFERT AND THE STARBURST GALAXY SAMPLE

starburst galaxy sample in terms of fractional polarization and rotation measure features.

This chapter is organized in the following manner. In Section 4.2, we have described our sample selection criteria after which we explain the details of our observations and the data analysis procedures in Section 4.3. In Section 4.4 we elucidate the radio morphology of individual target sources in the context of the existing literature and the polarization properties for the entire sample. We then discuss the implications of our results in Section 4.5.

4.2 The Sample

We chose a sample of Seyfert galaxies along with a comparison sample of starburst galaxies. The Seyfert galaxies were chosen from the sample of nearby AGNs from the Center for Astrophysics (CfA; Huchra & Burg (1992)) and extended 12 μm (Rush et al., 1993) surveys. Our sample was selected based on the following criteria: (i) all the sources had redshifts below 0.017 so that the angular resolutions correspond to similar physical extents for various sources, (ii) sources were restricted to declinations above -20° for VLA visibility, and (iii) had total lobe to lobe extents derived from Gallimore et al. (2006) greater than 20 to be able to choose sources which showed reliable KSR emission spanning several resolution elements and also to be able to undertake a detailed analysis of the morphology of these KSRs.

The starburst galaxies were selected from the samples of Dahlem et al. (1998) and Colbert et al. (1996b). We chose five of the seven “edge-on” starburst galaxies from Dahlem et al. (1998) that showed clear radio emission above and below their galactic disks in arcsecond-scale radio images. These are NGC 253, NGC 3079, NGC 3628, NGC 4631, and NGC 4666¹. Interestingly, three of these, viz., NGC 253, NGC 3628 and NGC 4666, have been classified as LINERs and are likely to be hosting AGN nuclei at their cores. To increase the sample size, we also selected “edge-on” starburst galaxies from Colbert et al. (1996b), which

¹NGC 4666 and NGC 4594 were finally not observed by the VLA because they were low in the scheduling queue. However, these sources have recently been observed by us at 10 GHz. These results will be presented in a forthcoming paper.

4.2 The Sample

are matched with the Seyfert galaxies in terms of their radio luminosities, axial ratios, and redshifts. This additional sub-sample includes NGC 1134, NGC 3044, NGC 7541 and UGC 903. All the nine chosen starburst galaxies have IRAS $60\mu\text{m}$ luminosities, $L_{60\mu\text{m}} 2 \times 10^{43} \text{ ergs s}^{-1}$.

Table 4.1: Observation log and observed parameters.

Source	R.A.	Dec.	Observation Date	Redshift	Frequency (GHz)	VLA Array Configuration	Beam, PA (arcsec ² , °)	Major axis of the beam in kpc	on-source time (in min)	r.m.s. (in μJy/beam)
Seyfert galaxies										
NGC2639	08h43m38.10s	+50d12m19.99s	04–Nov–2017	0.0111	5.5	B	$1.1 \times 1.0, -5.73$	0.24	26.75	8.829
NGC2992	09h45m42.00s	-14d19m34.99s	30–Jan–2018	0.0077	5.5	BnA	$1.5 \times 0.9, -17.01$	0.228	29.1	10.59
NGC3079	10h01m57.79s	+55d40m47.00s	16–Feb–2018	0.0037	5.5	BnA	$1.1 \times 0.5, -87.08$	0.081	28.8	25.57
NGC3516	11h06m47.49s	+72d34m07.00s	05–Feb–2018	0.0088	5.5	BnA	$1.2 \times 0.5, -73.74$	0.208	26.7	13.09
NGC4051	12h03m09.60s	+44d31m53.00s	24–Feb–2018	0.0023	5.5	BnA->A	$1.7 \times 0.9, -78.42$	0.078	25.55	14.36
NGC4235	12h17m09.90s	+07d11m29.99s	27–Feb–2018	0.0080	5.5	BnA-> A	$0.7 \times 0.3, -59.1$	0.11	13.8	21.35
NGC4388	12h25m46.70s	+12d39m44.00s	31–Jan–2018	0.0084	5.5	B->BnA	$2.2 \times 1.5, 39.17$	0.248	26.6	45.08
NGC4593	12h39m39.40s	-05d20m39.00s	13–Feb–2018	0.0090	5.5	BnA	$2.7 \times 0.5, -60.27$	0.479	26.7	33.42
NGC5506	14h13m14.90s	-03d12m27.00s	27–Feb–2018	0.0062	5.5	BnA-> A	$1.2 \times 0.6, -58.8$	0.147	26.55	134.43
starburst galaxies										
NGC1134	02h53m41.29s	+13d00m50.99s	03–Nov–2017	0.0121	1.5	B	$6.2 \times 4.1, -58.3$	1.472	25.55	24.61
NGC253	00h47m33.10s	-25d17m18.00s	31–Oct–2017	0.0008	1.5	B	$9.6 \times 3.2, -19.36$	0.153	29.2	205.06
NGC3044	09h53m40.90s	+01d34m46.99s	26–Nov–2017	0.0043	5.5	B	$3.9 \times 1.6, -55.67$	0.341	29.5	30.076
NGC3628	11h20m17.00s	+13d35m23.00s	27–Feb–2018	0.0028	5.5	BnA->A	$0.5 \times 0.3, -68.7$	0.028	14.25	9.601
NGC4631	12h42m08.00s	+32d32m29.00s	12–Jan–2018	0.0020	5.5	B	$1.5 \times 1.1, -80.36$	0.06	25.55	9.659
NGC7541	23h14m43.90s	+04d32m04.00s	25–Sep–2017	0.0090	1.5	B	$4.4 \times 3.9, -57.33$	0.78	26.65	39.68
UGC903	01h21m47.80s	+17d35m33.00s	04–Nov–2017	0.0084	1.5	B	$8.3 \times 4.0, 63.79$	1.374	24.6	22.2

4.3 Observations and Data analysis

The sample was observed using the VLA in B-array configuration under the project ID: 17B-074 during 2017-2018.

All the Seyfert galaxies and three of the starburst galaxies were observed at 5.5 GHz and four of the starburst galaxies were observed at 1.4 GHz. From past studies, it is well known that Seyfert galaxies show radio emission from parsec to kpc scales whereas most of the radio continuum studies of starburst galaxies show emission majorly from the large scales comparable to the galaxy itself. The largest angular scale that can be measured at C-band using B-array configuration is about 29'', so any larger spatial scales of emission will be resolved out in C-band observations. This study serves as a pilot study to understand the ideal frequencies and resolution for carrying out a comparative study between starburst galaxies and Seyfert galaxies. Hence, some of the starburst galaxies were observed at 1.5 GHz and some at 5.5 GHz.

The details of the observations are provided in Table 4.1. 3C 138, 3C 286, and 3C 48 were observed to calibrate the flux densities and polarization angles. Suitable phase calibrators were also observed to correct for the ionospheric phase errors. OQ 208, and 3C 84 were the unpolarized calibrators observed to correct for the instrumental leakage from these antennas.

CASA calibration pipeline for VLA data was used to carry out the basic editing and calibration of the ‘Stokes I’ data after which polarization calibration was carried out separately. We corrected the cross-hand delays between the two polarizations. The model of the polarization calibrator was fed manually using the CASA task ‘SETJY’ as elaborated in Sebastian et al. (2019b).

After calibrating for the D-terms using the unpolarized calibrator with the CASA task ‘polcal’, we corrected for the polarization angle (aka electric vector position angle, EVPA) with reference to the known polarization angle of the polarized calibrator. Either 3C 138, or 3C 286 was used as the polarization angle calibrator for the observations carried out at 5.5 GHz, whereas 3C 48 was used at 1.5 GHz. Since the fractional polarization of 3C 48 is too low ($\sim 0.5\%$ at 1.5 GHz) to provide reliable solutions, we combined all spectral windows while determining the cross-hand delays so that these delays are relatively accurate. 3C 48 was also

4. THE SEYFERT AND THE STARBURST GALAXY SAMPLE

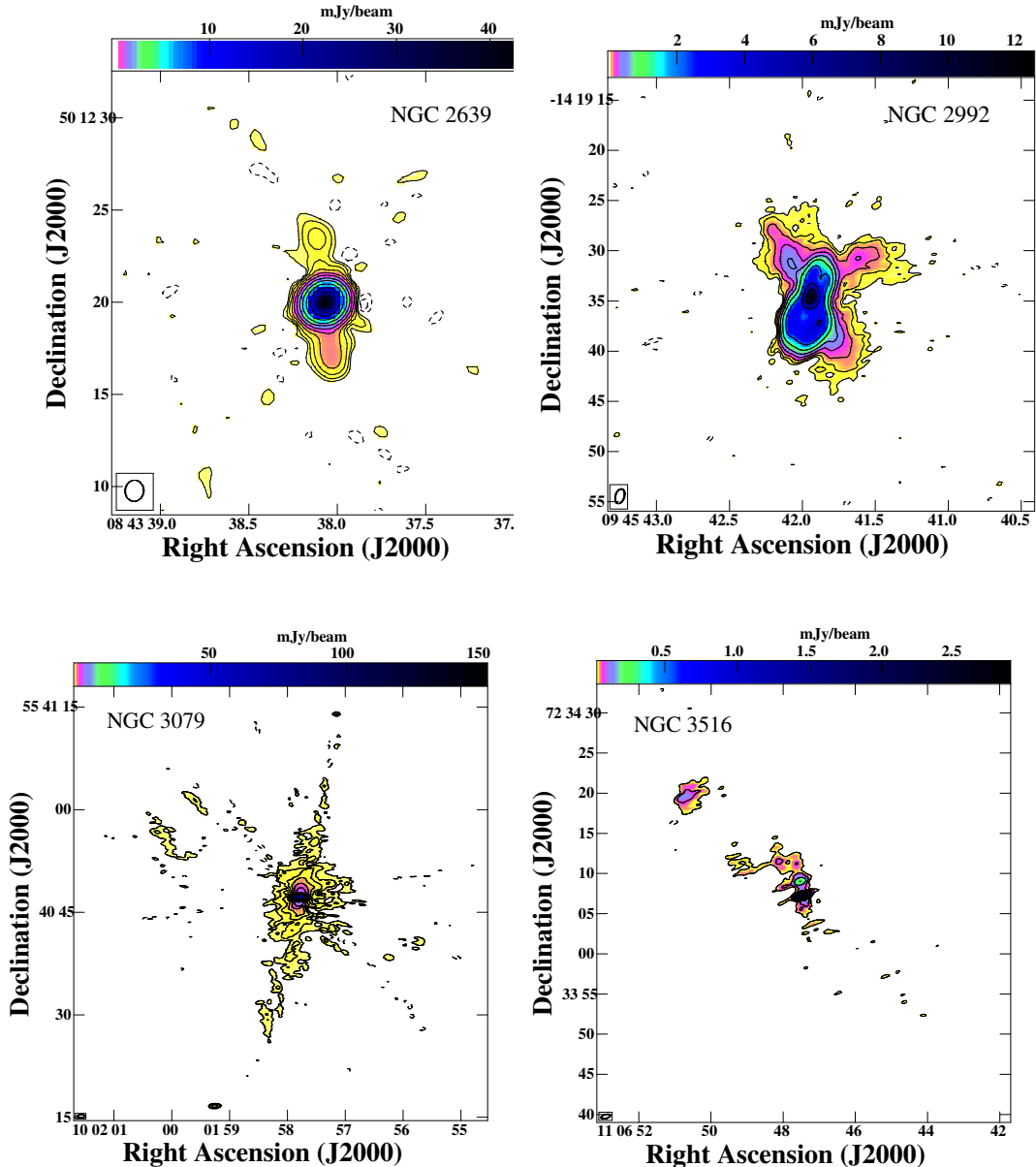


Figure 4.1: Total intensity images of Seyfert galaxies at 5.5 GHz. The contour levels used are $3\sigma \times (-2, -1, 1, 2, 4, 8, 16, 32, \dots)$, where $\sigma = 8.83, 10.59, 25.57, 13.085 \mu\text{Jy beam}^{-1}$ for NGC 2639 (top left), NGC 2992 (top right), NGC 3079 (bottom left), NGC 3516 (bottom right) respectively.

4.3 Observations and Data analysis

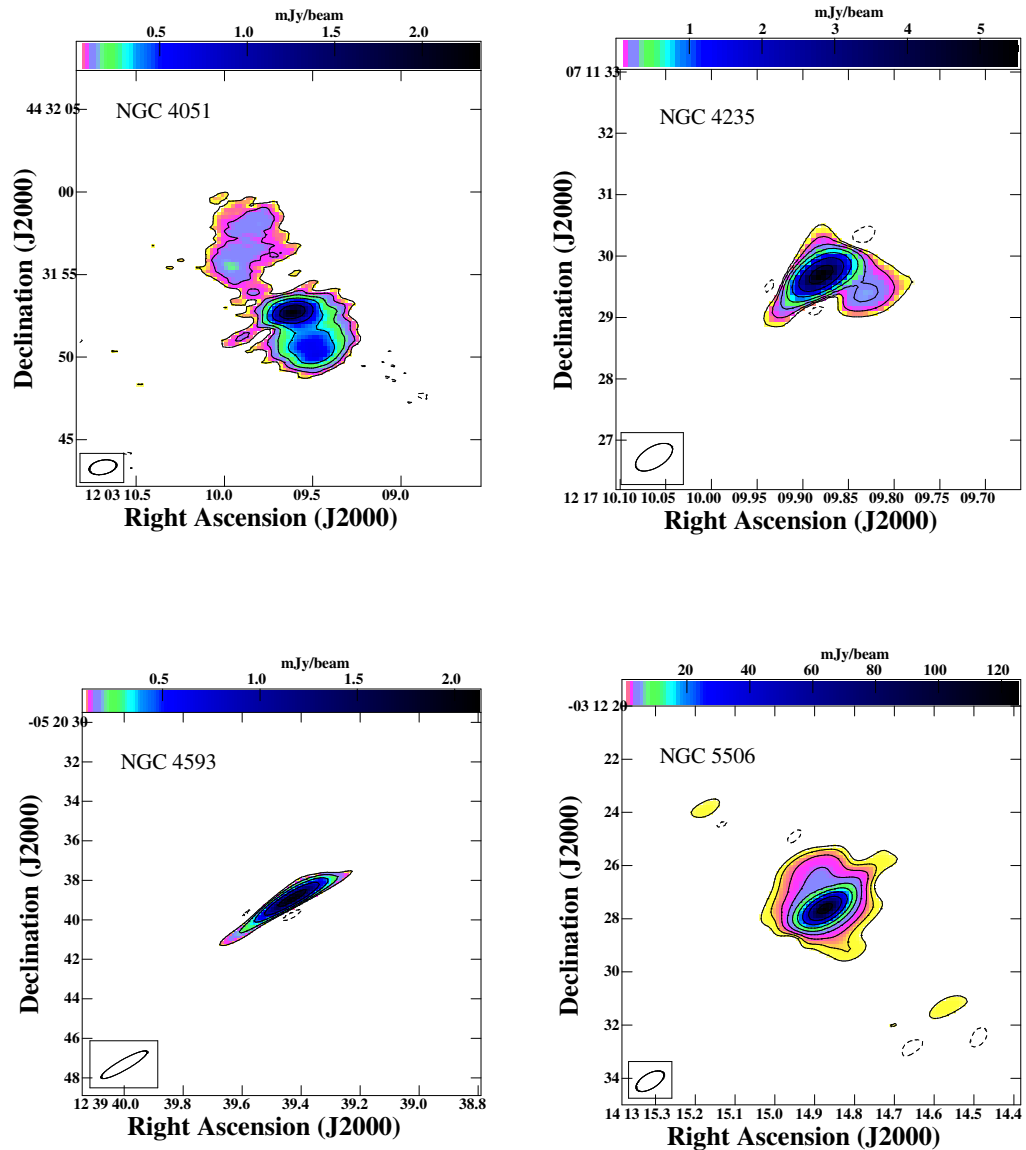


Figure 4.1: Continued –Total intensity images of Seyfert galaxies at 5.5 GHz. The contour levels used are $3\sigma \times (-2, -1, 1, 2, 4, 8, 16, 32 \dots)$, where $\sigma = 14.36, 21.35, 33.42, 134.43 \mu\text{Jy beam}^{-1}$ for NGC 4051 (top left), NGC 4235 (top right), NGC 4593 (bottom left), NGC 5506 (bottom right) respectively.

4. THE SEYFERT AND THE STARBURST GALAXY SAMPLE

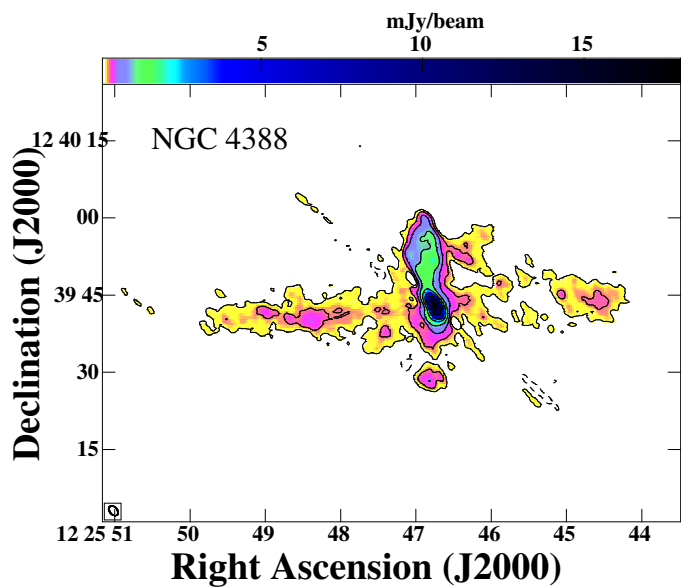


Figure 4.1: Continued – Total intensity images of Seyfert galaxies at 5.5 GHz. The contour levels used are $3\sigma \times (-2, -1, 1, 2, 4, 8, 16, 32 \dots)$, where $\sigma = 45.08 \mu\text{Jy beam}^{-1}$ for NGC 4388.

4.3 Observations and Data analysis

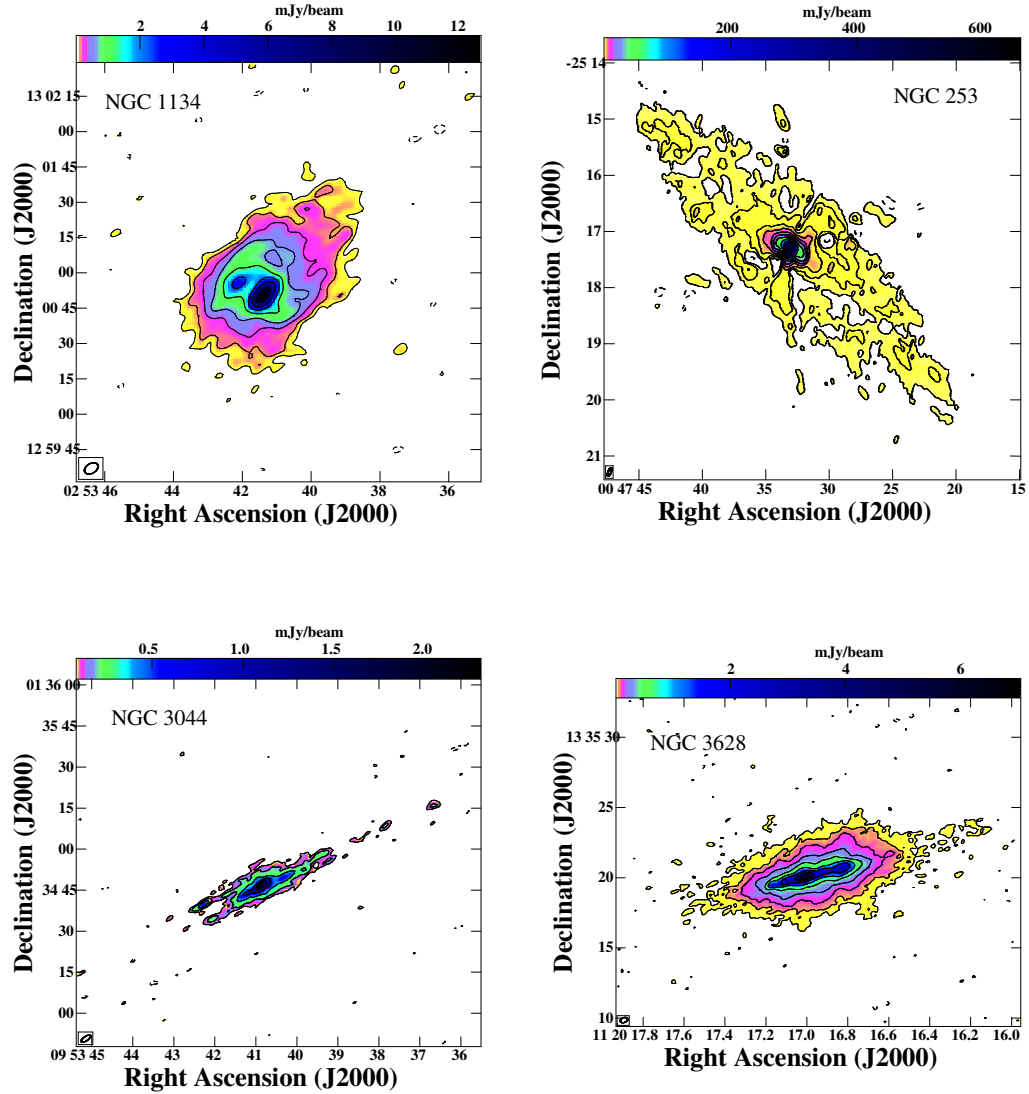


Figure 4.2: Total intensity images of starburst galaxies. The contour levels used are $3\sigma \times (-2, -1, 1, 2, 4, 8, 16, 32, \dots)$, where $\sigma = 24.61, 205.06, 30.076, 9.60 \mu\text{Jy beam}^{-1}$ for NGC 1134 at 1.5 GHz (top left), NGC 253 at 1.5 GHz (top right), NGC 3044 at 5.5 GHz (bottom left), NGC 3628 at 5.5 GHz (bottom right) respectively.

4. THE SEYFERT AND THE STARBURST GALAXY SAMPLE

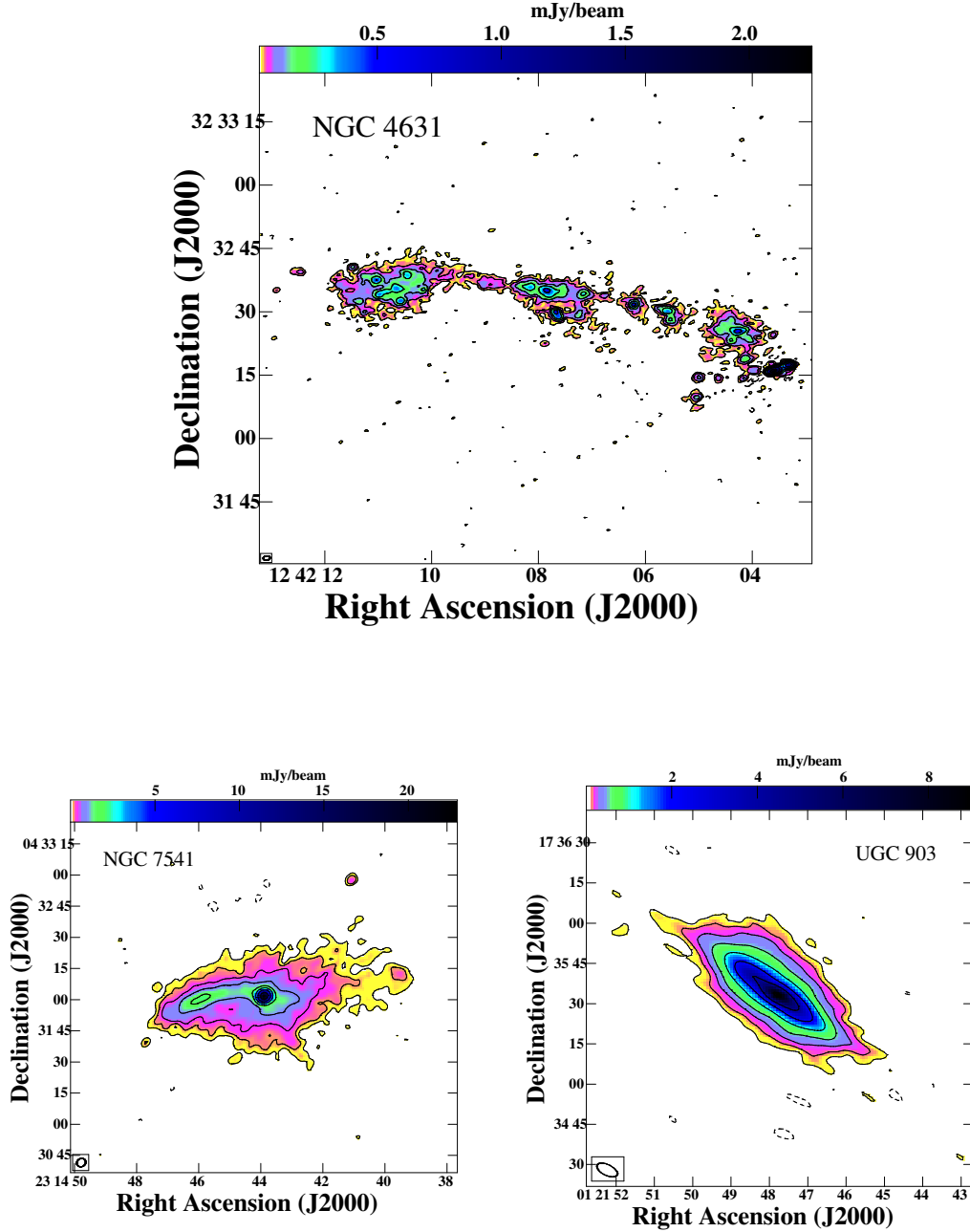


Figure 4.2: Continued—Total intensity images of starburst galaxies. The contour levels used are $3\sigma \times (-2, -1, 1, 2, 4, 8, 16, 32, \dots)$, where $\sigma = 9.66, 39.68, 22.2 \mu\text{Jy beam}^{-1}$ for NGC 4631 at 5.5 GHz (top), NGC 7541 at 1.5 GHz (bottom left), UGC 903 at 1.5 GHz (bottom right) respectively.

used to calibrate the polarization angles. However, the polarization angle for 3C 48 can vary by 30° or more at ~ 1 GHz, resulting in a similar uncertainty in the EVPAs of the sources, which in our sample turned out to be a single galaxy, NGC 253.

The calibrated target source was then extracted out of the multi-source file using the task ‘SPLIT’ in **CASA**. A few loops of imaging followed by phase-only self-calibration of the target source were carried out before one final round of amplitude and phase self-calibration. We used the **MT-MFS** algorithm while imaging, to correct for errors introduced due to the varied spectral indices of the sources in the field. We finally created the Stokes ‘Q’ and ‘U’ images, and the polarized intensity and polarization angle images from the former.

We then created polarization intensity images that were corrected for Ricean bias, polarization angle images, and fractional polarization images for each of our targets using the task ‘COMB’ in **AIPS**. While making the polarization angle images we blanked those pixels which had errors greater than 10° . Similarly while making the fractional polarization images, all the pixels which had errors greater than 10% of the fractional polarization values were blanked.

For the sources observed at 1.5 GHz, we also carried out rotation measure (RM) synthesis¹ to account for bandwidth depolarization. Data were acquired in 10 spectral windows (spws) for sources observed at 1.5 GHz. Separate full Stokes images were made at every spws on which RM synthesis was carried out. The results of our analysis are presented in Section 4.4.2.

4.4 Results

4.4.1 Radio Morphology

The total intensity images of Seyfert galaxies and starburst galaxies in our sample are presented in Figures 4.1 and 4.2, respectively. The radio morphologies of all the individual sources are discussed in the following sub-sections.

¹<https://github.com/mrbell/pyrmsynth>

4. THE SEYFERT AND THE STARBURST GALAXY SAMPLE

4.4.1.1 NGC 2639

Martini et al. (2003) classified NGC 2639 as a grand-design spiral galaxy hosting a Seyfert 1.9 nucleus. Our VLA observations revealed an extra pair of lobes in the north-south direction which appeared to be highly polarized and misaligned by almost 90° from the already identified pair of lobes (Sebastian et al., 2019a). Our observations favor a scenario where the secondary lobes are generated as a result of stopping and restarting of AGN activity.

4.4.1.2 NGC 2992

This Seyfert galaxy is a changing-look AGN that varies from type 2 to intermediate type sometimes accompanied by extreme X-ray activity and back over the span of a few years (Gilli et al., 2000; Ramos Almeida et al., 2009). By studying the X-ray variability in NGC 2992, Marinucci et al. (2020) have shown that the region showing X-ray flaring is as close as $\sim 15 - 40 r_g$ in two cases and $> 50 r_g$ to the supermassive black hole. Allen et al. (1999) found that NGC 2992 shows biconical outflows seen in [O III] and H α +N[II] on kilo-parsec scales and Veilleux et al. (2001) argue that this outflow is powered by the AGN rather than the starburst. Radio continuum emission shows a bright core and a pair of lobes with 8-shaped superbubble-like morphology with linear extents ~ 500 pc (Wehrle & Morris, 1988). Irwin et al. (2017) discovered an additional pair of lobes that are aligned along the minor axis of the host galaxy. This emission was disentangled from that of the disk emission using the high fractional polarization seen in the lobes.

4.4.1.3 NGC 3079

NGC 3079 is another Seyfert galaxy with a type 2 nucleus (Véron-Cetty & Véron, 2006) that shows loop-like radio lobes. NGC 3079 also hosts a central starburst rendering the delineation of the role played by starburst or AGN in the observed radio morphology difficult. Our high-resolution image resolves the “ring”-like lobes into filamentary structures. We carried out a detailed study of NGC 3079 and we conclude that the lobe morphology is a result of the central jet, the superwinds, and the galactic magnetic fields (Sebastian et al., 2019b).

4.4.1.4 NGC 3516

NGC 3516 is a Seyfert 1.5 galaxy (Knapen et al., 2002) hosted by an S0 type galaxy (Perez Garcia et al., 1998). H α and [O III] emission line imaging (Miyaji et al., 1992; Pogge, 1989) have shown elongated features which are aligned with the radio structures (Miyaji et al., 1992; Wrobel & Heeschen, 1988). Our radio intensity maps also show a bipolar diffuse feature similar to what is reported in the literature. Our image also shows a knot close to the nucleus in the northern direction, which coincides with a knot in the [O III] emission. Although the northernmost feature appears diffuse, it appears brighter compared to the region in between. It resembles a hotspot-like feature often seen in the jets of FR II radio galaxies.

4.4.1.5 NGC 4051

NGC 4051 has a Seyfert 1.2 type nuclei (Ho et al., 1997) and is hosted by a SAB type galaxy (Dumas et al., 2007). NGC 4051 has also been classified as a NLS1 galaxy in the literature (Denney et al., 2009; Yang et al., 2013). Christopoulou et al. (1997) using their MERLIN images find a triple source aligned at a PA of 73°. They also suggest the presence of conical outflows due to the presence of blueshifted components in the [O III] emission line profile. We find radio emission which is aligned along the NE direction similar to that found by Kukula et al. (1995). High resolution VLA observations of Berton et al. (2018) show the S-symmetry of the extended emission clearly. Christopoulou et al. (1997) find that the [OIII]emission is aligned along the NE direction coinciding with the emission seen at 8.4 GHz.

4.4.1.6 NGC 4235

NGC 4235 is a nearly edge-on, SAa type galaxy (Perez Garcia et al., 1998) with a Seyfert type 1 nucleus (Jiménez-Benito et al., 2000; Weedman, 1978) with high [O III] to H β line ratios at the core. NGC 4235 hosts a bright compact X-ray source (Fabbiano et al., 1992), whereas Rossa & Dettmar (2003) find a bright nucleus and an extended emission feature in H α images. Falcón-Barroso et al.

4. THE SEYFERT AND THE STARBURST GALAXY SAMPLE

(2006) and Pogge (1989) also find extended [O III] emission along the major axis, whereas no minor axis extension is detected (Colbert et al., 1996a).

However, the imaging study carried out by Colbert et al. (1996b) at 6 cm using the C-array configuration of VLA reveals an extraplanar bubble-like structure which extends up to 9 kpcs along with the compact core emission. The radio source appears unresolved in VLBA imaging, while it shows evidence for variability in flux density in the VLA images (Anderson & Ulvestad, 2005). The imaging study carried out by Hummel & Saikia (1991) also does not show any extended emission. The GMRT images at 325 and 610 MHz presented by Kharb et al. (2016) suggest the presence of relic lobe emission.

4.4.1.7 NGC 4593

NGC 4593 has a Seyfert type 1 nucleus (George et al., 1998) hosted by an SBb galaxy (González Delgado et al., 1997). The radio emission appears point-like in our image as well as many of the past high angular resolution studies like those by Schmitt et al. (2001); Thean et al. (2000); Ulvestad & Wilson (1984a). We do not detect the faint double lobes seen by Gallimore et al. (2006) in their lower resolution images. It was noted by Gallimore et al. (2006) that this kpc scaled emission is aligned along the [O III] emission (Schmitt et al., 2003).

4.4.1.8 NGC 4388

NGC 4388 is also a highly inclined galaxy hosting a Seyfert type 2 nucleus (Phillips & Malin, 1982). X-ray studies of NGC 4388 show the presence of an ample amount of extended soft X-ray emission, which is generated as a result of photoionization by the nuclear activity (Beckmann et al., 2004; Cappi et al., 2006; Iwasawa et al., 2003; Risaliti et al., 2002). Ionized gas studies also show similar extended features, for instance, Pogge (1988) find a conical shaped ionized region.

NGC 4388 is well studied in radio wavelengths, all of which show a double source slightly away from the center of the galaxy (Condon et al., 1987; Hummel & Saikia, 1991; Irwin et al., 2000; Stone et al., 1988). More recently, Damas-Segovia et al. (2016) studied NGC 4388 in great detail as a part of the CHANG-ES survey using the EVLA in C-band. They find that the radio emission from

the outflow is very well correlated with the H α and X-ray emission and extends up to 5 kpc in size. They also detected the southern counterpart of the outflow for the first time using their deep observations.

4.4.1.9 NGC 5506

NGC 5506 is hosted by an irregular edge-on spiral galaxy. Originally classified as a Seyfert type 2 nucleus (Wilson et al., 1976), it was later identified by Nagar et al. (2002) as a NLS1. Based on emission-line ratios, Maiolino et al. (1994) and Davies et al. (2005) argue that there is active star formation occurring on 250 – 400 parsec scales. Maiolino et al. (1994) also found evidence for double-peaked emission lines which were interpreted as the result of a biconical outflow. The extended soft X-ray emission as observed by (Colbert et al., 1998) is aligned in a direction similar to that the emission-line outflow traced and is also coincident with the radio emission. The IFU images produced by the WiFeS instrument on the ANU 2.3 m telescope also shows biconical outflows in the same direction (Thomas et al., 2017).

4.4.1.10 NGC 1134

NGC 1134 was classified as a starburst source based on their radio to FIR flux, the flux at 25 μm to 60 μm , and also due to the lack of any diffuse extended structures in radio images. Our image also shows radio continuum emission superposing the optical emission from the disk.

4.4.1.11 NGC 253

It is a nuclear starburst galaxy, which has star formation activity going on in the inner 200 pc radius (Engelbracht et al., 1998). NGC 253 has a bright central point source in radio coinciding with a faint NIR source (Sams et al., 1994) and a hard X-ray source (Weaver et al., 2002) and hence many authors classify the source as an LLAGN (Lira et al., 2007; Mohan et al., 2002). NGC 253 was classified as a LINER galaxy, although it is suggested that the optical line characteristics can be explained as a result of starburst (Engelbracht et al., 1998). McCarthy et al. (1987) identified a shocked bubble in emission-line gas, suggesting outflows.

4. THE SEYFERT AND THE STARBURST GALAXY SAMPLE

Diffuse X-ray emitting gas studies also present evidence for biconical outflows in this galaxy (Dahlem et al., 1998; Förster Schreiber et al., 2004). Carilli et al. (1992) discovered the radio continuum halo that extended up to 4 kpc in size from the disk.

4.4.1.12 NGC 3044

NGC 3044 is an edge-on galaxy that is classified as an SB (s) type galaxy (Miller & Veilleux, 2003). Narrowband image of H α +[N II] shows diffuse emission to both sides of the galaxy probably arising from an expanding superbubble (Miller & Veilleux, 2003). Collins et al. (2000) find that the H α and radio continuum emission possess very similar extents and structure. The VLA observations at 20 cm by Irwin et al. (2000) show a loop in the radio continuum to the northwest of the nucleus which we do not find in our images likely owing to the steep spectrum of these features.

4.4.1.13 NGC 3628

NGC 3628 is a Sb spiral galaxy which has a starburst nucleus and a prominent dust lane (Liu & Bregman, 2005). NGC 3628 hosts a LINER nuclei and González-Martín et al. (2006) classify it as an AGN from the spectral fitting of the X-ray data, whereas Flohic et al. (2006) suggested that the LINER emission in NGC 3628 is starburst-related rather than AGN related due to the absence of an X-ray point source at the center of the galaxy. Spectral index study of this source reveals double lobed structure (see Figure 4 in Irwin et al., 2019b). In our image, we see radio emission overlapping features in the optical image with finger-like protrusions at several locations across the disk.

4.4.1.14 NGC 4631

NGC 4631 is an edge-on spiral galaxy with a highly polarized radio continuum halo with a half-intensity height of about 14 kpc (Ekers & Sancisi, 1977). The polarized emission which is X-shaped is mostly extraplanar and the disk is depolarized. The magnetic field structure of the polarized emission is directed radially

outwards either indicating the role of outflowing material or the large-scale galactic dynamo or both (Golla & Hummel, 1994). Our 5.5 GHz observations did not have the uv-coverage to recover the diffuse extraplanar emission and the image of NGC 4631 mostly shows the detailed structure of the radio emission in the disk. Dahlem et al. (1995) show that the extent of the radio emission is similar to the diffuse X-ray emission seen in NGC 4631. Strickland et al. (2004) argue that the absence of a complete spatial correlation between the X-ray and the radio emission implies that the relativistic electron population, the magnetic fields, and the hot plasma are decoupled from each other. Detailed study of this source was carried out using EVLA observations in C-band with C and D-arrays and L-band with B, C, and D array configurations (Mora-Partiarroyo et al., 2019a,b). They detect semi-periodic field-reversals using their RM images in the northern halo of NGC 4631 for the first time using their deep observations.

4.4.1.15 NGC 7541

NGC 7541 is an SB type nearly edge-on spiral galaxy. Our radio image at 1.5 GHz shows the spiral arms to the east very clearly. While we do not detect any continuum halo-like emission, we detect diffuse radio emission overlapping with the star-forming disk. Colbert et al. (1996b) detect finger-like structures protruding from the disk, which is seen in our images as well.

4.4.1.16 UGC 903

Colbert et al. (1996b) in their radio study of UGC 903 at 5 GHz find that most of the radio emission have their origin from the disk. They also find that faint finger-like structures that extend out of the disk.

4.4.2 Polarization Properties

We detected polarization in four Seyfert galaxies (NGC 2639, NGC 3079, NGC 4388 and NGC 5506) at 5.5 GHz and one starburst (NGC 253) at 1.5 GHz. We did not detect polarization in many of our sources, probably due to a variety of reasons including depolarization, sensitivity limitations, and inadequacy of

4. THE SEYFERT AND THE STARBURST GALAXY SAMPLE

Table 4.2: Upper limit on fractional polarization

Source	Limit on brightest feature (%)	Limit on diffuse feature (%)
	$3 \times \frac{('Q'rms)}{('I'peak)}$	$3 \times \frac{('Q'rms)}{(typical 'I')}$
NGC2992	0.24	8.67
NGC3044	3.46	10.13
NGC3516	0.82	38.77
NGC3628	0.38	3.61
NGC4051	1.7	14.31
NGC4235	0.51	4.73
NGC4593	12.78	—
NGC4631	4.48	25.04
NGC7541	0.31	3.28
UGC903	0.59	3.55

Column 1: Target names. Column 2: the upper limit on the fractional polarization calculated using the peak from the total intensity image. Column 3: the upper limit on the fractional polarization calculated using the mean value of typical low surface brightness diffuse region from the total intensity image. NGC 4593 is a point source and hence column 3 is left blank.

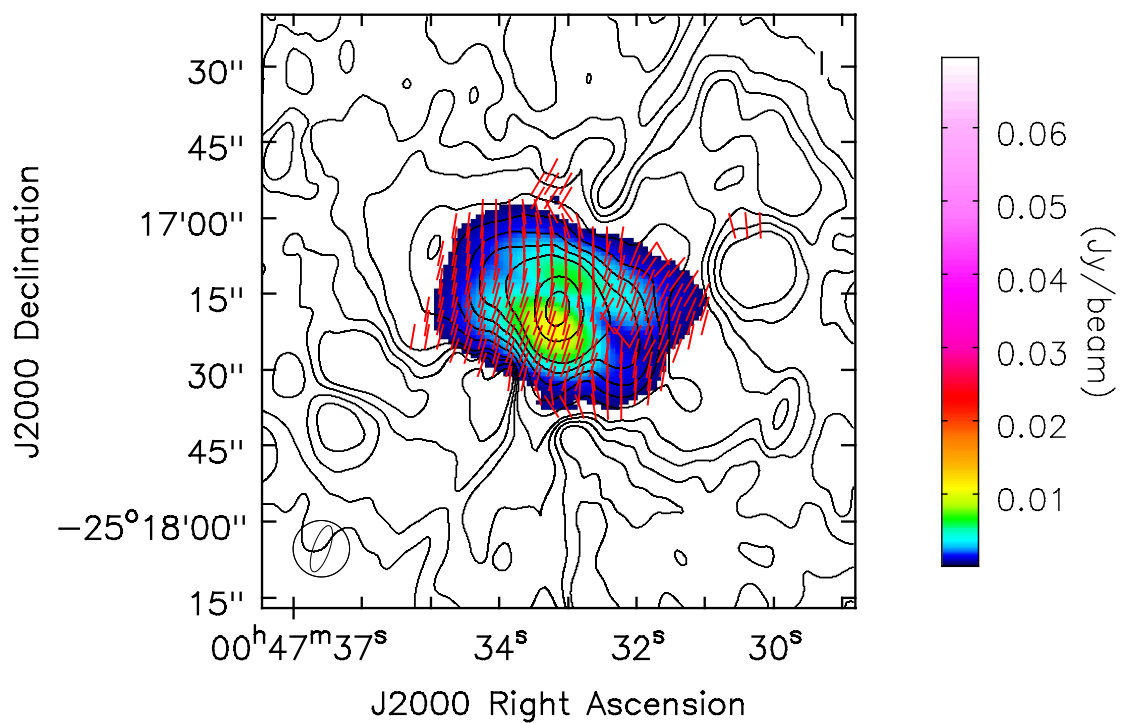


Figure 4.3: Zoomed-in polarization image of NGC 253: Polarization electric vectors in red overlaid on color image of the polarized intensity and total intensity contours for NGC 253 with contour levels = $0.48 \times (1, 2, 4, 8, 16, 32, 64, 128, 256, 512)$ mJy beam $^{-1}$. The polarization intensity and polarization angle images were produced using RM synthesis.

4. THE SEYFERT AND THE STARBURST GALAXY SAMPLE

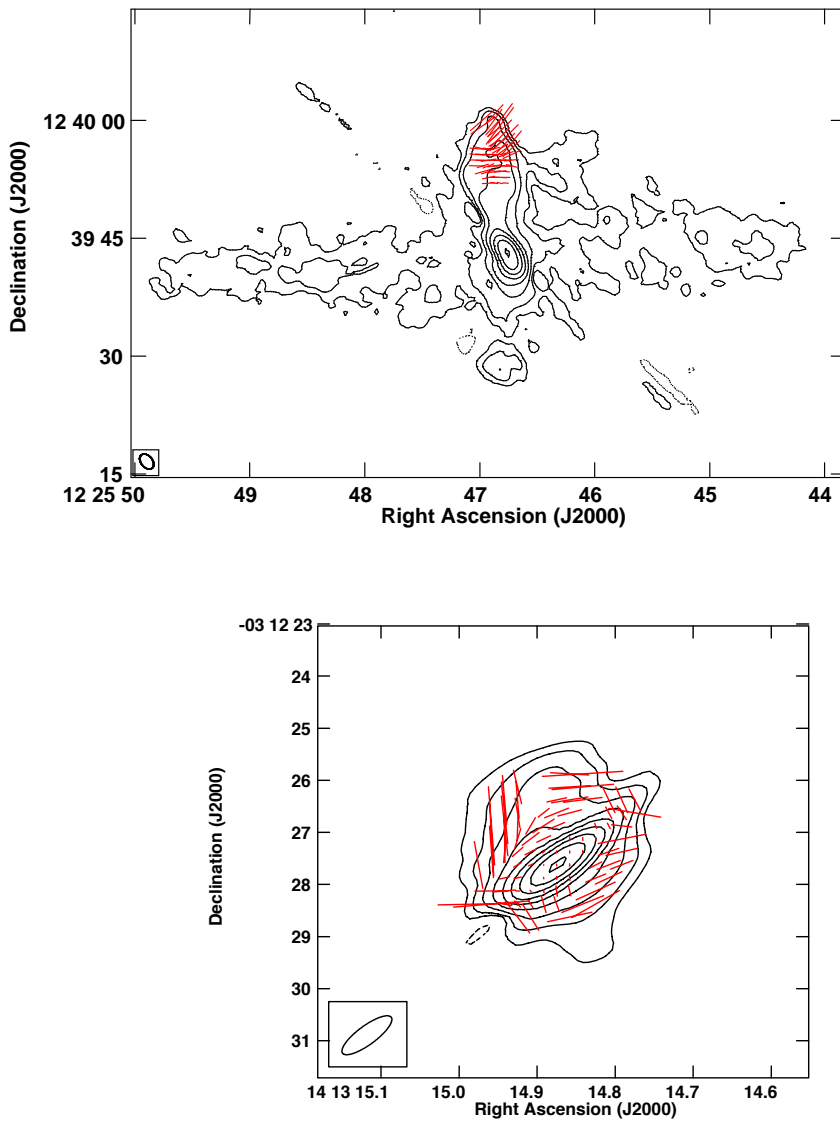


Figure 4.4: Polarization electric vectors with length proportional to fractional polarization in red overlaid on total intensity contours for (top) NGC 4388 at 5.5 GHz with contour levels = $0.13 \times (-2, -1, 1, 2, 4, 8, 16, 32, 64, 128, 256, 512)$ mJy beam $^{-1}$, with one arcsec length of the polarization vector corresponding to 6.8% fractional polarization and (bottom) NGC 5506 at 5.5 GHz with contour levels = $1.17 \times (-0.350, 0.350, 0.700, 1.400, 2.800, 5.600, 11.30, 22.50, 45, 90)$ mJy beam $^{-1}$ with one arcsec length of the polarization vector corresponding to 6.7% fractional polarization.

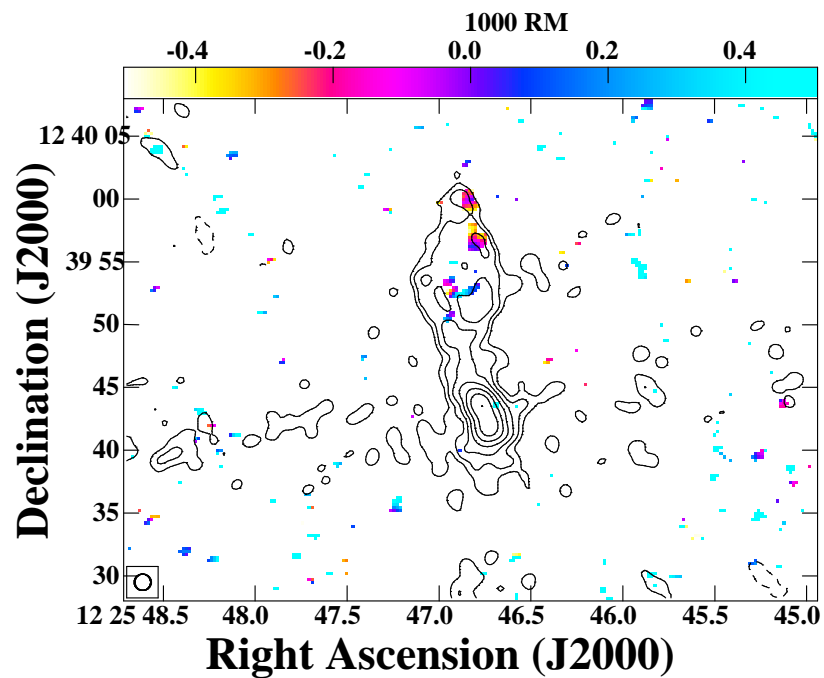


Figure 4.5: The 5 GHz total intensity radio contours superimposed over the in-band rotation measure image of NGC 4388 in color. Contour levels: $213 \times (-2, -1, 1, 2, 4, 8, 16, 32, 64, 128, 256, 512) \mu\text{Jy beam}^{-1}$. The beam shown in the lower left corner is of size $1.3'' \times 1.30''$. The RM values are in units 1000 rad m^{-2} .

4. THE SEYFERT AND THE STARBURST GALAXY SAMPLE

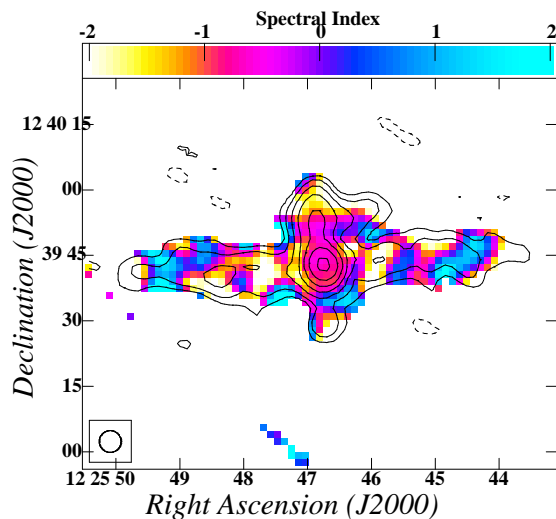


Figure 4.6: The in-band spectral index image of NGC 4388 in color with 5 GHz radio contours superimposed. Contour levels: $5 \times 10^{-4} \times (1, 2, 4, 8, 16, 32, 64, 128, 256, 512)$ Jy beam $^{-1}$. The circular beam shown in the lower left corner is of size $\sim 5''$.

4.4 Results

short baselines to map the diffuse polarized emission. Especially at 1.4 GHz, the wavelength dependant depolarization effects may be playing a significant role.

To recover polarized emission which may have been lost due to bandwidth depolarization in the process of imaging, we attempted using rotation measure (RM) synthesis (Brentjens & de Bruyn, 2005) for our starburst galaxies observed at 1.4 GHz. We detected marginal levels of polarization in NGC 1134, and UGC 903 which were undetected previously. The mean fractional polarization estimated from regions that showed polarization signal above three sigma threshold turned out to be in the range $\sim 1 - 4\%$ for NGC 1134, NGC 253 and UGC 903. Because of such low levels of polarization along with the lack of organization in the polarization angles, the fidelity of the polarized emission recovered using RM synthesis needs to be confirmed using future observations. The polarization image of NGC 253 is presented in Figure 4.3. The polarization vectors were obtained using the relation, $\frac{1}{2} \tan^{-1}(\frac{U}{Q})$. We note that the polarization angle calibrator 3C48 used for this dataset is only 0.5% polarised at 1.5 GHz¹. Therefore the polarization angles could in principle have large errors. In our study, the starburst galaxy NGC 253 shows polarized emission near the core with typical mean fractional polarization $\sim 4\%$. It is worth noting here that NGC 253 has been suggested to possess a weak LINER-like AGN in its center.

Therefore, we detect polarized emission in 4/9 ($\sim 44\%$) of Seyfert galaxies at 5.5 GHz, 3/4 (75%) of starburst galaxies observed at 1.4 GHz and 0/3 starburst galaxies at 5.5 GHz. A direct one-to-one comparison between the fractional polarization in the starburst galaxies at 1.4 GHz and Seyfert galaxies is limited because of the difference in frequencies and resolution. The starburst galaxies might be facing more bandwidth and beam depolarization with the additional complication of picking up more diffuse emission.

Despite the lower frequency of observation, the detection rate is higher for starburst galaxies at 1.4 GHz, which, if real, would imply that the ordering scales of polarized emission in starburst galaxies is larger and is preferably picked up by the lower resolution observations at 1.4 GHz. Such a situation is expected when the magnetic fields are ordered due to the large-scale mean-field dynamo mechanism operating on the scales similar to the structures of the galaxy itself. On

¹<https://science.nrao.edu/facilities/vla/docs/manuals/obsguide/modes/pol>

4. THE SEYFERT AND THE STARBURST GALAXY SAMPLE

the other hand, the radio emission which owes its origin to the jets at resolutions higher than the galaxy size scales is easily explicable. Owing to the small sample size and the fact that only four starburst galaxies were observed at 1.4 GHz and three at 5.5 GHz, our results must be treated as indicative pending additional data.

The upper limits on the fractional polarization of our sources calculated using the rms noise of the Stokes 'Q' images are tabulated in Table 4.2. The lobes of NGC 2639 and NGC 3079 show polarization fractions as high as 30% at 5.5 GHz (Sebastian et al., 2019a,b). While it is true that our observations suggest that Seyfert galaxies are more probable to show polarized emission at the given frequency (~ 5 GHz) and resolution ($\sim 1''$), this is not a universal trend. For example, we did not detect polarization in NGC 2992 with an upper limit of 8.7% on the most diffuse feature. Irwin et al. (2017) find an average fractional polarization of 6.4% for NGC 2992 observed at C-band using the C and D arrays. On the other hand, none of the starburst galaxies have polarization fractions above 25% even in the most diffuse features at either of the frequencies.

Figure 4.4 shows the polarization images of NGC 4388 and NGC 5506. The northern lobe of NGC 4388 shows polarized emission towards the northern edge. There appears to be two distinct polarized regions, one within the lobes and one along the north-western edge. The fractional polarization in the northwestern edge and that within the inner regions of the lobes turn out to be $24 \pm 4.5\%$ and $13 \pm 3\%$. The inner regions of the northern lobe show electric vectors aligned perpendicular to the axis implying magnetic field vectors that are aligned along the jet axis. More interesting is the alignment of the electric vectors at the north-western edge of the lobe. The electric field vectors are aligned perpendicular to the edge, implying tangential magnetic fields.

The high levels of fractional polarization along with the tangential alignment of magnetic fields and the tightening of contours are expected if shock compression is leading to the amplification of magnetic fields at the edges. Yet another interesting morphological detail is the diffuse extension towards the west which is present only after the end of the highly polarized feature in the north-west. Damas-Segovia et al. (2016) presented the lower-resolution polarization images of NGC 4388 from observation carried out using C and D array configuration at

4.4 Results

6.0 GHz. They recover much more diffuse polarized emission which extends up to 5 kpc. Their images mostly show poloidal magnetic fields similar to those seen in the inner regions of the lobes in our image. Figure 4.5 shows the RM image of NGC 4388 with radio total intensity contours overlaid. The RM values show gradients in two regions along the north-western edge of the northern lobe, and even an RM inversion in the region at declination $12^{\circ} 39' 55''$. Interestingly, such RM gradients have been inferred to suggest the presence of helical magnetic fields (e.g., Clausen-Brown et al., 2011; Kharb et al., 2009). Clearly, the magnetic field structure in the lobes of NGC 4388 is complex.

Figure 4.6 shows the spectral index image of NGC 4388 generated by dividing the data into four sub-bands and using the beginning and end frequency sub-band images. We have uv-tapered the data to achieve a coarse resolution of $\sim 5''$ to discern the variation of the spectral index across the lobes .

We do not find an obvious correlation between the implied magnetic field compression at the lobe edge in NGC 4388 and the in-band spectral index values, in that there is no clear spectral flattening at the lobe edge . Such spectral flattening has been observed in the lobes of the Seyfert 1 galaxy Mrk 231 by Ulvestad et al. (1999) and Seyfert 2 galaxy NGC 3079 by Sebastian et al. (2019b) and could be consistent with magnetic field compression as well as re-acceleration of charged particles at the lobe edges, where the lobes interact with the surrounding medium.

The outflow-like radio emission observed in NGC 5506 is also polarized with a complex morphology for the polarization electric vectors. The inferred magnetic field vectors appear to follow the outflow. The fractional polarization has an average value of 7.5% which increases towards the edge of the outflow. The radio emission does not show clear edges like those observed in NGC 3079 or NGC 4388. Shock acceleration, therefore, might not be the primary source for the polarized emission in this source.

Amongst several of the studies which explored the radio continuum emission from Seyfert galaxies, a few involved understanding their polarization properties. Ho & Ulvestad (2001) detected polarized emission from 12 out of the 52 sources that they observed. Several other detailed polarization studies of individual Seyfert sources include Crane & van der Hulst (1992); Duric & Seaquist

4. THE SEYFERT AND THE STARBURST GALAXY SAMPLE

(1988); Elmouttie et al. (1998); Kaufman et al. (1996); Kharb et al. (2006); Wilson & Ulvestad (1983). Several studies have noted a difference in the magnetic field structures inside parsec-scale jets of various AGN sub-classes like low-energy peaked BL Lacs (LBLs) and high-energy peaked BL Lacs (HBLs) with LBLs predominantly showing transverse inferred magnetic fields and HBLs showing longitudinal inferred magnetic fields, similar to those observed in quasars (Cawthorne et al., 1993; Gabuzda et al., 1992; Kharb et al., 2008). We inspected the images of the Seyfert galaxies published in the literature in conjunction with ours. In nearly seven out of ten sources with well-resolved polarized radio emission, the inferred magnetic field vectors are aligned with the lobe edges. In four of these sources the inferred magnetic field is largely poloidal along the outflow direction, while in most other sources, it is hard to attribute a uniform trend for the polarization vectors in the lobe. In the remaining sources, the inferred magnetic field orientation is neither parallel nor perpendicular to the outflows.

The CHANG-ES survey (Irwin et al., 2012) has obtained polarization data on a large number of nearby spiral galaxies. Krause et al. (2020) find that the fractional polarization values observed in spiral galaxies range from 10 to 40% when imaged at a resolution of $12''$. These high degrees of polarization are in contrast to the negligible values seen in our observations at higher resolutions. Krause et al. (2020) also noted that increased fractional polarization comes from large-scale diffuse emission from galactic haloes on scales larger than 1 kpc or several kpc. We conclude that the fractional polarization is higher in the lobes of Seyfert galaxies in high-resolution observations compared to starburst galaxies, although more polarization data are needed to confirm this result.

4.5 Discussion

The radio total intensity contours overlaid on the optical images are shown in Figures 4.7. It can be noticed that the radio continuum emission in starburst galaxies mostly follows the optical disk star formation regions, whereas the Seyfert galaxies most often show either lobe-like features without any corresponding optical features or nuclear core-dominated emission along with emission from the star-forming disk. The diffuse lobe-like structures in Seyfert galaxies are very different

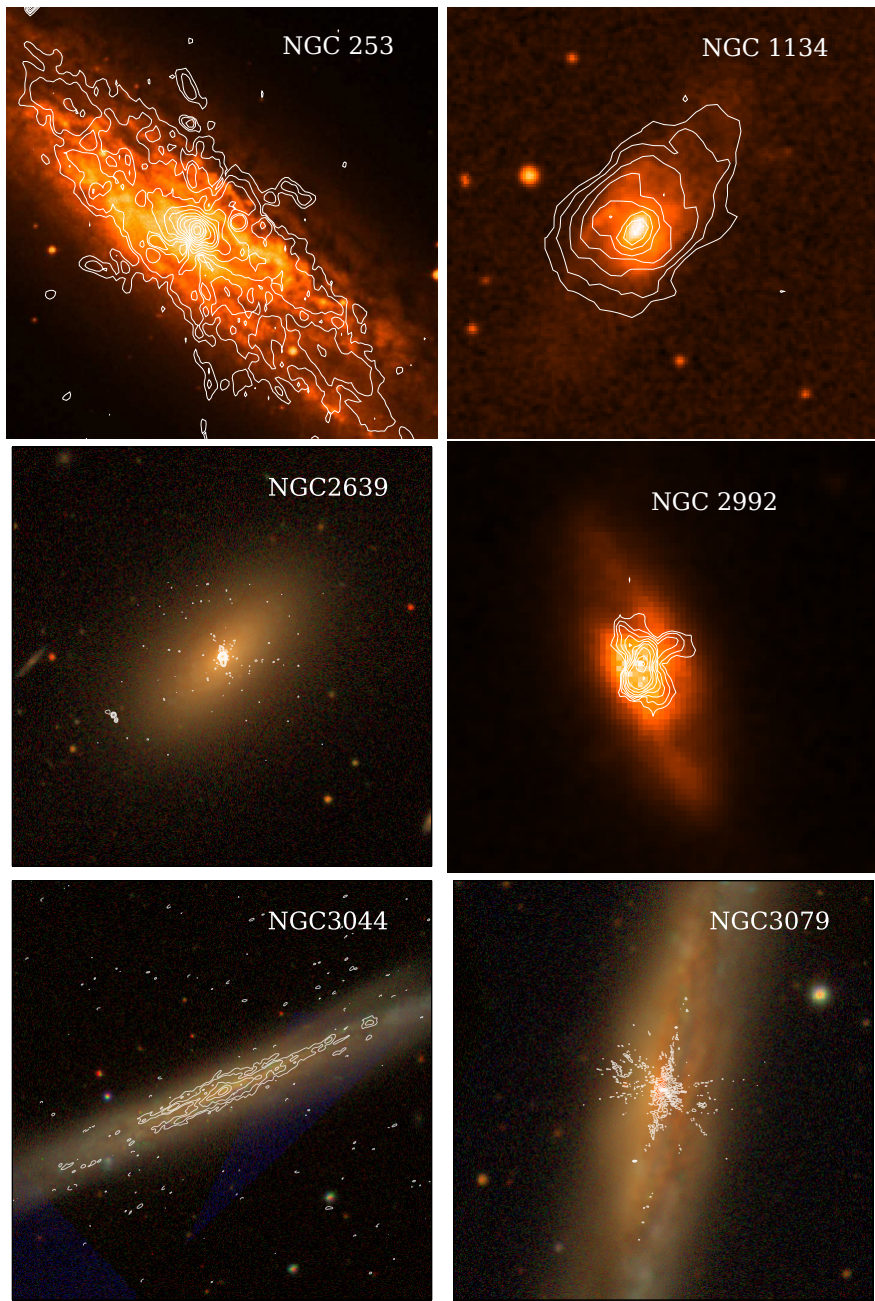


Figure 4.7: Radio total intensity emission overlaid in white contours over the optical color composite images. The optical images are taken from various optical surveys namely, DECaLS, MzLS, SDSS and DSS depending on the availability of data in these surveys. We have used only the DSS r-band image to make the overlays of NGC 253, NGC 1134 and NGC 2992 due to the poor quality of the color composite image.

4. THE SEYFERT AND THE STARBURST GALAXY SAMPLE

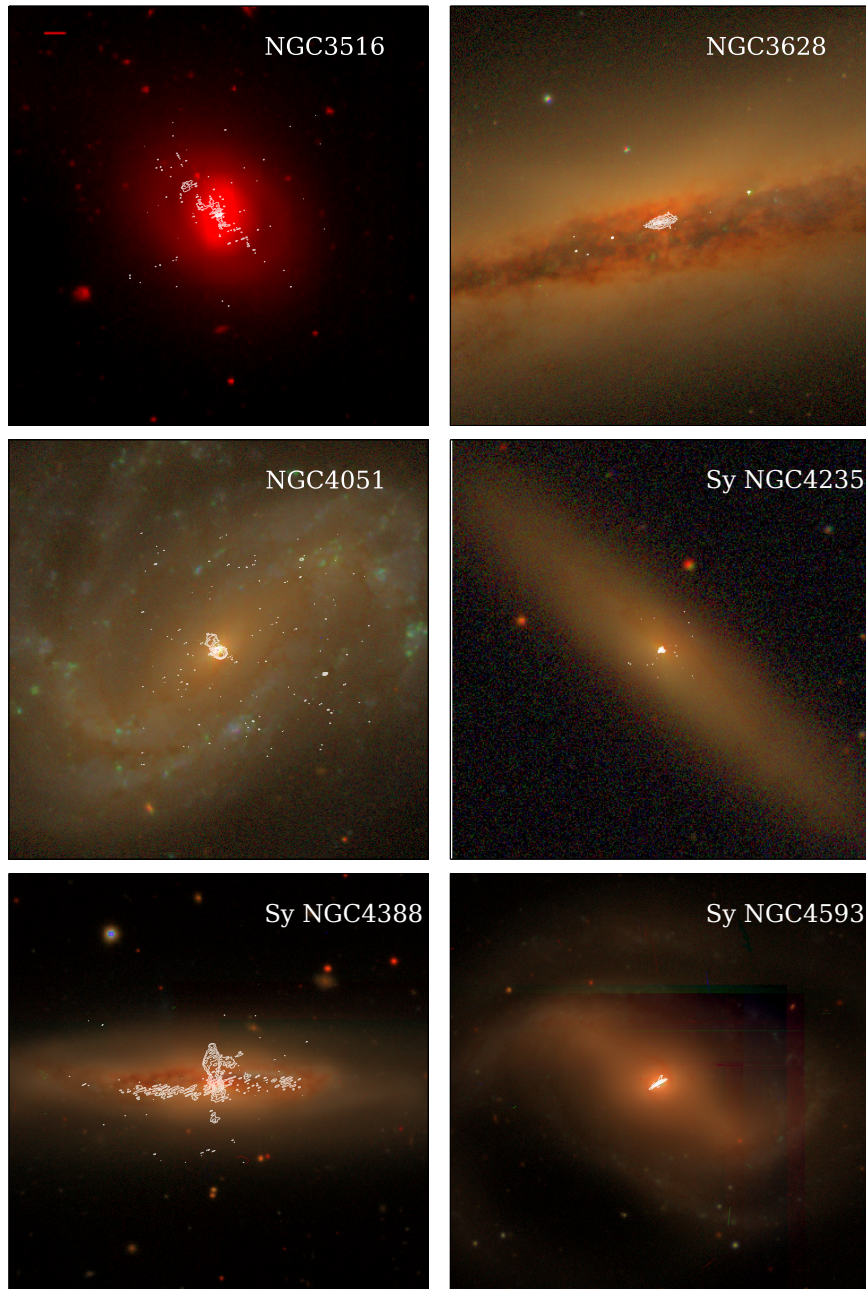


Figure 4.7: Continued–Radio total intensity emission overlaid in white contours over the optical color composite images.

4.5 Discussion

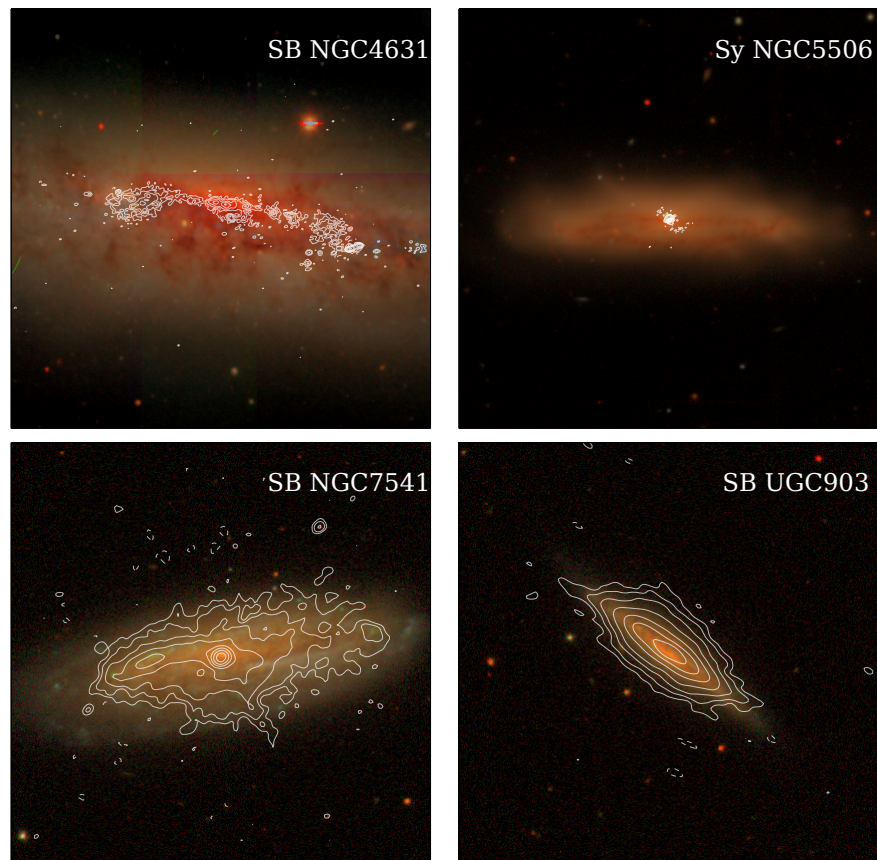


Figure 4.7: Continued—Radio total intensity emission overlaid in white contours over the optical color composite images.

4. THE SEYFERT AND THE STARBURST GALAXY SAMPLE

in morphology from those seen in both FR I, and FR II radio-galaxies. NGC 2639, NGC 2992, NGC 3079, NGC 4051, and NGC 4388 show lobe-like structures with a pinched in morphology near the AGN core. Most of them appear brighter at the farthest edges and sometimes show S-shaped symmetry like in the case of NGC 4051 and NGC 3079. NGC 3516 also shows S-symmetry although, the morphology appears somewhat intermediate between bulbous shaped lobes of a Seyfert galaxy and an FR II type radio galaxy showing hotspot and lobes.

On the other hand, most cases of galaxies dominated by star-formation show top open bi-conical outflow like morphology rather than a dome-shaped appearance. For example prototypical starburst galaxies like NGC 253 (Heesen et al., 2011) and M 82 (Adebahr et al., 2013) show bi-conical radio emission which is spatially aligned and correlated with X-ray and optical line emission. Such correlated emission was explained to be a result of the entrainment of the cosmic ray electron population from the galactic disk and the frozen-in magnetic fields along with the outflows which are traced using X-ray or emission-line gas (Adebahr et al., 2013; Cecil et al., 2001; Suchkov et al., 1994, 1996). Krause et al. (2020) through a stacking analysis find that the linear polarization in star-forming galaxies is X-shaped in morphology. This X-shaped morphology has been attributed to an interplay of the galactic outflows and the dynamo action of the host galaxy itself.

An attractive possibility to explain the bulbous-shaped morphology is to invoke the dynamical influence that the galaxy may have in the evolution of the Seyfert jets. A simple hydrodynamical model would favor a frustrated jet model, according to which the intrinsically low-power jets gets disrupted by the dense ISM percolating these late-type galaxies, and expands into the ambient medium along the minor axis, which offers the least resistance (Gallimore et al., 2006). However, such a model is rendered insufficient to explain the closed dome-like morphology, for which the large-scale magnetic fields that thread the galaxy was invoked (Henriksen, 2019; Sebastian et al., 2019b), because some of the solutions of a force-free magnetic field of the galaxy resemble the morphology of NGC 3079.

But even in this case, one would expect alignment along the minor axis. While this is true for some cases, like NGC 3079, NGC 4388, etc there are many where this is not the case, for example, NGC 2639 and NGC 3516. More importantly,

Seyfert galaxies like Mrk 6 which show this closed dome-type morphology in several directions misaligned with each other (Kharb et al., 2006) pose a problem for the simple picture of galactic magnetic fields being responsible for the dome-like structure.

Hence, we conclude that the peculiar dome-type morphology of the radio emission seen in Seyfert galaxies is linked to the active nucleus although the environmental influences might still be playing a role. The difference in the alignment itself can be produced as a result of multiple epochs of activity (Kharb et al., 2006; Sebastian et al., 2019b). In the following subsections, we try to understand the individual contributions from the AGN accretion, jet, and the star formation to the kpc-scaled radio emission.

4.5.1 Correlation between star-formation and radio emission

The radio-FIR correlation is one of the tightest astrophysical correlations known (Condon, 1992). It is proposed that the radio emission and the relativistic plasma seen in Seyfert galaxies arise due to mainly three reasons (i) jet-related, (ii) winds and the resulting in-situ acceleration of the thermal electrons to relativistic energies at shocks via diffusive shock acceleration (Blandford & Eichler, 1987) and/or (iii) star-formation-related. Any emission related to either of the former two reasons should show deviation in the form of a radio-excess from the radio-FIR correlation. It is however not clear if the shocks created due to winds like those by starburst galaxies/ AGN accretion are powerful enough to generate significant radio emission which is comparable to that generated by supernovae/ H II regions which result in the radio-FIR correlation. A simple observational test is to examine whether a radio excess is seen in starburst galaxies which show evidence for superwinds but do not host an AGN such that there is no contamination from jets.

In figure 4.8, we have plotted the radio luminosity at 1.4 GHz as a function of the far-infrared luminosity at $60\mu\text{m}$. We have also plotted the black line corresponding to the radio-FIR correlation as derived by Yun et al. (2001). We obtained the total radio flux densities from the NVSS images at 1.4 GHz, and the

4. THE SEYFERT AND THE STARBURST GALAXY SAMPLE

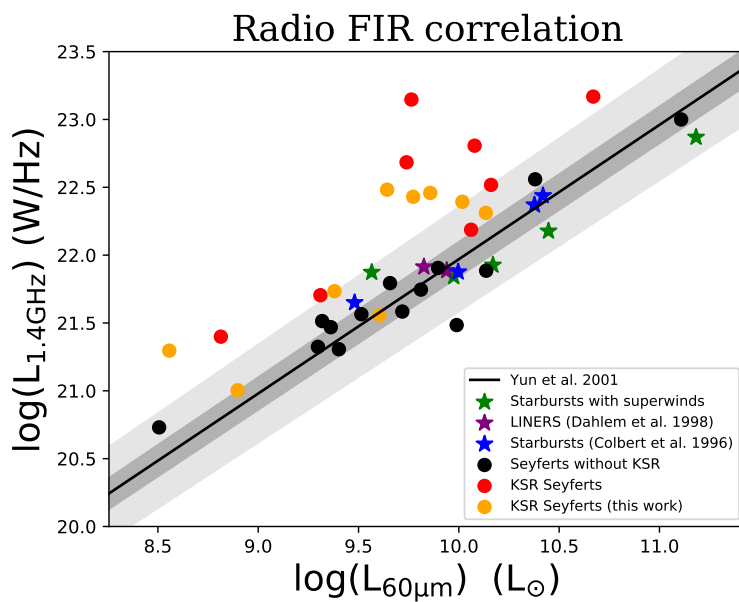


Figure 4.8: Plot of FIR luminosity at $60 \mu\text{m}$ vs the 1.4 GHz luminosity in W Hz^{-1} . The black line shows the radio-FIR correlation whereas the region shaded using dark grey and light grey represents the 1σ and 3σ boundary limits of the radio-FIR correlation from Yun et al. (2001).

4.5 Discussion

IR flux densities from the IRAS catalog (Fullmer & Lonsdale, 1989). The dark grey and the light grey shaded regions represent the 1σ and 3σ deviations from the radio-FIR correlation respectively (Yun et al., 2001). The dots represent the Seyfert galaxies, whereas the stars represent starburst galaxies. We increased the sample size of Seyfert galaxies by including more sources that showed radio flux densities above 10.0 mJy in NVSS from the sample presented in Gallimore et al. (2006). The red and black dots represent Seyfert galaxies that host KSR and that without much evidence for KSR respectively.

The starburst galaxies chosen from the Colbert et al. (1996b) represented by blue stars were chosen such that it matches the radio-luminosity of Seyfert galaxies in our sample. The three starburst galaxies from Dahlem et al. (1998) showed diffuse X-ray emission which was interpreted as evidence for superwinds. To increase the sample size of superwind-hosting starburst galaxies, we further chose four more superwind hosting galaxies from Heckman et al. (1990), which did not show any evidence for an AGN at its core, namely M82, NGC 4194, NGC 1222 and NGC 1614. The purple and green stars represent the starburst galaxies hosting superwinds taken from both Heckman et al. (1990) and Dahlem et al. (1998). However, the purple stars are the galaxies from Dahlem et al. (1998) which showed LINER nuclei, although the origin of this LINER emission is not indisputably AGN related (see Section 4.4.1.11 and 4.4.1.13). Moreover, they follow the radio-FIR correlation within 1σ error bar.

It is evident from figure 4.8 that most Seyfert galaxies with KSR show excess radio emission in comparison to the radio-FIR correlation, with 13/17 Seyfert galaxies having radio flux densities above the 3σ limits. However, most of the Seyfert galaxies without any KSR are consistent with the radio-FIR correlation. This was previously noted by Gallimore et al. (2006) as well. The starburst galaxies with superwinds are consistent with the radio-FIR correlation and often lies below the correlation. Hence, it is clear that shocks generated due to the supersonic velocities of the winds typically seen in these systems are not powerful enough to create radio emission comparable with that related to star-formation itself. Hence, any excess radio emission seen in Seyfert galaxies can be conclusively attributed to the jets or magnetically launched winds by an AGN present rather

4. THE SEYFERT AND THE STARBURST GALAXY SAMPLE

than radiatively/thermally driven winds that leads to radio emission via shock acceleration.

4.5.2 Investigating the correlation of radio emission with NLR properties

The correlation between the narrow line region and radio emission in Seyfert galaxies, in particular, that between the [O III] line luminosity, its FWHM, and the radio luminosity has been known for a while (Heckman et al., 1981; Whittle, 1985; Xu et al., 1999; de Bruyn & Wilson, 1978). These emission-line regions were found to be spatially aligned with the extended radio emission and sometimes surrounding the radio emission (Capetti et al., 1996; Falcke et al., 1998; Haniff et al., 1988). Extended emission-line regions were also found extending up to tens of kpc were found to be spatially associated with large scale radio emission in radio galaxies as well (Baum & Heckman, 1989; Fosbury, 1986). Moreover, such extended emission-line regions are more frequently found in steep spectrum sources rather than flat-spectrum sources. Leipski et al. (2006) found that the size of the radio sources in radio-quiet quasars correlates well with the size of the NLR. All these pieces of evidence are suggestive of a scenario where the material in the NLR is ionized as a result of shocks generated by the relativistic radio plasma interacting with the gas around it.

Several other studies preceded by Veilleux (1991a,b) also revealed a correlation between the narrow line region kinematics and the radio luminosity. In a recent study, Zakamska & Greene (2014) found that the [O III] line-width containing 90% of the emission line flux correlates well with the radio luminosity in these systems. The radio emission was interpreted to be a result of the shock acceleration that happens due to the supersonic velocities of the outflows driven by the accretion in these systems rather than a jet.

Seyfert galaxies, which are also mostly radio-quiet in nature, prove to be ideal candidates that can be studied in detail to test both these scenarios, namely the jet origin of the radio emission which then shock ionizes the medium or the radiation pressure driven wind origin which is responsible for both the radio

4.5 Discussion

emission via shocks and the NLR emission which constitutes the photo-ionized wind.

In this chapter, we study how the radio luminosity in our sample of Seyfert sources correlate with the [O III] line luminosity. We obtained the [O III] line luminosities of our Seyfert galaxies from the compilation presented in Malkan et al. (2017). We also obtained the H α and H β line luminosities from Malkan et al. (2017) to correct the [O III] line luminosities for extinction following Bassani et al. (1999) and assuming a Balmer decrement of 3.0 (Osterbrock & Ferland, 2006). Figure 4.9 shows the plot of [O III] line luminosity plotted against the integrated radio luminosity (νL_ν) at 5.5 GHz including the extended lobes, bright core and galaxy emission in the left panel, whereas in the right panel we have plotted the radio luminosity exclusively coming from the extended radio lobes. We defined regions to avoid the central unresolved core and any emission which is related to the host galaxy disk. In NGC 4593, we do not detect any extended emission and hence we did not include this source in the plot shown in the right panel. We avoided the radio emission from the galactic disk in the NGC 3079, and NGC 4388 while estimating the lobe luminosity.

Interestingly, we do not find a statistically significant correlation between radio luminosity (νL_ν) and [O III] luminosity ($L_{[O\ III]}$) when we use the integrated source radio luminosity. The Spearman’s rank correlation coefficient is 0.3 with a two-tailed p-value of 0.43. On the other hand, when we use only the extended radio emission and avoid the core contamination, we find that there is a significant correlation between νL_ν and $L_{[O\ III]}$. The corresponding Spearman’s rank correlation coefficient is 0.79 and the two-tailed p-value turns out to be 0.021. We used the least-square fitting to determine the slope of the relation between the extended radio emission and the line luminosity and the relation between the νL_ν and $L_{[O\ III]}$ is quoted in Figure 4.9.

It must be noted that there are several uncertainties in the extended flux density estimation. Our observations were carried out using the VLA B-array configuration as a result of which we might be missing flux from very diffuse structures. Also, the contamination from the star-formation related radio emission can not be completely accounted for, although efforts to avoid radio emission from location coinciding with the disk were taken. Despite these caveats, there

4. THE SEYFERT AND THE STARBURST GALAXY SAMPLE

appears to be a strong correlation between the radio luminosities from lobe-like features and the $L_{[O\ III]}$.

It was previously noted by Rawlings et al. (1989) and Baum & Heckman (1989) that there is a correlation between 178 MHz radio luminosity (dominated by extended radio emission) and the line luminosity whereas there is not much evidence for an intrinsic correlation between 5 GHz radio emission (often core dominated) and the NLR emission.

The $[O\ III]$ line being a forbidden line can only be found in the low-density regions like the NLR. Hence, the radio emission coming very close to the core, will not lead to $[O\ III]$ line emission and could be a plausible reason for the lack of correlation, when we take the core flux densities into account. However, the correlation of the $[O\ III]$ emission with the radio emission is suggestive of a common origin as was suggested by previous chapters as well.

To further investigate the origin of the extended radio emission itself, we created overlays of the radio total intensity emission over the HST narrow-band images of $[O\ III]$ emission for NGC 4388 and NGC 3516 (see Figure 4.10). These were the only two Seyfert galaxies in our sample which showed extended radio emission and also had HST $[O\ III]$ narrow-band images. There appears to be a spatial overlap in the radio emission and the $[O\ III]$ emission in both these objects. The underlying $[O\ III]$ emission is rather filamentary in nature in both these systems. The $[O\ III]$ emission is only seen towards the south of the core in NGC 4388 probably due to greater dust extinction towards the north. It is interesting to note that the $[O\ III]$ emission has a conical morphology aligned along the minor axis, which can be easily explained to be due to either wind shock-ionization or photoionization by the accretion disk emission.

On the other hand, NGC 3516 is another example where the $[O\ III]$ emission and the radio emission are aligned almost along the major axis. Moreover, both the $[O\ III]$ and radio emission posses an S-shaped symmetry rather than a bi-conical shape. Such symmetry can be introduced if a precessing jet leads to the $[O\ III]$ emission rather than a conical outflow and can not be explained using simple photoionization by the central engine.

Falcke et al. (1998) studied a sample of seven Seyfert 2 galaxies using VLA radio images and HST narrow-band images. Majority of them show a spatial

overlap between the emission line gas and the off-nuclear radio emission. More interestingly, four of their sources show evidence for an S-shaped symmetry in their emission line images. Clearly defined ionization cones are seen only in NGC 4388 and MrK 573 although the morphology of Mrk 573 in their images resembles the bulbous kpc-scaled radio emission in these Seyfert galaxies.

Also, in the previous section, we have argued from the study of radio-FIR correlation in these systems that the strengths of the shocks generated at galaxy-wide scales is inadequate to generate the amount of radio emission seen in these systems via shock acceleration. This along with the S-shaped symmetry seen in the emission-line images for several of these galaxies strongly suggest that jet driven shocks are a major contributor, or are driving the photo-ionized outflows at least in some of these sources, if not all.

4.5.3 Relative energy input from various mechanisms

In this section, we compare the relative contribution of each of the sources of energy namely AGN bolometric luminosity, star formation, and the jet.

4.5.3.1 Jet power

Several studies like Bîrzan et al. (2004) and Cavagnolo et al. (2010) derive empirical relations between the jet power and the radio luminosities by estimating the mechanical work done by the radio jets in inflating the X-ray cavities. These studies which use the total flux density of the radio features, mostly utilize lower frequency ($\nu \leq 1.4$ GHz) data. It was noted by Bîrzan et al. (2008) that the scatter for the relation derived using flux densities at lower radio frequency, namely, 327 MHz was lower compared to 1.4 GHz. Our observations were carried out using the VLA at 5 GHz in the B-array configuration, which is not the ideal setup to measure the total extended emission from lobes of the radio sources due to the complications like steep spectrum lobes and missing flux due to inadequate short baselines. Merloni & Heinz (2007) derive a similar relation between 5 GHz radio luminosity and jet power, however only using the nuclear radio luminosities rather than the integrated radio emission. We rely on the following equation from

4. THE SEYFERT AND THE STARBURST GALAXY SAMPLE

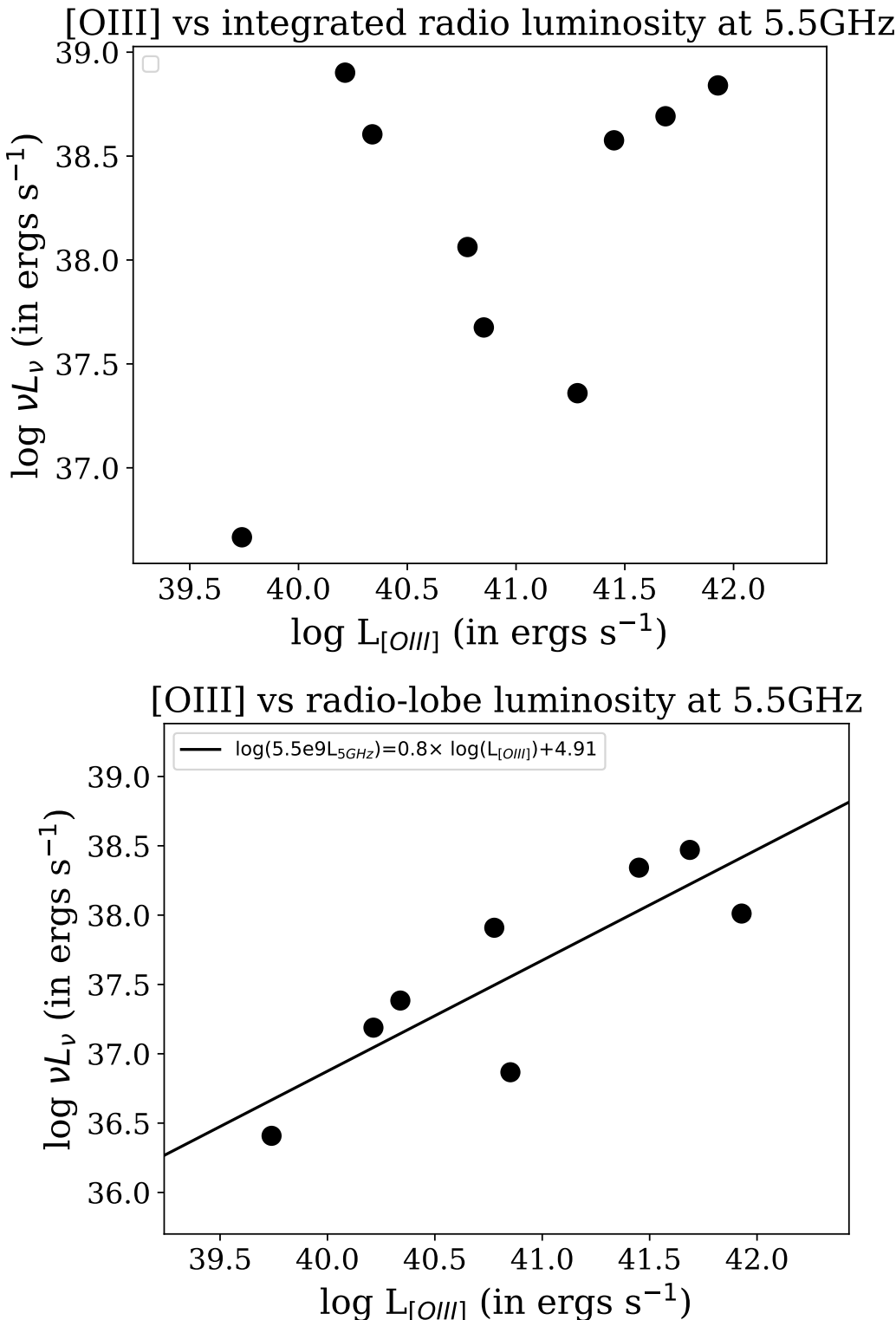


Figure 4.9: Top: [O III] line luminosity versus the integrated radio luminosity at 5.5 GHz. Bottom: [O III] line luminosity versus the radio lobe luminosity at 5.5 GHz.

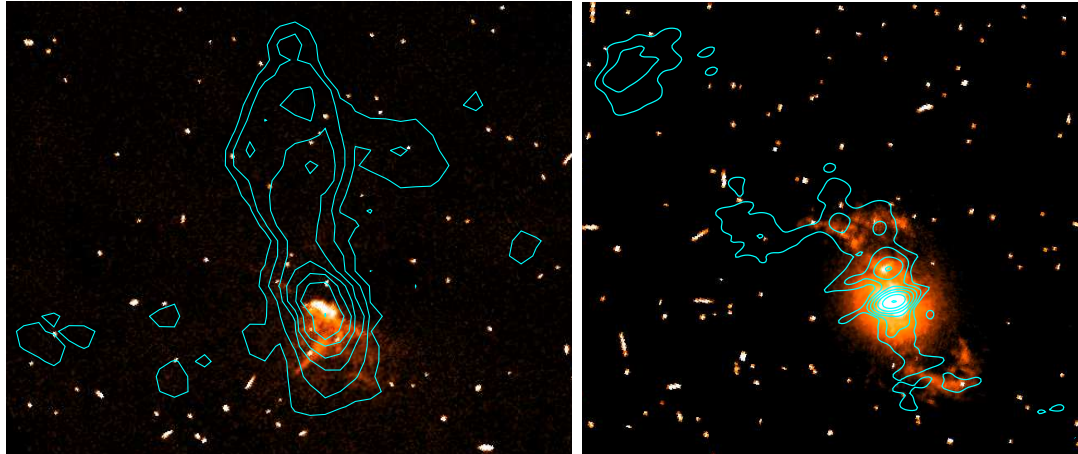


Figure 4.10: Overlay of radio continuum intensity contours in cyan on [O III] emission line images of NGC 4388 (Left) NGC 3516 (Right)

Table 4.3: Kinetic energy injection rates due to jets, AGN radiation and SFR

Source	S_{jet} (mJy)	dE/dt_{tot} (erg s $^{-1}$)	f_{jet}	f_{AGN}	f_{SFR}
NGC2639	44.53	43.36	0.906	0.001	0.094
NGC2992	12.48	43.21	0.251	0.583	0.166
NGC3079	151.8	43.12	0.704	0.007	0.289
NGC3516	2.88	42.7	0.31	0.544	0.147
NGC4051	2.31	41.79	0.24	0.242	0.518
NGC4235	5.49	42.56	0.611	0.353	0.036
NGC4388	4.47	42.99	0.206	0.331	0.463
NGC4593	2.12	42.89	0.161	0.644	0.195
NGC5506	125.05	44.09	0.15	0.836	0.014

Column 1: The target source. Column 2: The core flux density. Column 3: The total mechanical energy injection rates from the three mechanisms. Columns 4,5,6: Fractional contribution to the total injection rates from the jet, AGN accretion and star formation respectively.

4. THE SEYFERT AND THE STARBURST GALAXY SAMPLE

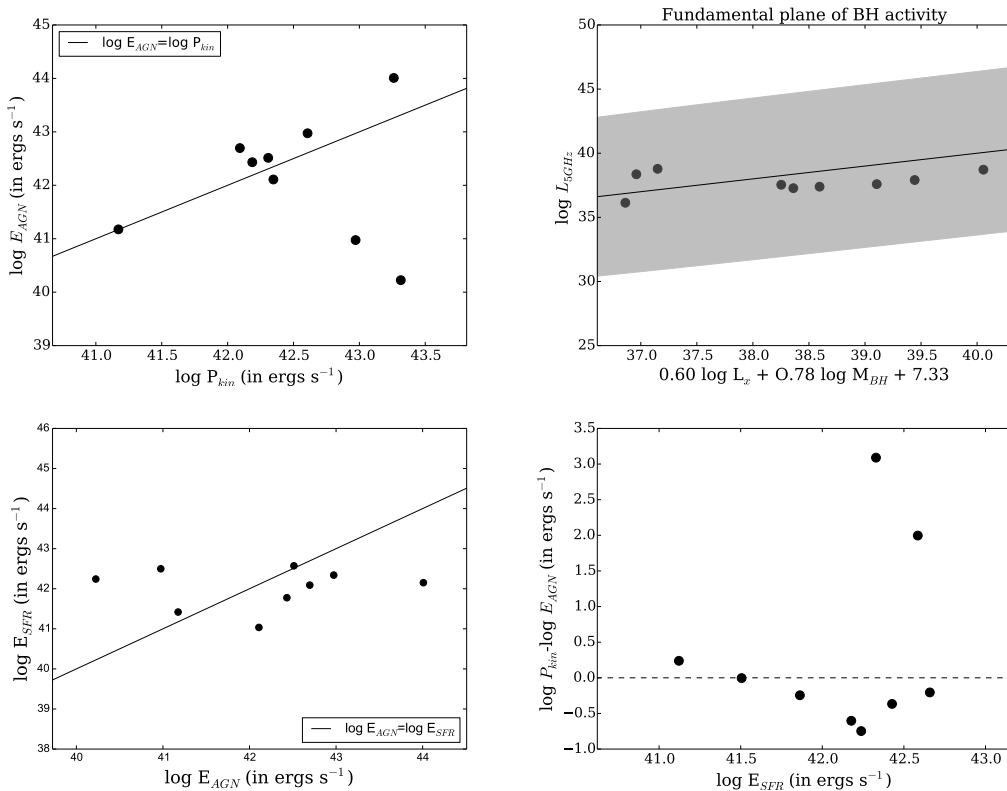


Figure 4.11: Top left: jet power versus AGN energy input rate from bolometric luminosities for the Seyfert sample. The identity line is indicated. Top right: The Seyfert sample in the fundamental plane of BH activity, along with its well-known scatter from observations in the literature in grey. Bottom left: AGN energy input rate from bolometric luminosities versus energy input from SFR. Bottom right: Energy injected from SFR versus the difference in AGN and jet power.

Merloni & Heinz (2007) to estimate the jet power.

$$\log(P_{\text{kin}}) = (0.81 \pm 0.11) \log(L_{5\text{GHz}}) + 11.9_{-4.4}^{+4.1} \quad (4.1)$$

We estimated the core flux densities from our VLA images at 5.5 GHz by fitting a Gaussian model with an underlying constant background to the core in the Seyfert galaxies. We used task ‘JMFIT’ in AIPS to do the fitting and the peak value is listed in the Table 4.3.

4.5.3.2 Kinetic energy from AGN bolometric radiation

We assume that a fraction ($\sim 5\%$) of the total AGN bolometric luminosity gets injected into the galaxy as kinetic energy (Di Matteo et al., 2005; Nesvadba et al., 2017). We derive the bolometric luminosities using hard X-ray (2-10 kev) luminosities taken from Malkan et al. (2017). Duras et al. (2020) computed a universal bolometric correction, K_X for a sample of both type-1 and type-2 AGN as a function of both X-ray luminosity and bolometric luminosity. They show that while K_X remains nearly unchanged for sources with $\log(L_{bol}/L_\odot) < 11$, it starts to increase beyond it. We used $K_X = a \left(1 + \left(\frac{\log(L_x/L_\odot)}{b}\right)^c\right)$ to obtain the bolometric AGN luminosities for our sources, where $a=15.33$, $b=11.48$ and $c=16.20$.

4.5.3.3 Energy injection rate due to star formation

Star formation accompanied by supernovae and stellar winds leads to the effective thermalization of the kinetic energy, which in turn leads to the formation of hot bubbles filled with tenuous plasma. This hot bubble expands into the lower pressure medium giving rise to a galaxy-wide outflow (Veilleux et al., 2005). For kinetic energy injected per solar mass of stars formed equal to 1.8×10^{49} ergs M_\odot^{-1} , 40% is carried away by the winds and the rest is assumed to be radiated away (Dalla Vecchia & Schaye, 2008). Hence a total of $0.72 \times 10^{49} \times \text{SFR}$ ergs s^{-1} is the net mechanical injection rate into the galaxy via star formation. Here, SFR is the star formation rate in $M_\odot s^{-1}$. To estimate the SFR, we used IRAS 60 μm and 100 μm fluxes from the IRAS catalog of galaxies and QSOs observed. We calculated SFR as $4.5 \times 10^{-44} L_{\text{FIR}}$ (Kennicutt, 1998), where $L_{\text{FIR}} = 4\pi D^2 \times \text{FIR} \times L_\odot$, where

4. THE SEYFERT AND THE STARBURST GALAXY SAMPLE

$\text{FIR} = 1.26(2.58f_{60} + f_{100}) \times 10^{-14}$, $L_{\odot} = 3.8 \times 10^{33}$ ergs s $^{-1}$ and the unit of f_{60} and f_{100} is W m $^{-2}$ (Helou et al., 1988).

In figure 4.11, we have compared the energy injection rates from all the three mechanisms discussed above. The top-left panel shows that the energy injection rate from the AGN bolometric luminosity and the jet is comparable in this sample. Almost half of the sources in our sample are distributed above and below the identity line. It can also be noted that there is no correlation between the jet emission and the AGN bolometric luminosity. Several studies investigating the relationship between the jet and the accretion disk emission have shown the existence of the “fundamental plane (FP) of black hole activity” (Merloni et al., 2003). This is the correlation between the 5 GHz radio luminosity representing the jet and the BH mass scaled X-ray luminosity representing the emission related to the accretion on the central black hole. Given, that our sources do not show a one-to-one correlation between the jet and the accretion, we test whether our sources follow the “fundamental plane of BH activity”. We have plotted the fundamental plane for our sources in the top right panel of Figure 4.11. The grey-shaded region represents the 1σ error in the original relation. While all our sources follow this relation within the errors, the Spearman’s rank correlation coefficient between the X and Y coordinates for our sources is 0.27 with a p-value of 0.49, suggesting no correlation. We note that our sample size is small, and therefore this study needs to be pursued with a larger sample. We also note however that the FP may intrinsically be flawed when it comes to jetted AGN (see for example, Zhang et al., 2018).

We also note that the trends seen in the top left panel of Figure 4.11 and the left panel of Figure 4.9 are similar to some extent. Both [O III] and hard X-ray emission are used as proxies for the bolometric luminosities and hence the coincidence. Saikia et al. (2018) studied the fundamental plane of black hole activity for a sample of LLAGN using radio luminosities derived using VLA A-array observations at 15 GHz. Interestingly, they study the correlation between both X-ray and [OIII] luminosities which are used as a proxy for the accretion rates and the core radio luminosity. They find that in both cases the radio luminosity correlates better with the BH mass scaled accretion rates rather than these quantities on their own. However, such a correlation would imply that

4.6 Conclusions and Summary

the extended radio emission in Seyfert galaxies is correlated with the accretion rates in these systems. In radio jets, the jet power seems to be correlated with a combination of black hole mass and accretion rate.

The plot of the energy injection rate from the star formation rate vs that from the bolometric luminosity of the AGN is plotted in the bottom-left panel of Figure 4.11. Here as well, there are about the same number of sources above and below the identity line. It is also obvious from the plot that the star formation rate does not depend on the AGN bolometric luminosities (Spearman's rank correlation coefficient is 0.083 with a p -value of 0.83). Hence, in our sample of sources, we do not see any evidence for AGN feedback. The bottom-right panel shows the jet power scaled by the AGN bolometric luminosity vs the energy injected due to star-formation. We see that all three processes inject comparable energies into the medium, except for two sources where the jet power dominates the other sources.

4.6 Conclusions and Summary

We have presented a polarization-sensitive VLA study of nine Seyfert galaxies along with a comparison sample of seven starburst galaxies at 1.5 and 5.5 GHz. We summarise the main results below.

1. Bubble-like or lobe-like radio emission is observed only in the Seyfert galaxies whereas the radio emission is more spread out over the galactic disks in starburst galaxies without an AGN.
2. Polarization is detected in four Seyfert galaxies (44% of the sample) and one starburst galaxy using regular imaging and two more using RM synthesis. A comparison of the polarization properties of our Seyfert galaxies in conjunction with those in the literature indicates parallel inferred magnetic fields at the lobe/bubble edges and mostly longitudinal fields inside the jets/lobes of the Seyfert galaxies, although signatures of RM gradients in some sources like NGC 2639, NGC 3079 and NGC 4388, point towards more complex magnetic field structures. While there appear to be differences in the fractional polarization of Seyfert galaxies and starburst galaxies (with

4. THE SEYFERT AND THE STARBURST GALAXY SAMPLE

higher values in the higher resolution images for Seyfert galaxies), more data are needed to confirm this. We conclude that polarization can indeed be used as a tool to distinguish between the AGN jet/lobe emission from that related to star-formation.

3. Lack of excess radio emission in superwind hosting starburst galaxies compared to the radio-FIR correlation rules out the shock origin (from supersonic winds) of the excess radio emission seen in Seyfert galaxies. While the origin of the synchrotron emission itself may not be dominated by stellar-related processes, the comparable mechanical power output from AGN accretion, jets, and star formation, suggests that they all might be playing some role in the long term evolution of the radio emission.
4. The correlation between the extended radio lobes and the [O III] line emission suggests a connection between the radio emission and the emission lines. We favor the jet-NLR interaction scenario based on the S-shaped symmetry observed both in radio continuum and emission lines, in a few Seyfert galaxies. Jets in Seyfert galaxies appear to be stunted due to a close interplay between the jet and surrounding media.

5

Episodic Activity in Seyfert Galaxies¹

5.1 Introduction

AGN are the energetic centres of galaxies that are powered by the release of gravitational potential energy as matter accretes onto supermassive black holes. Major and minor galaxy mergers play a key role in the release of angular momentum of galactic gas, brought all the way from kpc-scales to the small sub-parsec-scale accretion disks, to fuel the AGN (Barnes & Hernquist, 1991, 1996). Several merger events have therefore been suggested to explain the observed recurring AGN activity in many galaxies (Liu et al., 2003).

Among the radio-loud AGN class, double-double radio galaxies are understood to be clear signatures of recurrent AGN activity (Schoenmakers et al., 2000; Sebastian et al., 2018). Interestingly, the different epochs of emission are most often aligned with each other (Saikia et al., 2006). The lack of misalignment in most of the sources might point towards a constant black hole spin direction despite the restarting of the jet. Only rarely are some sources possessing misaligned pair of double lobes, seen (Akujor et al., 1996; Nandi et al., 2017). Misalignment in jet directions can be produced by slow precession which in turn can be caused by the warping of accretion disks, binary black holes (Begelman et al., 1980) or the

¹The contents of this chapter have been published in [Sebastian et al., MNRAS Letters, 2019, 490, L26](#), see here.

5. EPISODIC ACTIVITY IN SEYFERT GALAXIES

influence of a nearby neighbouring galaxy (Blandford & Icke, 1978). Coalescence of binary black holes has been suggested to cause a rapid spin flip in the primary black hole producing the jet, thereby producing jet misalignment between epochs (Dennett-Thorpe et al., 2002).

In radio-quiet AGN like Seyfert galaxies however, multiple radio lobes are not often reported or studied in detail. So far, only a handful of Seyfert galaxies which exhibit more than one pair of kpc-scale radio lobes, like Mrk 6 (Kharb et al., 2006) and NGC 2992 (Irwin et al., 2017) have been studied in detail. In this chapter we report the discovery of a second pair of radio lobes in new 5 GHz polarization-sensitive observations with the VLA, in the Seyfert galaxy NGC 2639. The newly discovered north-south oriented lobes are aligned nearly perpendicular to the well-known east-west lobes. NGC 2639 is a type 1.9 Seyfert (alternately classified as a LINER) hosted by an SA (ring) type grand-design spiral galaxy (Martini et al., 2003) at a redshift of 0.011128. We also present some tentative evidence for majority of the Seyfert galaxies in our larger sample to show some evidence for episodic activity.

5.2 Observations and Data Analysis

NGC 2639 was observed using the Expanded VLA (project ID: 17B_074) at 5 GHz (4.424 – 6.44 GHz) in full polarization mode using the B array configuration. The band was divided into 16 spectral windows (spws) each with a bandwidth of 128 MHz. 0832+492 was used as the phase calibrator whereas 3C138 was the flux density as well as polarization calibrator. 3C84 was used for calibrating the polarization leakage terms. Initial data editing and calibration were carried out using the CASA pipeline for VLA data reduction. The polarization calibration was carried out after the basic flux and phase calibration was completed. We followed the data reduction and imaging steps similar to those elaborated in Sebastian et al. (2019b).

We made use of the multi term-multi frequency synthesis (MT – MFS; see Rau & Cornwell (2011) for more details) algorithm while imaging in CASA to correct for wide-band related errors while deconvolving. The I, Q and U images of NGC 2639 were made using task `tclean` in CASA. Three rounds of phase-only

5.2 Observations and Data Analysis

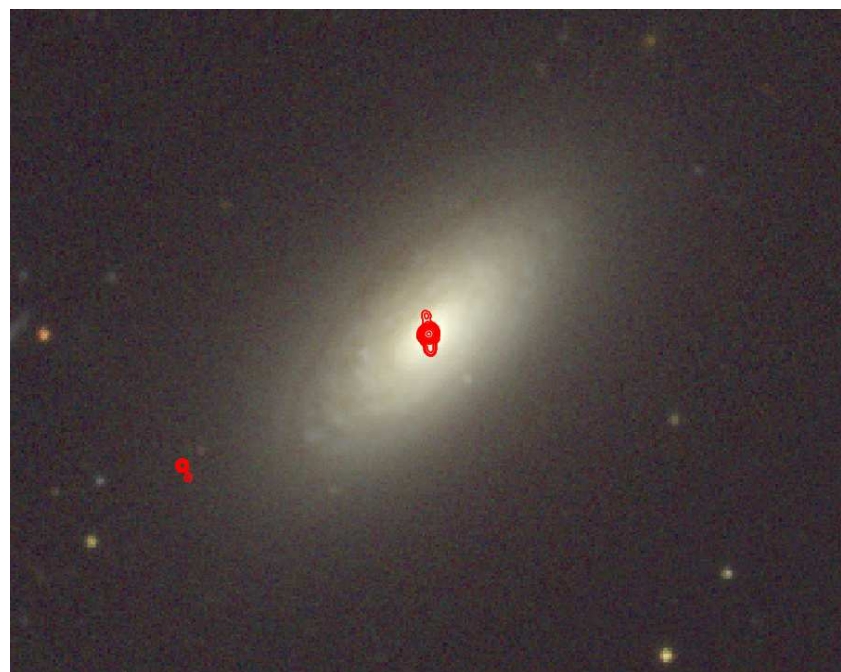


Figure 5.1: The color SDSS image of NGC 2639 superimposed by 5 GHz VLA radio contours in red, clearly showing the presence of the newly discovered north-south radio lobes.

5. EPISODIC ACTIVITY IN SEYFERT GALAXIES

self-calibration was carried out before a final round of A&P self-calibration. We used nterms =2 while carrying out the MT – MFS clean in CASA. In order to obtain accurate spectral index maps, the VLA calibrated data file was therefore divided into four parts, each consisting of 4 spectral windows. The imaging of these four data sets were carried out using common cell size, image size and a restoring beam ($1.22'' \times 1.22''$). We blanked all the pixels which had total intensity values less than 3σ in any of the images. We then fitted a power law to flux densities at each pixel as a function of the frequency to estimate the in-band spectral index values.

The total polarization image and the polarization angle images were produced from the Q and U images. We corrected for Ricean bias using the task **COMB** in Astronomical Image Processing System (**AIPS**). In order to make the rotation measure image the calibrated data were divided into four chunks each with 500 MHz bandwidth. The images were then convolved to the same beam size of $1.3'' \times 1.3''$. The task **rmfit** was used to generate an RM image from the ‘QU’ Stokes image cubes. The pixels where the error in RM was greater than 150 rad m^{-2} were blanked. The final r.m.s. noise in the VLA total intensity and polarization images is $\sim 10 \mu\text{Jy beam}^{-1}$. In addition to the new VLA data, we also analyzed archival VLA data at 5 GHz from 1998 (Project ID: GL022) and Very Long Baseline Array (VLBA) data at 8.3 GHz from 2011 (Project ID: BC196J). We followed standard data reduction procedures as described in the AIPS cookbook for VLA and VLBA data¹.

5.3 Results

Figure 5.1 shows the total radio intensity image at 5 GHz superimposed on the SDSS *gri* band color composite image of NGC 2639. Figure 5.2 shows the polarization and total intensity image from VLA, as well as the total intensity images from historical VLA and VLBA. The new north-south radio lobes with a prominent ‘core’ are clearly seen in Figures 5.1 and 5.2. The ‘core’ is the already known triple core-jet structure observed by Thean et al. (2000) and Baldi et al. (2018).

¹<http://www.aips.nrao.edu/CookHTML/CookBookap1.html#x168-369000A>.
<http://www.aips.nrao.edu/CookHTML/CookBookap3.html#x180-386000C>.

5.3 Results

The VLBA image shows a one-sided jet which is misaligned with the lobes seen in both the VLA and the archival VLA images. The linear size of each of the north-south lobes is ~ 0.8 kpc. The extent of the east-west lobes is ~ 180 parsec on each side of the core, whereas the VLBA core-jet extent is ~ 3 parsec. It is clear from the optical image of the host galaxy that the radio lobes are misaligned with the optical disk. The position angle (PA) of the host galaxy is 136° whereas the PA of the north-south radio lobes is -174° and that of the east-west lobes is 106° . The radio morphology of NGC 2639 resembles a Seyfert galaxy with lobes like Mrk 6 (Kharb et al., 2006) or NGC 6764 (Kharb et al., 2010a).

The north-south radio lobes are highly polarized showing an average fractional polarization of $20 \pm 3\%$ in the southern lobe and $30 \pm 7\%$ in the northern lobe. Although the southern lobe is brighter in total intensity, the average fractional polarization is slightly higher in the northern lobe. For the optically thin radio lobes in NGC 2639, the inferred magnetic field structures are aligned with the direction of the lobes, but show a slight change in orientation (by about 30°) at the end of the lobes, both in the north and the south.

The in-band rotation measure (RM) image is shown in Figure 5.5. The average spectral index in the northern lobes is $\sim -0.26 \pm 0.05$ while that in the southern lobes is $\sim -1.4 \pm 0.3$. The core has a flat mean spectral index of -0.16 ± 0.02 . The RM of the southern lobe has a mean value of $\sim 70 \pm 50$ rad m 2 . There appears to be an RM gradient in the southern lobe roughly in the north-west - south-east direction. A suggestion for an RM gradient is also observed in the northern lobe roughly in the east-west direction. The “minimum energy” magnetic field strength (see O’Dea & Owen, 1987) for a volume filling factor and proton to electron ratio (k) of unity, is $12 - 14$ μ G and ~ 88 μ G for the north-south lobes and ‘core’, respectively, for NGC 2639.¹ The volume was estimated using the observed projected length and width of the lobes. The corresponding electron lifetimes (undergoing both synchrotron and inverse Compton losses over CMB photons van der Laan & Perola, 1969) are $12 - 16$ Myr and 0.8 Myr for the north-south lobes and ‘core’, respectively.

¹For $k = 100$, the magnetic field is underestimated by a factor of $(k + 1)^{\frac{1}{\alpha+3}}$ or $3 - 4$.

5. EPISODIC ACTIVITY IN SEYFERT GALAXIES

We also estimated the star-formation rates from the Spitzer space telescope infrared fluxes using the clumpyDREAM code. The details of the fitting code itself is summarized in the appendix of Sales et al. (2015). It fits models simultaneously to infrared spectra and broadband SEDs. Since there was no evidence for a strong AGN component in the infrared, only an ISM model (Draine & Li, 2007) and a simple stellar population from GRASIL (Silva et al., 1998) were adequate to fit the spectrum. Figure 5.3 shows the plot of the SED fit and its residual. The SFR turn out to be of the order of $1 M_{\odot} \text{ yr}^{-1}$, lower than that estimated from the radio flux densities (using Equation 28 in Condon et al., 2002). This fact along with the collimated morphology of the lobes as well as high degree of linear polarization and an organised magnetic field structure, all point to an AGN origin for the radio lobes in NGC 2639.

5.4 Discussion

The discovery of an additional pair of radio lobes in our polarization-sensitive historical VLA observations at 5.5 GHz makes NGC 2639 only the third known Seyfert galaxy after Mrk 6 and NGC 2992, with multiple pair of lobes on kpc scales aligned at different angles to each other. Multiple lobes have also been hinted at in the polarization image of NGC 3079 in the CHANG-ES survey (Irwin et al., 2017). We note that weak signatures of a north-south extension could be seen in previous images of NGC 2639 in the literature using VLA and eMERLIN (e.g., Baldi et al., 2018; Gallimore et al., 2006). However, the high degree of polarization along with the ideal resolution of our VLA image has helped us in discovering the second pair of lobes. The case of NGC 2639 is similar to NGC 2992 where an extra pair of lobes which was previously not revealed in total intensity due to contamination from the galaxy disk emission, was discovered in polarized emission by Irwin et al. (2017).

Several possibilities can lead to the observed double set of lobes in NGC 2639, including (a) slow jet precession, (b) a pair of binary black hole at the center each launching independent jets, (c) recurrent jet activity at a misaligned angle.

The 5 GHz VLBI image of NGC 2639 from Lal et al. (2004) shows a curved parsec-scale jet bent towards the south. A curved jet could indicate jet precession,

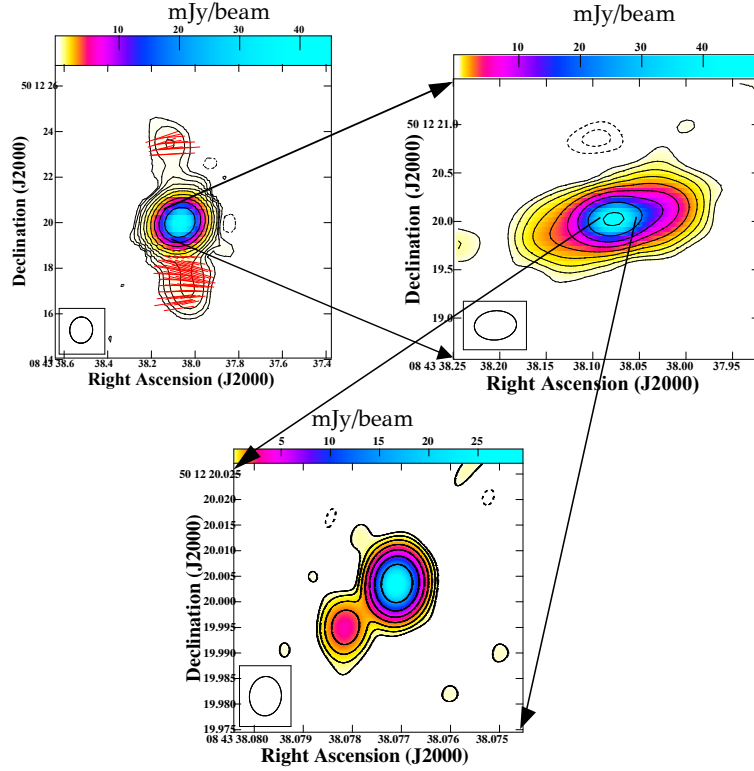


Figure 5.2: (Top left) 5.5 GHz total intensity radio contours of NGC 2639 with polarized intensity shown in color. Red ticks denote the polarization electric vectors with lengths proportional to the fractional polarization. Contour levels: $50 \times (-2, -1, 1, 2, 4, 8, 16, 32, 64, 128, 256, 512) \mu\text{Jy beam}^{-1}$. The newly discovered north-south lobes are highly linearly polarised. The beam shown in the bottom left corner is of size $1.15'' \times 1.00''$ at PA = -4.9° . (Top right) 5 GHz total intensity radio contours overlaid on colour image of the total intensity of NGC 2639. Contour levels: $164 \times (-2, -1, 1, 2, 4, 8, 16, 32, 64, 128) \mu\text{Jy beam}^{-1}$. The east-west lobes are embedded within the core of the image in the left panel. The beam shown in the bottom left corner is of size $0.435'' \times 0.302''$ at PA = 85.4° . (Bottom) 8.3 GHz archival VLBA image showing a ~ 1 parsec jet at PA = 130° . Contour levels: $239.2 \times (-2, -1, 1, 2, 4, 8, 16, 32, 64) \mu\text{Jy beam}^{-1}$. The beam shown in the bottom left corner is of size $7.7 \text{ mas} \times 6.2 \text{ mas}$ at PA = -5° .

5. EPISODIC ACTIVITY IN SEYFERT GALAXIES

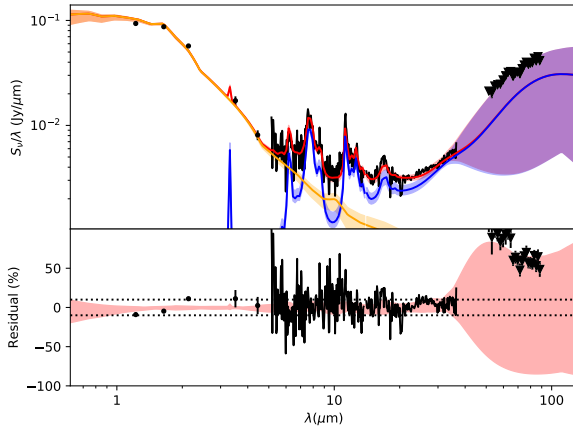


Figure 5.3: Plot of the infrared SED fit and its residual for NGC 2639. Data are in black, with upper limits (inverted triangles) for larger apertures relative to Spitzer Infrared Spectrograph, IRS (in this case, Multiband Imaging Photometer, MIPS, SED mode). The starlight model is in orange, ISM model in blue, the sum is in red. Lines show the best fit, and the shaded region shows the range of realizations for that model component (or sum). The systematic uncertainty is expected to be about 10%, indicated by dotted lines on the residuals plot. The statistical noise can exceed 10% for the short wavelength end of the IRS spectrum.

5.4 Discussion

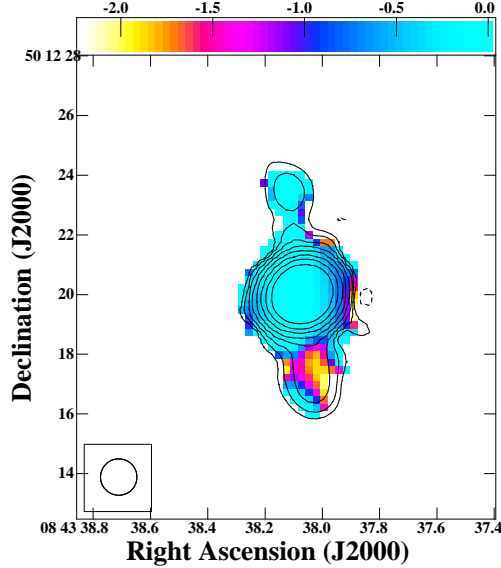


Figure 5.4: The in-band spectral index image of NGC 2639 in color with 5 GHz radio contours superimposed. Contour levels: $50 \times (1, 2, 4, 8, 16, 32, 64, 128, 256, 512)$ $\mu\text{Jy beam}^{-1}$. The beam shown in the lower left corner is of size $1.15'' \times 1.00''$ at PA = -4.9° .

which in turn could arise from a warped accretion disk or the presence of binary black holes. It is unlikely however, that the two sets of lobes is caused due to slow jet precession because of a lack of connection between these two jets as usually seen in the case of X or S-shaped sources. No continuity or connection is seen between the N-S and E-W lobes in the image of NGC 2639 in Figure A1 from Baldi et al. (2018), where both the lobes can be seen simultaneously. We note however, that it is difficult to suggest what looks like diffuse extension in the north-south direction in their image to be a separate set of lobes in the absence of polarization data.

Alternately, the two episodes of AGN activity are a result of a minor gas-rich merger which created a new accretion disk in a direction driven by the angular momentum of the inflowing gas and which consequently created a jet in a different direction to the previous episode. While the VLBI image does not indicate the presence of black hole binaries in NGC 2639, sub-parsec-scale binaries cannot be ruled out with present day VLBI experiments. In addition, it is possible that

5. EPISODIC ACTIVITY IN SEYFERT GALAXIES

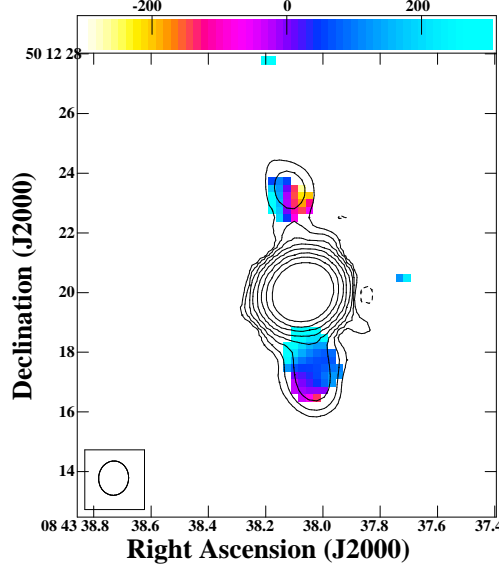


Figure 5.5: The in-band rotation measure image of NGC 2639 in color with 5 GHz radio contours superimposed. Contour levels: $50 \times (1, 2, 4, 8, 16, 32, 64, 128, 256, 512)$ $\mu\text{Jy beam}^{-1}$. The beam shown in the lower left corner is of size $1.15'' \times 1.00''$ at PA = -4.9° .

currently both the black holes are not launching jets simultaneously, and hence both are not visible. The probability that the two sets of lobes result from a binary black hole pair with one set of lobes each is $< 0.02\%$ if we consider the probability of binary black holes in optically-selected SDSS QSOs (0.1%; Foreman et al., 2009) and the probability of a Seyfert galaxy producing a kpc-scale radio lobes ($\geq 44\%$; Gallimore et al., 2006). NGC 2639 was one among the 10 Seyferts from our larger sample that was observed with the VLA. NGC 2992, which also shows two pairs of lobes is part of our sample as well. Hence, the probability of multiple set of lobes estimated from our sample is 20%, which is much higher than the expected occurrence rate of binary black holes launching jets. Of course we note the caveat of our small sample size. Given the relatively undisturbed morphology of the host galaxy, any merger that might have contributed a second supermassive black hole must have been minor. Since the black hole mass and bulge mass of a galaxy are correlated (Magorrian et al., 1998), it is probable that the second black hole mass would be much smaller and hence less likely

5.4 Discussion

to produce its own radio jet. For instance, Baldi et al. (2018) found that black hole masses needed to be $> 10^6 M_\odot$ for producing radio jets. Hence, both the probability estimates and the undisturbed morphology of the host galaxy argues against the feasibility of the binary black hole model.

Irwin et al. (2017) consider the scenario where the lobe misalignment occurs as a result of interaction with ambient medium, which deflects the radio lobes along the direction of steepest pressure gradient. Given that in NGC 2639 the lobes are well confined within the galaxy itself, interaction with the ISM is inevitable. With additional estimates of parameters like the pressure exerted by the ISM on the lobes, which can be derived from X-ray measurements, useful constraints on the amount of jet bending can be obtained (Fiedler & Henriksen, 1984). Such bending should lead to an alignment with the galaxy minor axis. The PAs of various components listed in Section 5.3 suggest that the east-west lobe is misaligned with the host galaxy minor axis by $\sim 60^\circ$, whereas the north-south lobe is misaligned only by $\sim 40^\circ$. The fact that the galaxy minor axis lies in between the current position angles of both the set of lobes, undermines this model. Any bending induced by ISM interaction should have been closer to 60° rather than $\gtrsim 90^\circ$ that is observed in NGC 2639.

Lastly, we consider the episodic activity model. Recurrent activity which leads to the formation of lobes at different angles is a possibility that has been invoked to explain such structures in radio galaxies (Nandi et al., 2017). A comparison of images at different resolutions can provide us a handle on the currently active lobes. The parsec-scale jet in Lal et al. (2004) pointing towards the east in NGC 2639 might have been indicative of the large-scale east-west lobe being the currently active jet. In addition to the jet bending seen in parsec scales (Lal et al., 2004), the jet seen in the archival VLBA image presented in this chapter which is at a lower resolution compared to Lal et al. (2004) is aligned at an angle which is in-between both of the kpc scale lobes. It is therefore possible in principle, that the north-south lobes could be fed by the VLBI jet. Moreover, the relative total intensity of the eastern and western outflows inside the ‘core’ (top right panel of Figure 5.2) clearly shows the western one to be brighter and perhaps Doppler-boosted on ~ 200 parsec-scales, whereas the eastern jet is the approaching one in the VLBI images. It is however possible that the asymmetry

5. EPISODIC ACTIVITY IN SEYFERT GALAXIES

in brightness on the 100-parsec-scale is result of asymmetric environments rather than Doppler-boosting. While the degree of polarization is comparable in the two lobes to the north and south (it is marginally higher in the northern lobe, which could be due to an intrinsically highly polarized jet/knot region), the fact that the southern lobe shows a larger polarized lobe extent is consistent with it being the approaching lobe (e.g., Garrington et al., 1988). The fact that all angles are measured in projection, must of course, be borne in mind.

From the image of NGC 2639 presented in Baldi et al. (2018), it can be seen that the north-south lobes appear more diffuse, whereas the east-west lobes are more collimated which might be suggestive that the north-south lobes form the older set of lobes which had more time to expand adiabatically even after the switching off of the central engine. The spectral index values are also flatter in the ‘core’ compared to that in the north-south lobes, which is also in accordance with north-south lobes forming the older epoch of emission. Gallimore et al. (2006) quote a duty cycle of $\geq 44\%$. An average duration of each of the outflows can be determined from the duty cycle which is defined as $\tau_{flow} = 44\tau_8 n^{-1}$ Myr. Here $\tau_8=1$ is the typical Seyfert activity time-scale in 10^8 yrs and n is the number of outflows. For $n=2$ and assuming $\tau_8=1$, we derive an outflow duration of 22 Myr which is also comparable to the derived electron lifetime of the northern lobe (~ 16 Myr).

Could the restarted AGN activity in NGC 2639 be a consequence of a minor galaxy merger? (e.g., Capetti & Balmaverde, 2006). The SDSS optical image however, does not show any tidal tail features or other outward signatures of a recent merger. The host galaxy does possess a bar and a stellar ring (e.g., Márquez et al., 1999) which could be indicative of morphological irregularities caused by a past gas-rich merger. It is also noteworthy that there has been a $\sim 90^\circ$ change in the jet direction between the two AGN activity episodes, similar to what is observed in Mrk 6 by Kharb et al. (2006). Such rapid jet flips have been suggested to be a consequence of the presence or mergers of binary supermassive black holes (Kharb et al., 2017; Merritt & Ekers, 2002).

The lack of polarization from most of the ‘core’ region is likely to be due to the presence of copious amounts of magneto-ionised gas belonging to gas in the BLR, the NLR or the central ISM of the host galaxy. Using a very high-resolution study

of core-dominated AGN, O'Dea (1989) puts an upper limit of 200 rad m^{-2} on the integrated RM introduced by the magneto-ionic medium. The north-south lobes on the other hand show an r.m.s. RM value of $\sim 125 \text{ rad m}^{-2}$. For an average magnetic field value of $\sim 13\mu\text{G}$ and a path length of ~ 100 parsec, we obtain an electron density $n_e \sim 0.1 \text{ cm}^{-3}$. The volume averaged electron density typically seen in the warm interstellar medium (WIM) ranges from 0.01 cm^{-3} to 0.1 cm^{-3} (Gaensler et al., 2008). On the other hand, Kakkad et al. (2018) show that the electron densities in the NLR region varies from $\leq 50 - 2000 \text{ cm}^{-3}$. The observed RM in NGC 2639 could therefore be due to WIM or the intercloud NLR gas. As O'Dea (1989) point out, the RM could still arise from NLR if the path-length is overestimated, or if the magnetic field is highly tangled leading to less apparent rotation of the electric vectors.

The magnetic field orientation is aligned with the lobe direction both in the north and the south, but there is a 30° change in magnetic field orientation right at the end of the lobes. These could indicate a change in the flow direction of the radio emitting plasma, as in an S-shaped radio jet. While the magnetic fields are aligned along the lobe axis in both the north and south lobes, the RM gradient in the northern lobe is suggestive of a large-scale helical or toroidal magnetic field (Asada et al., 2002; Kharb et al., 2009), whereas the southern lobe shows an RM gradient in the longitudinal direction, which points to a greater complexity in the magnetic field structure.

5.4.1 Episodic Jet Activity in the sample

Similar to NGC 2639, the radio morphology of the Seyfert galaxy NGC 4388 in our VLA data suggests at least two episodes of activity. Multiple activity episodes are suggested for NGC 5506 based on the different lobe position angles (PAs) in our data and those of Gallimore et al. (2006). Secondary lobes have been detected in polarized emission in the Seyfert galaxy NGC 2992 by Irwin et al. (2017). There also appears to be a sharp change in the jet PA of NGC 3516 in our data; the inner lobe itself shows an S-shaped morphology which is followed closely by the [O III] gas. The GMRT images at 325 and 610 MHz of the Seyfert galaxy NGC 4235 by Kharb et al. (2016) suggest the presence of relic lobe emission.

5. EPISODIC ACTIVITY IN SEYFERT GALAXIES

Therefore overall, the majority of our sample Seyfert galaxies show indications of episodic AGN activity.

We checked the spectral index images generated as a by-product of MS-MFS imaging in CASA for NGC 4388, NGC 3516, and NGC 2992. We find that in both NGC 4388 and NGC 3516, the outer lobes show steeper spectral indices compared to the inner lobes. Using the sub-band data, we have created a poorer-resolution ($\sim 5''$) two-point spectral index image of NGC 4388 (see Figure ??). While the image naturally appears noisy owing to the narrow range of frequencies used, the steepness of the outer lobe to the north, is clearly visible. Such a steep spectrum in the outer lobes is consistent with the presence of an older population of plasma in the outer lobes. On the other hand, in NGC 2992, the outer lobe towards the north shows a flatter spectral index compared to the inner ones. The emission in the outer lobes is not very prominent and hence the result needs to be cross-checked with newer observations. We see a similar trend in the spectral index image of NGC 2992 produced by the CHANG-ES survey (Irwin et al., 2012), although the resolution of the images is relatively poor to make strong claims. However, if real, this may mean that some re-acceleration process is at play in the outer lobes.

The “spin-paradigm” has been invoked for explaining the evolution of black holes and the radio-loudness observed in AGN (Hughes & Blandford, 2003; Sikora et al., 2007; Wilson & Colbert, 1995). Mergers of galaxies were suggested to be causing the spin-up or spin-down of the black hole, depending on whether the new accretion disk was co-rotating or counter-rotating with respect to the black hole (Hughes & Blandford, 2003; Sikora et al., 2007; Wilson & Colbert, 1995). From the lifetime estimates of Seyfert jets and the minimum statistical lifetime of Seyfert activity in a particular galaxy, Sanders (1984) have argued that there might be as many as 100 episodes of AGN activity in Seyfert galaxies, with each episode lasting less than 10^6 years. These might be induced by several minor mergers leading to the formation of a new accretion disk each time, with an orientation dependent on the mass inflow direction. This would in turn result in multiple radio outflows, misaligned with each other. Our present study is consistent with these suggestions of short-lived episodic activity in Seyfert galaxies.

Several multi-epoch studies of Seyfert galaxies using the VLBA have shown that most of these sources have sub-relativistic speeds often of the order of $0.1c$ (Middelberg et al., 2004; Ulvestad, 2003). On the other hand, many of the radio galaxies have relativistic speeds near their cores, and the hotspots in some giant radio galaxies were shown to possess speeds as high as $0.1c$ using spectral aging analysis (Jamrozy et al., 2005). However, the speeds are lower by about an order of magnitude, while dynamical ages are used. The spectral ages of giant radio galaxies are reported to be ~ 30 Myr. The low-speeds in Seyfert galaxy jets along with comparable values of spectral ages suggest that the major difference between Seyfert galaxy jets and that seen in powerful radio galaxies are probably the jet velocities. So these jets are probably not simply weak in terms of radio luminosity, but also velocities (Ulvestad, 2003).

5.5 Summary

We report here the discovery of a new pair of north-south oriented radio lobes in the Seyfert galaxy NGC 2639; this galaxy has been known to possess an east-west core-jet structure. The in-band RM image shows gradients in both the lobes indicative of organised magnetic field structures on kpc-scales. The magnetic field structure is aligned with the jet/lobe direction in both the lobes, but shows a change in orientation around the terminal point; an S-shaped radio outflow is implied. The presence of a twin pair of orthogonally aligned radio lobes in NGC 2639 is highly reminiscent of the Seyfert galaxy Mrk 6. Based on the settled optical morphology of the host galaxy, it is likely that a minor merger that did not disrupt the host galaxy structure is responsible for the observed features in NGC 2639. This also explains the near 90° change in the jet direction; the current jet direction being the result of a new accretion disk formed by the minor merger, whose direction was a result of the angular momentum of the inflowing merger gas. Additional radio images at better resolution revealing more details of the north-south outflow along with the east-west lobes, can provide more definitive clues. For example, determining the ages of both the lobes simultaneously can give insights into the time elapsed between the stopping and restarting of the jets, which can in turn help in constraining various models (Dennett-Thorpe

5. EPISODIC ACTIVITY IN SEYFERT GALAXIES

et al., 2002). Furthermore, better resolution polarization images of the lobes can help identify any S-shaped outflow which is suggested by our current data.

6

Conclusions and Future Work

The primary aim of this thesis was to understand the outflows in radio quiet AGN like Seyfert and LINER galaxies. We used polarimetric techniques to disentangle the effects of AGN outflows from stellar-related processes. We, therefore, observed a comparison sample of starburst galaxies in this thesis. This is for the first time that such a comparison study has been carried out using polarimetric techniques. The advent of the wideband receivers has significantly reduced the sensitivity limitations of radio telescopes like the VLA enabling it to probe weak polarization features. In this chapter, we summarize our main findings, the limitations of the current study, and future work.

6.1 Summary of the thesis

I have presented a radio polarimetric study of a sample of Seyfert galaxies in conjunction with a sample of starburst galaxies in an attempt to understand the origin of radio outflows in radio quiet AGN. From our polarization study, we conclude that the radio emission shows greater polarization and complexities in Seyfert galaxies compared to the starburst galaxies. The detection rates of polarization in Seyfert galaxies at 5.5 GHz is higher (4/9) than the starburst galaxies (0/3). While we detect more polarization in our Seyfert galaxies than our starburst galaxies at the given resolution we did not detect polarization in the rest of our Seyferts probably owing to various depolarization effects at play. In Seyfert galaxies, most of the lobe emission was confined to well within the

6. CONCLUSIONS AND FUTURE WORK

galaxies and as a result, the ionized gas in the NLR and tangled magnetic fields close to the center of the galaxy can lead to depolarization within the telescope beam (Bower et al., 2017; Middelberg et al., 2005b).

On the other hand in starburst galaxies, we did not detect polarization mainly because the ordering scales of the starburst galaxies are large and are missed by the VLA B-array observations in both the total intensity and polarization images. Because of the high resolution of our images, we picked up more compact emission from local star formation regions rather than the diffuse halo with high polarization degrees. Since some of our Seyfert galaxies show very high degree of polarization at the resolution of our images, which means that the emission is indeed dominated by jets.

Since we need to recover the polarized signal from both the sample of galaxies and still be able to distinguish between them it would be ideal to make use of a slightly lower resolution array than our own study. This would help in recovering the diffuse emission from the starburst galaxies. However, we also do not want to lower our resolution too much to prevent beam depolarization from playing a major role. Also, in order to reduce the effects of bandwidth depolarization it would be ideal to choose a higher frequency, although this can also lead to non-detection of steep spectrum features.

Hence we chose a higher frequency (10 GHz) and D-array for our new observations. Preliminary results from our 10 GHz images are consistent with this suggestion. The Seyfert galaxies show a wide range of fractional polarization, sometimes as high as 30% in the radio lobes. At 1.4 GHz, one of the starburst galaxies, NGC 253 showed polarized emission in its central regions. RM synthesis resulted in the detection of marginal levels of polarization (1 – 3%) in two more starburst galaxies (UGC 903 and NGC 1134).

Most of the Seyfert galaxies showed polarization structures that implied aligned magnetic fields along the lobe edges. Another common feature is the presence of inferred longitudinal magnetic fields along the outflow directions. While such a topology might imply simple poloidal magnetic fields along the length of the KSRs in Seyfert galaxies, the RM gradient images of NGC 2639, and NGC 3079 suggest more complicated magnetic field structures. The KSRs themselves are not necessarily aligned along the minor axis of the galaxy.

6.1 Summary of the thesis

From the in-depth study of NGC 3079 we have concluded that the morphology of the radio lobes is a consequence of an interaction of the jet with the external factors like the dense ISM, the magnetic fields threading the galaxy. For the entire Seyfert sample, we studied the radio-FIR correlation. We find that many of the KSR hosting Seyfert galaxies show a “radio excess” above the radio-FIR correlation line. We hence ruled out the scenario where the relativistic material that has its origin in the star formation disk from the supernovae and H II regions, is entrained along with AGN or starburst-driven winds. The possibility of the radio excess having its origin due to the shock acceleration of a thermal pool of electrons to relativistic energies exists. However, a sample of starburst superwind galaxies without an AGN at its center did not show any evidence for a radio excess. Hence, we conclude that the shocks on these large galactic scales are not powerful enough to produce the radio emission comparable with that related to the galaxy itself. As a result, the radio emission itself is most likely AGN jet related.

We also studied the correlation between [O III] line luminosity and the radio luminosity for our sample of sources. We found that for our sources the correlation between the total radio luminosity at 5 GHz and the radio luminosity is weak, whereas when only the radio luminosity from the lobes is considered we find a stronger correlation. We favor a scenario where the correlation is a result of jet-NLR interaction rather than a scenario where the [O III] emission is a result of the photo-ionization from the AGN accretion, whereas the radio emission is produced as a result of the shock acceleration from the winds driven by AGN accretion. Since many of the Seyfert galaxies show the S-shaped symmetry in the [O III] narrow band emission-line images along with the radio images and we do not find much evidence in support of the shock acceleration scenario from our radio-FIR correlation study, we favor the jet-NLR interaction scenario. The “frustrated jet scenario” that emerges from our study is fully consistent with the small radio extents of the outflows in Seyfert galaxies.

To quantify the contribution of each of the possible driving mechanisms including AGN radiative winds, AGN jets, and starburst winds in the evolution of jets in our sample sources, we estimated the kinetic power contributed by each of the mechanisms into the ambient medium. We find that there is no one single

6. CONCLUSIONS AND FUTURE WORK

mechanism that is dominant in all of the sources. All three mechanisms contribute comparable kinetic power into the medium. This is again in favor of the “frustrated jet scenario”, according to which the later stages of evolution of the low power jets in these Seyfert galaxies are influenced by other processes such as the AGN radiative and starburst winds.

Another finding that emerges from this comparative study of the role played by each of these mechanisms, is a lack of correlation between the AGN bolometric luminosities and the star-formation, possibly indicating that AGN feedback does not regulate the star-formation in our sample of Seyfert galaxies.

Finally, we find that majority of our Seyfert galaxies show some evidence for episodic activity. Misaligned pairs of lobes were identified in the majority (5/9) of Seyfert galaxies. From past detailed studies of similar Seyfert galaxies like NGC 2992 (Irwin et al., 2017), Mrk 6 (Kharb et al., 2006), and NGC 2639 (included in this thesis), we find that the most favored model is “restarted AGN activity”. From our study, we find that the AGN jet duty cycle in radio quiet AGN like Seyfert galaxies is much shorter than that is observed in radio loud AGN.

To summarize, our study has resulted in several new findings compared to the previous work in the field. For example, we found that polarization properties of Seyfert galaxies including their polarization structures, polarization fraction, etc differ systematically from a population of starburst galaxies. Our study of the radio-FIR correlation and the correlation between [O III] line luminosity and the radio luminosity of the lobes provided more evidence for the jet origin of the radio emission in Seyfert galaxies than that was available from past studies. Another unanticipated result that emerged from our studies was the higher rate of episodic activity in Seyfert galaxies when compared to the radio galaxies.

As the next step, we have recently acquired polarization-sensitive VLA D-array 10 GHz data for the entire Seyfert-starburst sample. Early results are extremely encouraging with much more polarised emission detected in the Seyfert lobes and host galaxies, as well as the starburst disks and halos. We plan to obtain spectral index and RM images of the entire sample to fully understand the nature of radio outflows and their galactic environments, in radio quiet AGN (Sebastian et al. 2021, in prep.)

Bibliography

- Aartsen M. G., et al., 2017, ApJ, 835, 45 12
- Adebahr B., Krause M., Klein U., Weżgowiec M., Bomans D. J., Dettmar R. J., 2013, A& A, 555, A23 61, 102
- Adebahr B., Brienza M., Morganti R., 2019, A& A, 622, A209 64
- Akujor C. E., Leahy J. P., Garrington S. T., Sanghera H., Spencer R. E., Schilizzi R. T., 1996, MNRAS, 278, 1 117
- Allen R. J., Baldwin J. E., Sancisi R., 1978, A& A, 62, 397 67
- Allen M. G., Dopita M. A., Tsvetanov Z. I., Sutherland R. S., 1999, ApJ, 511, 686 84
- Anderson J. M., Ulvestad J. S., 2005, ApJ, 627, 674 86
- Angel J. R. P., Stockman H. S., 1980, ARA&A, 18, 321 8
- Antonucci R., 1993, ARA&A, 31, 473 3, 4, 9, 10, 12
- Asada K., Inoue M., Uchida Y., Kameno S., Fujisawa K., Iguchi S., Mutoh M., 2002, , 54, L39 129
- Baan W. A., Irwin J. A., 1995, ApJ, 446, 602 42
- Baldi R. D., et al., 2018, MNRAS, 476, 3478 16, 120, 122, 125, 127, 128
- Baldwin J. A., Phillips M. M., Terlevich R., 1981, , 93, 5 6
- Barnes J. E., Hernquist L. E., 1991, ApJL, 370, L65 117

BIBLIOGRAPHY

- Barnes J. E., Hernquist L., 1996, ApJ, 471, 115 117
- Bassani L., Dadina M., Maiolino R., Salvati M., Risaliti G., Della Ceca R., Matt G., Zamorani G., 1999, ApJS, 121, 473 107
- Battye R. A., Browne I. W. A., 2009, MNRAS, 399, 1888 25
- Baum S. A., Heckman T., 1989, ApJ, 336, 702 25, 106, 108
- Baum S. A., O'Dea C. P., Dallacassa D., de Bruyn A. G., Pedlar A., 1993, ApJ, 419, 553 16, 17, 41, 73
- Baum S. A., Zirbel E. L., O'Dea C. P., 1995, ApJ, 451, 88 5
- Beck R., 2015, , 24, 4 23, 26, 72, 73
- Beckmann V., Gehrels N., Favre P., Walter R., Courvoisier T. J. L., Petrucci P. O., Malzac J., 2004, ApJ, 614, 641 86
- Begelman M. C., Blandford R. D., Rees M. J., 1980, NATURE, 287, 307 117
- Begelman M. C., Blandford R. D., Rees M. J., 1984, Reviews of Modern Physics, 56, 255 71
- Bell A. R., Lucek S. G., 2001, MNRAS, 321, 433 23
- Bennert N., Jungwiert B., Komossa S., Haas M., Chini R., 2006, A& A, 459, 55 11
- Bernikov L. V., Semenov V. S., 1979, Geomagnetism and Aeronomy, 19, 671 64
- Berton M., et al., 2018, A& A, 614, A87 85
- Best P. N., Heckman T. M., 2012, MNRAS, 421, 1569 15, 56
- Bicknell G. V., 1994, ApJ, 422, 542 5
- Bicknell G. V., 1995, ApJS, 101, 29 5
- Binette L., Fosbury R. A., Parker D., 1993, , 105, 1150 24

BIBLIOGRAPHY

- Bîrzan L., Rafferty D. A., McNamara B. R., Wise M. W., Nulsen P. E. J., 2004, ApJ, 607, 800 62, 109
- Bîrzan L., McNamara B. R., Nulsen P. E. J., Carilli C. L., Wise M. W., 2008, ApJ, 686, 859 109
- Bland-Hawthorn J., Veilleux S., Cecil G., 2007, Ap& SS, 311, 87 17
- Blandford R., Eichler D., 1987, , 154, 1 19, 62, 63, 103
- Blandford R. D., Icke V., 1978, MNRAS, 185, 527 22, 118
- Blandford R. D., Payne D. G., 1982, MNRAS, 199, 883 20
- Blandford R. D., Rees M. J., 1974, MNRAS, 169, 395 13
- Blandford R. D., Znajek R. L., 1977, MNRAS, 179, 433 9, 13
- Blandford R., Meier D., Readhead A., 2019, ARA&A, 57, 467 12
- Blundell K. M., Kuncic Z., 2007, ApJL, 668, L103 19
- Blustin A. J., Fabian A. C., 2009, MNRAS, 396, 1732 19, 56, 68, 72
- Bonchi A., La Franca F., Melini G., Bongiorno A., Fiore F., 2013, MNRAS, 429, 1970 71
- Boolter R. V., Pedlar A., Davies R. D., 1982, MNRAS, 199, 229 68
- Böttcher M., 2007, Ap& SS, 309, 95 12
- Bower G. C., Dexter J., Markoff S., Rao R., Plambeck R. L., 2017, ApJL, 843, L31 134
- Bregman J. N., 1980, ApJ, 236, 577 50
- Brentjens M. A., de Bruyn A. G., 2005, A& A, 441, 1217 39, 95
- Brinkmann W., Laurent-Muehleisen S. A., Voges W., Siebert J., Becker R. H., Brotherton M. S., White R. L., Gregg M. D., 2000, A& A, 356, 445 22

BIBLIOGRAPHY

- Burn B. J., 1966, MNRAS, 133, 67 37, 39
- Capetti A., Balmaverde B., 2006, A& A, 453, 27 128
- Capetti A., Axon D. J., Macchetto F., Sparks W. B., Boksenberg A., 1996, ApJ, 469, 554 24, 106
- Cappi M., et al., 2006, A& A, 446, 459 86
- Carilli C. L., Holdaway M. A., Ho P. T. P., de Pree C. G., 1992, ApJL, 399, L59 50, 67, 88
- Cavagnolo K. W., McNamara B. R., Nulsen P. E. J., Carilli C. L., Jones C., Bîrzan L., 2010, ApJ, 720, 1066 109
- Cawthorne T. V., Wardle J. F. C., Roberts D. H., Gabuzda D. C., 1993, ApJ, 416, 519 27, 98
- Cecil G., Bland-Hawthorn J., Veilleux S., Filippenko A. V., 2001, ApJ, 555, 338 42, 53, 60, 61, 62, 65, 66, 102
- Cecil G., Bland-Hawthorn J., Veilleux S., 2002, ApJ, 576, 745 42, 60, 61
- Chelouche D., Netzer H., 2005, The Astrophysical Journal, 625, 95–107 20
- Christopoulou P. E., Holloway A. J., Steffen W., Mundell C. G., Thean A. H. C., Goudis C. D., Meaburn J., Pedlar A., 1997, MNRAS, 284, 385 85
- Cioffi D. F., Jones T. W., 1980, AJ, 85, 368 63
- Clarke C. J., Kinney A. L., Pringle J. E., 1998, ApJ, 495, 189 25
- Clausen-Brown E., Lyutikov M., Kharb P., 2011, MNRAS, 415, 2081 66, 97
- Colbert E. J. M., Baum S. A., Gallimore J. F., O'Dea C. P., Lehnert M. D., Tsvetanov Z. I., Mulchaey J. S., Caganoff S., 1996a, ApJS, 105, 75 16, 21, 86
- Colbert E. J. M., Baum S. A., Gallimore J. F., O'Dea C. P., Christensen J. A., 1996b, ApJ, 467, 551 41, 67, 73, 74, 86, 89, 105

BIBLIOGRAPHY

- Colbert E. J. M., Baum S. A., O'Dea C. P., Veilleux S., 1998, ApJ, 496, 786 87
- Collins J. A., Rand R. J., Duric N., Walterbos R. A. M., 2000, ApJ, 536, 645 88
- Condon J. J., 1992, ARA&A, 30, 575 103
- Condon J. J., Yin Q. F., Burstein D., 1987, ApJS, 65, 543 86
- Condon J. J., Cotton W. D., Broderick J. J., 2002, AJ, 124, 675 67, 122
- Crane P. C., van der Hulst J. M., 1992, AJ, 103, 1146 97
- Croton D. J., et al., 2006, MNRAS, 365, 11 42
- Crummy J., Fabian A. C., Gallo L., Ross R. R., 2006, MNRAS, 365, 1067 22
- Dahlem M., Lisenfeld U., Golla G., 1995, ApJ, 444, 119 89
- Dahlem M., Weaver K. A., Heckman T. M., 1998, ApJS, 118, 401 74, 88, 105
- Dalla Vecchia C., Schaye J., 2008, MNRAS, 387, 1431 113
- Damas-Segovia A., et al., 2016, ApJ, 824, 30 86, 96
- Das M., Vogel S. N., Verdoes Kleijn G. A., O'Dea C. P., Baum S. A., 2005, ApJ, 629, 757 6
- Davies R. I., Sternberg A., Lehnert M. D., Tacconi-Garman L. E., 2005, ApJ, 633, 105 87
- Dennett-Thorpe J., Scheuer P. A. G., Laing R. A., Bridle A. H., Pooley G. G., Reich W., 2002, MNRAS, 330, 609 118, 131
- Denney K. D., et al., 2009, ApJ, 702, 1353 85
- Dewangan G. C., Griffiths R. E., Dasgupta S., Rao A. R., 2007, ApJ, 671, 1284 22
- Di Matteo T., Springel V., Hernquist L., 2005, NATURE, 433, 604 113
- Dopita M. A., Sutherland R. S., 1996, ApJS, 102, 161 25

BIBLIOGRAPHY

- Draine B. T., Li A., 2007, ApJ, 657, 810 122
- Dumas G., Mundell C. G., Emsellem E., Nagar N. M., 2007, MNRAS, 379, 1249 85
- Duras F., et al., 2020, arXiv e-prints, p. arXiv:2001.09984 113
- Duric N., Seaquist E. R., 1988, ApJ, 326, 574 42, 62, 64, 67, 68, 97
- Duric N., Irwin J., Bloemen H., 1998, A& A, 331, 428 67
- Durrer R., Neronov A., 2013, , 21, 62 23
- Dursi L. J., Pfrommer C., 2008, ApJ, 677, 993 65
- Edelson R. A., 1987, ApJ, 313, 651 15
- Edge D. O., Shakeshaft J. R., McAdam W. B., Baldwin J. E., Archer S., 1959, , 68, 37 2
- Ekers R. D., Sancisi R., 1977, A& A, 54, 973 67, 88
- Elitzur M., Ho L. C., Trump J. R., 2014, MNRAS, 438, 3340 26
- Elmouttie M., Haynes R. F., Jones K. L., Sadler E. M., Ehle M., 1998, MNRAS, 297, 1202 98
- Emonts B., Morganti R., Oosterloo T., van Gorkom J., 2008, arXiv e-prints, p. arXiv:0801.4769 6
- Engelbracht C. W., Rieke M. J., Rieke G. H., Kelly D. M., Achtermann J. M., 1998, ApJ, 505, 639 87
- Ensslin T. A., Biermann P. L., Klein U., Kohle S., 1998, A& A, 332, 395 63
- Event Horizon Telescope Collaboration et al., 2019a, ApJL, 875, L2 9
- Event Horizon Telescope Collaboration et al., 2019b, ApJL, 875, L3 9
- Event Horizon Telescope Collaboration et al., 2019c, ApJL, 875, L4 9

BIBLIOGRAPHY

- Event Horizon Telescope Collaboration et al., 2019d, ApJL, 875, L5 9
- Everett J., 2007, Astrophysics and Space Science, 311, 269 20, 21, 72
- Everett J. E., Murray N., 2007, ApJ, 656, 93 20
- Fabbiano G., Kim D. W., Trinchieri G., 1992, ApJS, 80, 531 85
- Falcke H., Wilson A. S., Simpson C., 1998, ApJ, 502, 199 24, 106, 108
- Falcke H., Körding E., Markoff S., 2004, A& A, 414, 895 14
- Falcón-Barroso J., et al., 2006, MNRAS, 369, 529 85
- Fanaroff B. L., Riley J. M., 1974, MNRAS, 167, 31P 5
- Fermi E., 1949, Phys. Rev., 75, 1169 22
- Feruglio C., Maiolino R., Piconcelli E., Menci N., Aussel H., Lamastra A., Fiore F., 2010, A& A, 518, L155 18
- Fiedler R., Henriksen R. N., 1984, ApJ, 281, 554 127
- Fischer J., et al., 2010, A& A, 518, L41 18
- Flohic H. M. L. G., Eracleous M., Chartas G., Shields J. C., Moran E. C., 2006, ApJ, 647, 140 88
- Foreman G., Volonteri M., Dotti M., 2009, ApJ, 693, 1554 126
- Förster Schreiber N. M., Roussel H., Sauvage M., Charmandaris V., 2004, A& A, 419, 501 88
- Fosbury R. A. E., 1986, Large scale ionized gas in radio galaxies and quasars.. pp 297–306, doi:10.1007/978-90-277-2155-6_17 25, 106
- Foschini L., et al., 2015, A& A, 575, A13 4
- Fukumura K., Tombesi F., Kazanas D., Shrader C., Behar E., Contopoulos I., 2015, ApJ, 805, 17 72

BIBLIOGRAPHY

- Fullmer L., Lonsdale C. J., 1989, JPL D-1932, p. 0 105
- Gabuzda D. C., Cawthorne T. V., Roberts D. H., Wardle J. F. C., 1992, ApJ, 388, 40 27, 98
- Gaensler B. M., Madsen G. J., Chatterjee S., Mao S. A., 2008, , 25, 184 129
- Gallagher S. C., Brandt W. N., Chartas G., Priddey R., Garmire G. P., Sambruna R. M., 2006, The Astrophysical Journal, 644, 709–724 20
- Gallimore J. F., Baum S. A., O'Dea C. P., Pedlar A., 1996, ApJ, 458, 136 41
- Gallimore J. F., Axon D. J., O'Dea C. P., Baum S. A., Pedlar A., 2006, AJ, 132, 546 16, 21, 22, 25, 41, 73, 74, 86, 102, 105, 122, 126, 128, 129
- Gallimore J. F., et al., 2016, ApJL, 829, L7 10
- Gammie C. F., McKinney J. C., Tóth G., 2003, ApJ, 589, 444 14
- Garrington S. T., Leahy J. P., Conway R. G., Laing R. A., 1988, NATURE, 331, 147 128
- Genzel R., Schödel R., Ott T., Eckart A., Alexander T., Lacombe F., Rouan D., Aschenbach B., 2003, NATURE, 425, 934 9
- George I. M., Turner T. J., Netzer H., Nand ra K., Mushotzky R. F., Yaqoob T., 1998, ApJS, 114, 73 86
- Ghez A. M., et al., 2008, ApJ, 689, 1044 9
- Gilli R., Maiolino R., Marconi A., Risaliti G., Dadina M., Weaver K. A., Colbert E. J. M., 2000, A& A, 355, 485 84
- Giommi P., Padovani P., 1994, MNRAS, 268, L51 8
- Giuricin G., Mardirossian F., Mezzetti M., Bertotti G., 1990, ApJS, 72, 551 15
- Golla G., Hummel E., 1994, A& A, 284, 777 89
- González Delgado R. M., Pérez E., Tadhunter C., Vilchez J. M., José Miguel Rodríguez-Espinosa a., 1997, ApJS, 108, 155 86

BIBLIOGRAPHY

- González-Martín O., Masegosa J., Márquez I., Guerrero M. A., Dultzin-Hacyan D., 2006, *A& A*, 460, 45 88
- Goodrich R. W., 1989, *ApJ*, 342, 224 4
- Goodrich R. W., 1992, *ApJ*, 399, 50 24
- Greene J. E., Ho L. C., 2005, *ApJ*, 630, 122 11
- Haardt F., Maraschi L., 1991, *ApJL*, 380, L51 22
- Haardt F., Maraschi L., 1993, *ApJ*, 413, 507 22
- Hamaker J. P., Bregman J. D., Sault R. J., 1996, , 117, 137 xv, 35
- Hamann F., Barlow T., Cohen R. D., Junkkarinen V., Burbidge E. M., 1997, in Arav N., Shlosman I., Weymann R. J., eds, Astronomical Society of the Pacific Conference Series Vol. 128, Mass Ejection from Active Galactic Nuclei. p. 19 ([arXiv:astro-ph/9704234](https://arxiv.org/abs/astro-ph/9704234)) 18
- Hanayama H., Takahashi K., Kotake K., Oguri M., Ichiki K., Ohno H., 2005, *ApJ*, 633, 941 23
- Haniff C. A., Wilson A. S., Ward M. J., 1988, *ApJ*, 334, 104 106
- Harrison C. M., 2017, *Nature Astronomy*, 1, 0165 17
- Harrison C. M., Costa T., Tadhunter C. N., Flütsch A., Kakkad D., Perna M., Vietri G., 2018, *Nature Astronomy*, 2, 198 17
- Hawarden T. G., Israel F. P., Geballe T. R., Wade R., 1995, *MNRAS*, 276, 1197 43
- Heckman T. M., 1980, *A& A*, 500, 187 6
- Heckman T. M., Miley G. K., van Breugel W. J. M., Butcher H. R., 1981, *ApJ*, 247, 403 24, 106
- Heckman T. M., Armus L., Miley G. K., 1990, *ApJS*, 74, 833 105

BIBLIOGRAPHY

- Heckman T. M., Lehnert M. D., Armus L., 1993, Galactic Superwinds. p. 455, doi:10.1007/978-94-011-1882-8_25 17
- Heesen V., Beck R., Krause M., Dettmar R. J., 2011, A& A, 535, A79 27, 65, 102
- Helou G., Khan I. R., Malek L., Boehmer L., 1988, ApJS, 68, 151 114
- Henriksen R., 2019, Galaxies, 7, 53 102
- Hine R. G., Longair M. S., 1979, MNRAS, 188, 111 5
- Hjellming R. M., Johnston K. J., 1981, ApJL, 246, L141 69
- Ho L. C., Peng C. Y., 2001, ApJ, 555, 650 72
- Ho L. C., Ulvestad J. S., 2001, ApJS, 133, 77 15, 97
- Ho L. C., Filippenko A. V., Sargent W. L. W., 1997, ApJ, 487, 568 6, 85
- Hönig S. F., Kishimoto M., Gandhi P., Smette A., Asmus D., Duschl W., Polletta M., Weigelt G., 2010, A& A, 515, A23 10
- Hu J., 2008, MNRAS, 386, 2242 53
- Huchra J., Burg R., 1992, ApJ, 393, 90 74
- Hughes S. A., Blandford R. D., 2003, ApJL, 585, L101 130
- Hummel E., Saikia D. J., 1991, A& A, 249, 43 86
- Hwang H.-C., Zakamska N. L., Alexanderoff R. M., Hamann F., Greene J. E., Perrotta S., Richards G. T., 2018, MNRAS, 477, 830 72
- Imanishi M., Nakanishi K., Izumi T., 2016, ApJL, 822, L10 10
- Irwin J. A., Saikia D. J., 2003, MNRAS, 346, 977 42, 50
- Irwin J. A., Seaquist E. R., 1988, ApJ, 335, 658 42, 50, 67, 68
- Irwin J. A., Saikia D. J., English J., 2000, AJ, 119, 1592 86, 88

BIBLIOGRAPHY

- Irwin J., et al., 2012, AJ, 144, 43 98, 130
- Irwin J. A., et al., 2017, MNRAS, 464, 1333 1, 84, 96, 118, 122, 127, 129, 136
- Irwin J., et al., 2019a, Galaxies, 7, 42 24
- Irwin J., et al., 2019b, AJ, 158, 21 24, 88
- Iwasawa K., Wilson A. S., Fabian A. C., Young A. J., 2003, MNRAS, 345, 369 86
- Iyomoto N., Fukazawa Y., Nakai N., Ishihara Y., 2001, ApJL, 561, L69 42, 53
- Jamrozy M., Machalski J., Mack K. H., Klein U., 2005, A& A, 433, 467 131
- Jarvis M. E., et al., 2019, MNRAS, 485, 2710 17
- Jennison R. C., Das Gupta M. K., 1953, NATURE, 172, 996 12
- Jiménez-Benito L., Díaz A. I., Terlevich R., Terlevich E., 2000, MNRAS, 317, 907 85
- Jurlin N., et al., 2020, A& A, 638, A34 25
- Kaiser C. R., Alexander P., 1997, MNRAS, 286, 215 6
- Kakkad D., et al., 2018, A& A, 618, A6 129
- Kaufman M., Bash F. N., Crane P. C., Jacoby G. H., 1996, AJ, 112, 1021 98
- Kellermann K. I., Sramek R., Schmidt M., Shaffer D. B., Green R., 1989, AJ, 98, 1195 4
- Kennicutt Robert C. J., 1998, ARA&A, 36, 189 113
- Khachikian E. Y., Weedman D. W., 1974, ApJ, 192, 581 3
- Kharb P., O'Dea C. P., Baum S. A., Colbert E. J. M., Xu C., 2006, ApJ, 652, 177 25, 41, 68, 98, 103, 118, 121, 128, 136

BIBLIOGRAPHY

- Kharb P., O'Dea C. P., Baum S. A., Daly R. A., Mory M. P., Donahue M., Guerra E. J., 2008, ApJS, 174, 74 27, 98
- Kharb P., Gabuzda D. C., O'Dea C. P., Shastri P., Baum S. A., 2009, ApJ, 694, 1485 66, 97, 129
- Kharb P., Lister M. L., Cooper N. J., 2010a, ApJ, 710, 764 121
- Kharb P., Hota A., Croston J. H., Hardcastle M. J., O'Dea C. P., Kraft R. P., Axon D. J., Robinson A., 2010b, ApJ, 723, 580 41
- Kharb P., Singh V., Gallimore J. F., Ishwara-Chandra C. H., 2014a, ArXiv e-print 1402.1577, 73
- Kharb P., O'Dea C. P., Baum S. A., Hardcastle M. J., Dicken D., Croston J. H., Mingo B., Noel-Storr J., 2014b, MNRAS, 440, 2976 41, 72
- Kharb P., Srivastava S., Singh V., Gallimore J. F., Ishwara-Chandra C. H., Ananda H., 2016, MNRAS, 459, 1310 73, 86, 129
- Kharb P., Lal D. V., Merritt D., 2017, Nature Astronomy, 1, 727 128
- Kinney A. L., Schmitt H. R., Clarke C. J., Pringle J. E., Ulvestad J. S., Antonucci R. R. J., 2000, ApJ, 537, 152 41
- Klein U., Lisenfeld U., Verley S., 2018, A& A, 611, A55 62
- Knapen J. H., Pérez-Ramírez D., Laine S., 2002, MNRAS, 337, 808 85
- Koay J. Y., Vestergaard M., Bignall H. E., Reynolds C., Peterson B. M., 2016, MNRAS, 460, 304 26
- Komissarov S. S., 1994, MNRAS, 269, 394 5
- Komossa S., Voges W., Xu D., Mathur S., Adorf H.-M., Lemson G., Duschl W. J., Grupe D., 2006, AJ, 132, 531 4
- Kondratko P. K., Greenhill L. J., Moran J. M., 2000, in American Astronomical Society Meeting Abstracts. p. 1586 53

BIBLIOGRAPHY

- Kondratko P. T., Greenhill L. J., Moran J. M., 2005, ApJ, 618, 618 68
- Krause M., et al., 2020, arXiv e-prints, p. arXiv:2004.14383 24, 72, 98, 102
- Krolik J. H., 1998, Active Galactic Nuclei: From the Central Black Hole to the Galactic Environment 21
- Krolik J. H., Begelman M. C., 1988, ApJ, 329, 702 10
- Kukula M. J., Pedlar A., Baum S. A., O'Dea C. P., 1995, MNRAS, 276, 1262 72, 85
- Kukula M. J., Ghosh T., Pedlar A., Schilizzi R. T., 1999, ApJ, 518, 117 16
- Kulsrud R. M., Anderson S. W., 1992, ApJ, 396, 606 23
- Lacy M., Laurent-Muehleisen S. A., Ridgway S. E., Becker R. H., White R. L., 2001, ApJL, 551, L17 71
- Laing R. A., 1980, MNRAS, 193, 439 23, 63
- Laing R. A., Jenkins C. R., Wall J. V., Unger S. W., 1994, in Bicknell G. V., Dopita M. A., Quinn P. J., eds, Astronomical Society of the Pacific Conference Series Vol. 54, The Physics of Active Galaxies. p. 201 5
- Lal D. V., Shastri P., Gabuzda D. C., 2004, A& A, 425, 99 41, 122, 127
- Laor A., Behar E., 2008, MNRAS, 390, 847 22, 72
- Lazar M., Schlickeiser R., Wielebinski R., Poedts S., 2009, ApJ, 693, 1133 23
- Le Roux E., 1961, Annales d'Astrophysique, 24, 71 37
- Leipski C., Falcke H., Bennert N., Hüttemeister S., 2006, A& A, 455, 161 15, 106
- Lerche I., Schlickeiser R., 1980, ApJ, 239, 1089 67
- Lin M.-Y., et al., 2016, MNRAS, 458, 1375 42
- Lira P., Johnson R. A., Lawrence A., Cid Fernand es R., 2007, MNRAS, 382, 1552 87

BIBLIOGRAPHY

- Liu J.-F., Bregman J. N., 2005, ApJS, 157, 59 88
- Liu F. K., Wu X.-B., Cao S. L., 2003, MNRAS, 340, 411 117
- Lynden-Bell D., 1969, NATURE, 223, 690 3
- Lyutikov M., 2006, MNRAS, 373, 73 64
- Magorrian J., et al., 1998, AJ, 115, 2285 126
- Mahatma V. H., et al., 2018, MNRAS, 475, 4557 25
- Mahatma V. H., et al., 2019, A& A, 622, A13 25
- Maiolino R., Stanga R., Salvati M., Rodriguez Espinosa J. M., 1994, A& A, 290, 40 87
- Malkan M. A., Jensen L. D., Rodriguez D. R., Spinoglio L., Rush B., 2017, ApJ, 846, 102 107, 113
- Marinucci A., et al., 2016, MNRAS, 456, L94 10
- Marinucci A., Bianchi S., Braito V., De Marco B., Matt G., Middei R., Nardini E., Reeves J. N., 2020, MNRAS, 84
- Markowitz A. G., Krumpe M., Nikutta R., 2014, MNRAS, 439, 1403 10
- Márquez I., et al., 1999, , 140, 1 128
- Martini P., Regan M. W., Mulchaey J. S., Pogge R. W., 2003, ApJS, 146, 353 84, 118
- McCarthy P. J., van Breugel W., Heckman T., 1987, AJ, 93, 264 87
- McKinney J. C., 2006, MNRAS, 368, 1561 14
- McKinney J. C., Narayan R., 2007, MNRAS, 375, 531 9
- Meier D. L., 1999, ApJ, 522, 753 5
- Meier D. L., 2012, Black Hole Astrophysics: The Engine Paradigm 13

BIBLIOGRAPHY

- Mej  a-Restrepo J. E., Trakhtenbrot B., Lira P., Netzer H., Capellupo D. M., 2016, MNRAS, 460, 187 11
- Merloni A., Heinz S., 2007, MNRAS, 381, 589 109, 113
- Merloni A., Heinz S., di Matteo T., 2003, MNRAS, 345, 1057 14, 114
- Merritt D., Ekers R. D., 2002, Science, 297, 1310 128
- Middleberg E., et al., 2004, A& A, 417, 925 25, 131
- Middleberg E., Krichbaum T. P., Roy A. L., Witzel A., Zensus J. A., 2005a, in Romney J., Reid M., eds, Astronomical Society of the Pacific Conference Series Vol. 340, Future Directions in High Resolution Astronomy. p. 140 42
- Middleberg E., Roy A. L., Bach U., Gabuzda D. C., Beckert T., 2005b, in Romney J., Reid M., eds, Astronomical Society of the Pacific Conference Series Vol. 340, Future Directions in High Resolution Astronomy. p. 189 ([arXiv:astro-ph/0309385](https://arxiv.org/abs/astro-ph/0309385)) 134
- Middleberg E., Agudo I., Roy A. L., Krichbaum T. P., 2007, MNRAS, 377, 731 50
- Miller S. T., Veilleux S., 2003, ApJS, 148, 383 88
- Miyaji T., Wilson A. S., Perez-Fournon I., 1992, ApJ, 385, 137 85
- Miyamoto Y., Nakai N., Seta M., Salak D., Hagiwara K., Nagai M., Ishii S., Yamauchi A., 2015, , 67, 5 43
- Mohan N. R., Anantharamaiah K. R., Goss W. M., 2002, ApJ, 574, 701 87
- Mor R., Netzer H., Elitzur M., 2009, ApJ, 705, 298 9, 10
- Mora-Partiarroyo S. C., et al., 2019a, A& A, 632, A10 89
- Mora-Partiarroyo S. C., et al., 2019b, A& A, 632, A11 89
- Morganti R., Tsvetanov Z. I., Gallimore J., Allen M. G., 1999, , 137, 457 15

BIBLIOGRAPHY

- Morris M. R., Zhao J. H., Goss W. M., 2014, in Sjouwerman L. O., Lang C. C., Ott J., eds, IAU Symposium Vol. 303, The Galactic Center: Feeding and Feedback in a Normal Galactic Nucleus. pp 369–373 ([arXiv:1312.2238](https://arxiv.org/abs/1312.2238)), doi:10.1017/S1743921314000933 66
- Mukherjee D., Bicknell G. V., Sutherland R., Wagner A., 2016, MNRAS, 461, 967 25
- Mukherjee D., Wagner A. Y., Bicknell G. V., Morganti R., Oosterloo T., Nesvadba N., Sutherland R. S., 2018a, MNRAS, 476, 80 25
- Mukherjee D., Bicknell G. V., Wagner A. e. Y., Sutherland R. S., Silk J., 2018b, MNRAS, 479, 5544 25
- Müller-Sánchez F., Prieto M. A., Hicks E. K. S., Vives-Arias H., Davies R. I., Malkan M., Tacconi L. J., Genzel R., 2011, ApJ, 739, 69 42
- Mundell C. G., Wilson A. S., Ulvestad J. S., Roy A. L., 2000, ApJ, 529, 816 16
- Nagar N. M., Wilson A. S., Mulchaey J. S., Gallimore J. F., 1999, ApJS, 120, 209 25
- Nagar N. M., Oliva E., Marconi A., Maiolino R., 2002, A&A, 391, L21 87
- Nakamura M., et al., 2018, ApJ, 868, 146 14
- Nandi S., Jamrozy M., Roy R., Larsson J., Saikia D. J., Baes M., Singh M., 2017, MNRAS, 467, L56 117, 127
- Narayan R., Yi I., 1994, ApJL, 428, L13 10
- Narayan R., Yi I., 1995, ApJ, 452, 710 10
- Nesvadba N. P. H., Drouart G., De Breuck C., Best P., Seymour N., Vernet J., 2017, A&A, 600, A121 113
- Nims J., Quataert E., Faucher-Giguère C.-A., 2015, MNRAS, 447, 3612 72
- O'Dea C. P., 1989, A&A, 210, 35 129

BIBLIOGRAPHY

- O'Dea C. P., Owen F. N., 1987, ApJ, 316, 95–56, 121
- Orienti M., Prieto M. A., 2010, MNRAS, 401, 2599–16
- Osterbrock D. E., 1981, ApJ, 249, 462–3
- Osterbrock D. E., Ferland G. J., 2006, Astrophysics of gaseous nebulae and active galactic nuclei 107
- Osterbrock D. E., Pogge R. W., 1985, ApJ, 297, 166–4
- Pacholczyk A. G., 1977, Oxford Pergamon Press International Series on Natural Philosophy, 89–24
- Padovani P., Giommi P., 1995, MNRAS, 277, 1477–8
- Panessa F., Giroletti M., 2013, MNRAS, 432, 1138–16, 22
- Panessa F., Barcons X., Bassani L., Cappi M., Carrera F. J., Ho L. C., Pellegrini S., 2007, A&A, 467, 519–22, 72
- Panessa F., et al., 2015, MNRAS, 447, 1289–22
- Panessa F., Baldi R. D., Laor A., Padovani P., Behar E., McHardy I., 2019, Nature Astronomy, 3, 387–71
- Pâris I., et al., 2018, A&A, 613, A51–3
- Perez Garcia A. M., Rodriguez Espinosa J. M., Santolaya Rey A. E., 1998, ApJ, 500, 685–85
- Pérez-Torres M. A., Alberdi A., 2007, MNRAS, 379, 275–56
- Perley R. A., Butler B. J., 2013, ApJS, 206, 16–46
- Perley R., Carilli C., Perley D., Dhawan V., 2019, in American Astronomical Society Meeting Abstracts #233. p. 233.01–11
- Perucho M., Martí J. M., Hanasz M., 2005, A&A, 443, 863–6
- Peterson B. M., 1997, An Introduction to Active Galactic Nuclei xv, 7, 11

BIBLIOGRAPHY

- Peterson B. M., et al., 2013, ApJ, 779, 109 11
- Pfrommer C., Jonathan Dursi L., 2010, Nature Physics, 6, 520 64
- Phillips M. M., Malin D. F., 1982, MNRAS, 199, 905 86
- Pogge R. W., 1988, ApJ, 332, 702 86
- Pogge R. W., 1989, ApJ, 345, 730 85, 86
- Pounds K. A., 2014, MNRAS, 437, 3221 18, 72
- Proga D., 2007, in Ho L. C., Wang J. W., eds, Astronomical Society of the Pacific Conference Series Vol. 373, The Central Engine of Active Galactic Nuclei. p. 267 ([arXiv:astro-ph/0701100](https://arxiv.org/abs/astro-ph/0701100)) 19
- Pudritz R. E., Hardcastle M. J., Gabuzda D. C., 2012, , 169, 27 66
- Ramos Almeida C., et al., 2009, ApJ, 702, 1127 10, 84
- Rau U., Cornwell T. J., 2011, A& A, 532, A71 118
- Rawlings S., Saunders R., Eales S. A., Mackay C. D., 1989, MNRAS, 240, 701 108
- Readhead A. C. S., Cohen M. H., Blandford R. D., 1978, NATURE, 272, 131 8
- Rees M. J., 1966, NATURE, 211, 468 12
- Rees M. J., 1971, NATURE, 229, 312 12
- Reynolds C. S., 2014, , 183, 277 14
- Riffel R. A., Storchi-Bergmann T., Winge C., 2013, MNRAS, 430, 2249 42
- Risaliti G., Elvis M., Nicastro F., 2002, ApJ, 571, 234 86
- Romero G. E., Müller A. L., Roth M., 2018, A& A, 616, A57 63
- Rossa J., Dettmar R. J., 2003, A& A, 406, 505 85

BIBLIOGRAPHY

- Roy A. L., Norris R. P., Kesteven M. J., Troup E. R., Reynolds J. E., 1994, ApJ, 432, 496 41
- Rupke D., 2018, Galaxies, 6, 138 17
- Rupke D. S. N., Veilleux S., 2011, ApJL, 729, L27 18
- Rush B., Malkan M. A., Spinoglio L., 1993, ApJS, 89, 1 74
- Saikia D. J., Konar C., Kulkarni V. K., 2006, MNRAS, 366, 1391 117
- Saikia P., Körding E., Coppejans D. L., Falcke H., Williams D., Baldi R. D., McHardy I., Beswick R., 2018, A& A, 616, A152 114
- Sales D. A., et al., 2015, ApJ, 799, 25 122
- Salvato M., Greiner J., Kuhlbrodt B., 2004, ApJL, 600, L31 22
- Sams Bruce J. I., Genzel R., Eckart A., Tacconi-Garman L., Hofmann R., 1994, ApJL, 430, L33 87
- Sanders R. H., 1984, A& A, 140, 52 25, 130
- Saripalli L., 2012, AJ, 144, 85 6
- Sawada-Satoh S., Inoue M., Shibata K. M., Kameno S., Migenes V., Nakai N., Diamond P. J., 2000, , 52, 421 50, 68
- Scargle J. D., Caroff L. J., Noerdlinger P. D., 1970, ApJL, 161, L115 19
- Schawinski K., Koss M., Berney S., Sartori L. F., 2015, MNRAS, 451, 2517 26
- Schmidt M., Green R. F., 1983, ApJ, 269, 352 4
- Schmitt H. R., Kinney A. L., 2002, New Astronomy Review, 46, 231 41
- Schmitt H. R., Kinney A. L., Storchi-Bergmann T., Antonucci Robert 1997, ApJ, 477, 623 25
- Schmitt H. R., Antonucci R. R. J., Ulvestad J. S., Kinney A. L., Clarke C. J., Pringle J. E., 2001, ApJ, 555, 663 25, 41, 73, 86

BIBLIOGRAPHY

- Schmitt H. R., Donley J. L., Antonucci R. R. J., Hutchings J. B., Kinney A. L., 2003, ApJS, 148, 327 86
- Schoenmakers A. P., de Bruyn A. G., Röttgering H. J. A., van der Laan H., Kaiser C. R., 2000, MNRAS, 315, 371 13, 117
- Schwarz U. J., 1978, A& A, 65, 345 31
- Sebastian B., Ishwara-Chandra C. H., Joshi R., Wadadekar Y., 2018, MNRAS, 473, 4926 117
- Sebastian B., Kharb P., O'Dea C. P., Gallimore J. F., Baum S. A., 2019a, MNRAS, 490, L26 73, 84, 96
- Sebastian B., Kharb P., O'Dea C. P., Colbert E. J. M., Baum S. A., 2019b, ApJ, 883, 189 73, 77, 84, 96, 97, 102, 103, 118
- Shafi N., Oosterloo T. A., Morganti R., Colafrancesco S., Booth R., 2015, MNRAS, 454, 1404 43, 68
- Shakura N. I., Sunyaev R. A., 1973, A& A, 500, 33 5, 9
- Shapiro S. L., Lightman A. P., Eardley D. M., 1976, ApJ, 204, 187 10, 50
- Shlosman I., Vitello P. A., Shaviv G., 1985, ApJ, 294, 96 19
- Shlosman I., Begelman M. C., Frank J., 1990, NATURE, 345, 679 9
- Sikora M., Begelman M. C., 2013, ApJL, 764, L24 15
- Sikora M., Stawarz Ł., Lasota J.-P., 2007, ApJ, 658, 815 14, 130
- Silva L., Granato G. L., Bressan A., Danese L., 1998, ApJ, 509, 103 122
- Singh V., Chand H., 2018, MNRAS, 480, 1796 17
- Singh V., Ishwara-Chandra C. H., Wadadekar Y., Beelen A., Kharb P., 2015, MNRAS, 446, 599 17
- Sofue Y., Koda J., Kohno K., Okumura S. K., Honma M., Kawamura A., Irwin J. A., 2001, ApJL, 547, L115 43

BIBLIOGRAPHY

- Sokoloff D. D., Bykov A. A., Shukurov A., Berkhuijsen E. M., Beck R., Poezd A. D., 1998, MNRAS, 299, 189 38
- Stalin C. S., Gopal-Krishna Sagar R., Wiita P. J., Mohan V., Pandey A. K., 2006, MNRAS, 366, 1337 6
- Stone John L. J., Wilson A. S., Ward M. J., 1988, ApJ, 330, 105 86
- Strickland D. K., Heckman T. M., Colbert E. J. M., Hoopes C. G., Weaver K. A., 2004, ApJS, 151, 193 89
- Suchkov A. A., Balsara D. S., Heckman T. M., Leitherer C., 1994, ApJ, 430, 511 102
- Suchkov A. A., Berman V. G., Heckman T. M., Balsara D. S., 1996, ApJ, 463, 528 102
- Thean A., Pedlar A., Kukula M. J., Baum S. A., O'Dea C. P., 2000, MNRAS, 314, 573 41, 72, 86, 120
- Thean A. H. C., Gillibrand T. I., Pedlar A., Kukula M. J., 2001, MNRAS, 327, 369 16, 72
- Thomas A. D., et al., 2017, ApJS, 232, 11 87
- Thompson A. R., Moran J. M., Swenson George W. J., 2017, Interferometry and Synthesis in Radio Astronomy, 3rd Edition, doi:10.1007/978-3-319-44431-4. 29
- Tombesi F., Cappi M., Reeves J. N., Palumbo G. G. C., Yaqoob T., Braito V., Dadina M., 2010, A& A, 521, A57 18, 72
- Trotter A. S., Greenhill L. J., Moran J. M., Reid M. J., Irwin J. A., Lo K.-Y., 1998, ApJ, 495, 740 50, 68
- Ulvestad J. S., 2003, in Zensus J. A., Cohen M. H., Ros E., eds, Astronomical Society of the Pacific Conference Series Vol. 300, Radio Astronomy at the Fringe. p. 97 ([arXiv:astro-ph/0301057](https://arxiv.org/abs/astro-ph/0301057)) 131
- Ulvestad J. S., Wilson A. S., 1984a, ApJ, 278, 544 15, 41, 86

BIBLIOGRAPHY

- Ulvestad J. S., Wilson A. S., 1984b, ApJ, 285, 439 15, 41
- Ulvestad J. S., Wilson A. S., 1989, ApJ, 343, 659 16
- Ulvestad J. S., Wilson A. S., Sramek R. A., 1981, ApJ, 247, 419 15, 68, 72
- Ulvestad J. S., Roy A. L., Colbert E. J. M., Wilson A. S., 1998, ApJ, 496, 196 41
- Ulvestad J. S., Wrobel J. M., Carilli C. L., 1999, ApJ, 516, 127 97
- Unger S. W., Lawrence A., Wilson A. S., Elvis M., Wright A. E., 1987, MNRAS, 228, 521 16
- Urry C. M., Padovani P., 1995, , 107, 803 xv, 3, 8, 9, 10, 12
- Vaidya B., Fendt C., Beuther H., Porth O., 2011, ApJ, 742, 56 19
- Veilleux S., 1991a, ApJS, 75, 383 25, 106
- Veilleux S., 1991b, ApJ, 369, 331 25, 106
- Veilleux S., Osterbrock D. E., 1987, ApJS, 63, 295 xv, 7, 62
- Veilleux S., Cecil G., Bland-Hawthorn J., Tully R. B., Filippenko A. V., Sargent W. L. W., 1994, ApJ, 433, 48 42
- Veilleux S., Shopbell P. L., Miller S. T., 2001, AJ, 121, 198 84
- Veilleux S., Cecil G., Bland-Hawthorn J., 2005, ARA&A, 43, 769 17, 113
- Véron-Cetty M. P., Véron P., 2006, A& A, 455, 773 84
- Wals M., Boyle B. J., Croom S. M., Miller L., Smith R., Shanks T., Outram P., 2005, MNRAS, 360, 453 71
- Weaver K. A., Heckman T. M., Strickland D. K., Dahlem M., 2002, ApJL, 576, L19 87
- Weedman D. W., 1978, MNRAS, 184, 11P 85
- Wehrle A. E., Morris M., 1988, AJ, 95, 1689 68, 84

BIBLIOGRAPHY

- White R. L., Helfand D. J., Becker R. H., Glikman E., de Vries W., 2007, ApJ, 654, 99–71
- Whittle M., 1985, MNRAS, 213, 33–24, 106
- Whittle M., Pedlar A., Meurs E. J. A., Unger S. W., Axon D. J., Ward M. J., 1988, ApJ, 326, 125–24
- Wilson A. S., Colbert E. J. M., 1995, ApJ, 438, 62–130
- Wilson A. S., Tsvetanov Z. I., 1994, AJ, 107, 1227–24
- Wilson A. S., Ulvestad J. S., 1982, ApJ, 263, 576–68
- Wilson A. S., Ulvestad J. S., 1983, ApJ, 275, 8–68, 98
- Wilson A. S., Penston M. V., Fosbury R. A. E., Boksenberg A., 1976, MNRAS, 177, 673–87
- Woodfinden A., Henriksen R. N., Irwin J., Mora-Partiarroyo S. C., 2019, MNRAS, 487, 1498–26
- Wrobel J. M., Heeschen D. S., 1988, ApJ, 335, 677–13, 85
- Wrobel J. M., Heeschen D. S., 1991, AJ, 101, 148–13
- Xu C., Livio M., Baum S., 1999, AJ, 118, 1169–24, 106
- Yamagishi M., Kaneda H., Ishihara D., Komugi S., Suzuki T., Onaka T., 2010, Publications of the Astronomical Society of Japan, 62, 1085–67
- Yang Z., Bian W.-H., Wang Y., 2013, Ap& SS, 348, 517–85
- Yun M. S., Reddy N. A., Condon J. J., 2001, ApJ, 554, 803–xix, 103, 104, 105
- Zakamska N. L., Greene J. E., 2014, MNRAS, 442, 784–72, 106
- Zhang D., 2018, Galaxies, 6, 114–17
- Zhang X., Zhang H., Zhang X., 2018, Ap& SS, 363, 259–114

BIBLIOGRAPHY

- Zirbel E. L., Baum S. A., 1995, ApJ, 448, 521–5
- de Bruyn A. G., Wilson A. S., 1976, A&A, 53, 93–16, 41
- de Bruyn A. G., Wilson A. S., 1978, A&A, 64, 433–15, 16, 24, 106
- van Weeren R. J., et al., 2016, ApJ, 818, 204–63
- van der Laan H., Perola G. C., 1969, A&A, 3, 468–121